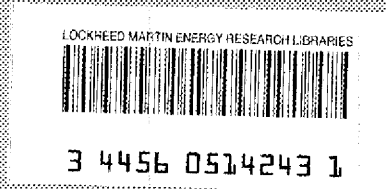# OAK RIDGE NATIONAL LABORATORY
operated by
UNION CARBIDE CORPORATION • NUCLEAR DIVISION
for the
U. S. ATOMIC ENERGY COMMISSION
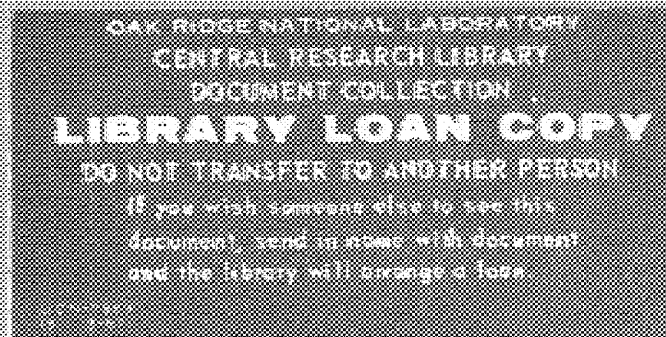
ORNL - TM - 3139

ENGINEERING DEVELOPMENT STUDIES FOR MOLTEN-SALT BREEDER REACTOR PROCESSING NO. 4

L. E. McNeese

ENGINEERING DEVELOPMENT STUDIES FOR MOLTEN-SALT BREEDER REACTOR PROCESSING NO. 4

L. E. McNeese

AUGUST 1971

Reports previously issued in this series are as follows:

ORNL-4234	Period ending September 1967
ORNL-4235	Period ending December 1967
ORNL-4364	Period ending March 1968
ORNL-4365	Period ending June 1968
ORNL-4366	Period ending September 1968
ORNL-TM-3053	Period ending December 1968
ORNL-TM-3137	Period ending March 1969
ORNL-TM-3138	Period ending June 1969

CONTENTS

CONTENTS (Continued)

SUMMARIES

SEMICONTINUOUS REDUCTIVE EXTRACTION EXPERIMENTS
IN A MILD-STEEL FACILITY

The first hydrodynamic run (HR-4) attempted after the salt over-flow line had been modified was cut short by the failure of tubing at the base of the packed column and the resultant leakage of salt and bismuth from the column. This line, as well as a transfer line on which a resistance heater had failed, was replaced, and the bismuth and the salt were treated with a H_2-HF mixture before the hydrodynamic experiments were resumed.

The subsequent experiment (HR-5) yielded useful pressure-drop data, verified the effectiveness of changes in the overflow piping, and showed that automating the level control for the salt jackleg provided more nearly constant salt flow rates to the column.

MEASUREMENT OF AXIAL DISPERSION COEFFICIENTS
IN PACKED COLUMNS

We have initiated an experimental program for measuring axial dispersion coefficients in packed columns under conditions similar to those that will apply in proposed reductive extraction processes; in this program, mercury and water simulate the bismuth and molten salt. We are using a steady-state technique in which the concentration profile of a tracer is determined photometrically at various points along the column. Results from seven experiments with 3/8-in.-diam Raschig ring packing indicate that the dispersion coefficient is about 3.5 cm^2/sec and has little dependence on either the dispersed-phase flow rate or the continuous-phase flow rate.

A SIMPLIFIED METHOD FOR ESTIMATING THE EFFECT OF AXIAL DISPERSION
ON COUNTERCURRENT COLUMN PERFORMANCE

A simple, rapid method has been developed for estimating the effect of axial dispersion on the performance of countercurrent contactors. The column efficiency (i.e., the ratio of the height of a contactor in which no axial dispersion occurs to the height of a contactor in which axial dispersion is present) is given as a simple function of design parameters (extraction factor, number of transfer units, height of a plug flow transfer unit, and the axial dispersion coefficient). The contactor efficiency can be estimated with axial dispersion present in one phase, or in both phases, for most operating conditions of interest. The predicted values for contactor efficiency are in satisfactory agreement with values calculated from published solutions to the continuity equation for countercurrent flow with axial dispersion and mass transfer between phases.

EFFECT OF AXIAL DISPERSION IN PACKED COLUMN CONTACTORS
USED FOR MSBR PROCESSING

We have completed calculations that show the effect of axial dispersion in packed column contactors specified by MSBR processing flowsheets. These calculations indicate that the efficiency of the columns used for isolating protactinium is high and that axial dispersion will require the length of such columns to be increased by less than 10% over that for columns in which no axial dispersion is present. The calculated efficiencies for the rare-earth columns are quite low; thus we conclude that axial dispersion preventers or staging would be required for these columns.

AXIAL DISPERSION IN AN OPEN BUBBLE COLUMN

Axial dispersion in an air-water system was studied as a function
of gas and liquid flow rates in a 2-in.-ID open bubble column. The
degree of mixing was characterized by a dispersion coefficient defined
in a manner analogous to Fick's law. The experimental technique in-
volved continuously injecting $Cu(NO_3)_2$ tracer and measuring the tracer
concentration gradient along the length of the column at steady state
by a photometric technique. Within the range of operating conditions
studied, the dispersion coefficient was found to be independent of
liquid flow rate. The dispersion coefficient increased from 26.9
cm^2/sec to 35 cm^2/sec as the volumetric gas flow rate was increased
from 5.2 cm^3/sec to 44 cm^3/sec. At gas flow rates higher than 44
cm^3/sec, it was more dependent on gas flow rate and increased to a
value of 68.7 cm^2/sec at a gas flow rate of 107 cm^3/sec. The experi-
mentally determined values for the dispersion coefficient are higher
than the values reported in the literature.

ELECTROLYTIC CELL DEVELOPMENT: STATIC CELL EXPERIMENTS

Experiments directed toward two problems related to cell develop-
ment were carried out in static cells. Results showed that a protec-
tive layer of frozen salt could be maintained on a surface in the pres-
ence of high heat generation rates in adjacent salt. An experiment in
which lead-acid batteries were used to provide dc power showed that the
ac ripple in the nominal dc power in previous experiments was not re-
sponsible for the formation of dark-colored material in the salt.

DESIGN AND INSTALLATION OF THE FLOW ELECTROLYTIC
CELL FACILITY

A facility for continuously circulating molten salt and bismuth
through electrolytic cells at temperatures up to 600°C is being in-
stalled. The equipment associated with this facility will allow us to

test a variety of cell designs under conditions similar to those ex-
pected in processing plants. The equipment consists of a 16-in.-diam
vessel that will contain the cell to be tested, a mixer-settler tank
in which the salt and bismuth streams from the cells will be equili-
brated, gas-lift pumps and orifice--head pot flowmeters for circulating
and metering the streams to the cell, and a vessel containing a graph-
ite crucible for purifying the salt and bismuth.

CALIBRATION OF AN ORIFICE-HEAD POT FLOWMETER WITH MOLTEN SALT AND BISMUTH

The Flow Electrolytic Cell Facility contains orifice--head pot flow-
meters for measuring salt and bismuth flow rates. Calibration of this
equipment is being carried out prior to operation of the facility to
ensure that uncertainties in flow rates will be acceptably small. Ini-
tial tests with mercury and water in a Lucite head pot showed the need
for an enlarged drainage chamber downstream of the orifice. Subsequent
experiments with transient flows resulted in average orifice coeffi-
cients of 0.663 and 0.709 for mercury and water, respectively. Experi-
ments with transient flows of bismuth and molten salt through a mild-
steel head pot at 600°C resulted in average orifice coefficients of
0.646 and 0.402, respectively. Experiments with steady bismuth flows
resulted in an average orifice coefficient of 0.654.

BISMUTH-SALT INTERFACE DETECTOR

A salt-metal interface detection device is needed for use with
salt-metal extraction columns. A modified version of an induction type
of liquid-level probe is under study. The inductance coil consists of
a bifilar winding of 30-gage platinum wire wound in grooves on the sur-
face of a lavite form. For testing, the detector coil will be mounted

on a type 316 stainless steel tube having an outside diameter of 0.050 in. and a wall thickness of 0.065 in. Portions of the tube that are in contact with bismuth will be coated with a 0.005-in. layer of tungsten to prevent attack of the stainless steel by the bismuth.

STRIPPING OF ThF_4 FROM MOLTEN SALT BY REDUCTIVE EXTRACTION

Efficient operation of the reductive extraction system for rare-earth removal requires that only a negligible quantity of ThF_4 remain in the salt which passes through the electrolytic cell and returns to the bottom of the extraction column. Calculated results show that ThF_4 can be removed from the salt to the extent required by reductive extraction, using two to three theoretical stages.

1. INTRODUCTION

A molten-salt breeder reactor (MSBR) will be fueled with a molten fluoride mixture that will circulate through the blanket and core regions of the reactor and through the primary heat exchangers. We are developing processing methods for use in a close-coupled facility for removing fission products, corrosion products, and fissile materials from the molten fluoride mixture.

Several operations associated with MSBR processing are under study. The remaining parts of this report describe: (1) experiments on the hydrodynamics of packed column operation, carried out in a mild-steel reductive extraction facility, (2) measurement of axial dispersion in packed columns in which immiscible fluids having large density differences are flowing countercurrently, (3) a simplified method for estimating the effect of axial dispersion on countercurrent column performance, (4) estimates of the effect of axial dispersion in packed column contactors used for MSBR processing, (5) measurements of axial dispersion coefficients in an open bubble column, (6) experiments related to the development of electrolytic cells for use with molten salt and bismuth, (7) the design and installation of the Flow Electrolytic Cell Facility, (8) the calibration of an orifice--head pot flowmeter for use with the Flow Electrolytic Cell Facility, (9) the development of an induction type of bismuth-salt interface detector, and (10) calculations regarding the removal of ThF_4 from molten-salt streams by reductive extraction. This work was carried out in the Chemical Technology Division during the period July through September 1969.

2. SEMICONTINUOUS REDUCTIVE EXTRACTION EXPERIMENTS IN A MILD-STEEL FACILITY

B. A. Hannaford   C. W. Kee
L. E. McNeese

The first hydrodynamic run (HR-4) attempted after the salt overflow line had been modified[1] was cut short by the failure of tubing at

the base of the packed column and the resultant leakage of salt and bismuth from the column. This line, as well as a transfer line on which a resistance heater had failed, was replaced and the bismuth and salt were treated with a H_2-HF mixture before the hydrodynamic experiments were resumed.

The subsequent experiment (HR-5) yielded useful pressure-drop data, verified the effectiveness of changes in the overflow piping, and showed that automating the level control for the salt jackleg provided more nearly constant salt flow rates to the column.

2.1 Hydrodynamic Run HR-4

The objectives of the fourth hydrodynamic experiment (Run HR-4) were: (1) to test the effectiveness of revisions in the salt overflow line, and (2) to investigate a new method for controlling the liquid level in the salt jackleg. However, this run had to be terminated after only 5 min of operation because salt and bismuth were found to be leaking from the bismuth overflow line near the base of the column. No useful hydrodynamic data were obtained.

Examination of the 3/8-in.-diam mild steel tubing disclosed the presence of two holes — one about 1/8 in. in diam and the other essentially a crack. The second crack-like hole was located about 2 in. above the first hole at the juncture of the tubing with a weld fillet, which attached the tube to the base of the column. Metallographic examination of transverse and longitudinal sections of the tubing indicated that the failures were probably due to oxidation by external air. The absence of cracks or grain distortion in areas near the failures indicated that stress was probably not a factor. Although the inside surface of the line was slightly roughened, there was no other indication of attack by the molten salt and bismuth. The outer surface was much more irregular, especially in the areas near the failures. Measurements showed that the

wall thickness of the section that had been in service for the longest period of time (>500 hr) had been reduced from 0.058 in. to as little as 0.010 in. in some locations.

A second failure occurred in the 3/8-in. steel transfer line connecting the bismuth receiver and the treatment vessel; however, it did not result in the loss of salt or bismuth. Shortly after this line was heated to about 700°C in order to melt a suspected salt plug, the resistance heater grounded to the tubing and burned a hole in the tubing. Examination of the tubing revealed no clues as to the cause of the formation of the salt plug; the internal surfaces were free of metal or salt deposits, and both the internal and the external surfaces had suffered little corrosion.

2.2 Treatment of Bismuth and Salt with H_2-HF

After the two transfer lines had been replaced, the salt and bismuth were transferred to the treatment vessel for purification. The procedure was substantially the same as that described previously[1]; that is, the two phases were sparged with a 75-25 mole % H_2-HF mixture at the rate of 16 scfh for 23 hr in order to remove oxides. The HF utilization ranged from 10% initially to about 1 to 2% at the time treatment was terminated. The flow of the H_2-HF mixture was interrupted twice when a small amount of material (salt-like in appearance) collected in the off-gas line.

2.3 Hydrodynamic Run HR-5

The system modifications that were made prior to Run HR-4 to improve the control of the salt and bismuth flow rates were shown to be effective during Run HR-5. The automatic level control for the salt jackleg held the liquid level constant to within ± 0.05 in. The bismuth drain line on the salt overflow loop prevented accumulation of bismuth at this point, which had been a source of difficulty previously. The salt and bismuth

flow rates remained within about ± 2% of the desired values during several selected time intervals. The freeze valve below the bismuth entrainment detector was operated in the open position, and no measurements were made of bismuth accumulation resulting from entrainment.

Run HR-5 began with a 28-min period of bismuth flow only, during which the flow rate was stable at 80 ml/min (nominal). Salt flow was then started, and about 20 min of operation was required for the salt flow rate to become steady. However, approximately 15 min of this time period was required to fill the salt jackleg.

During Run HR-5, stable flows of salt and bismuth were obtained at six sets of flow rates, as shown in Table 1. Of these flow rates, five represented nonflooded conditions. Rates that were interpreted as flooding rates are those occurring during periods of high (and increasing) apparent bismuth holdup in the column. Such a period is usually followed by a period of unstable flow of both phases. Table 1 also shows the apparent bismuth holdup in the column during the periods of steady flow. (There is no provision for measuring holdup directly.) The apparent holdup is defined as the holdup that is necessary to produce the observed pressure drop. This value will normally be less than the actual holdup since part of the weight of the bismuth is supported by the packing and does not contribute to the pressure drop of the continuous phase.

Apparent holdup seems to be strongly dependent upon V_d, the dispersed-phase superficial velocity, but is almost independent of V_c, the continuous-phase superficial velocity. This is shown most strikingly by a comparison of time intervals 4 and 5, during which the apparent holdup failed to change even though V_c was doubled.

Table 1. Apparent Bismuth Holdup and Flow Rate Data for Hydrodynamic Experiment HR-5

Interval Number	Steady Flow Duration (min)	Flow Rate (ml/min)		Superficial Velocity[a] (ft/hr)		Apparent Bismuth Holdup (vol %)	Comments
		Bismuth	Salt	Bismuth, V_d	Salt, V_c		
1	12.0	70.7	71.0	40.4	40.6	≤ 16	
2	8.0	76.8	71.0	43.8	40.6	∿21	
3	21.5	85.4	70.2	48.8	40.1	∿28	
4	8.5	87.0	70.2	49.7	40.1	∿28	
5	6.0	87.0	156.7	49.7	89.5	∿28	
6	13.0	93.9	134.7	53.6	76.9	51→72	Flooding

[a] Based on cross-sectional area of 0.00371 ft^2 for 0.824-in.-ID column.

3. MEASUREMENT OF AXIAL DISPERSION COEFFICIENTS IN PACKED COLUMNS

J. S. Watson   L. E. McNeese

Axial dispersion in the continuous (salt) phase can reduce the performance of the packed column contactors that are proposed for the MSBR fuel processing system. Effects of axial dispersion will be most severe in the rare-earth removal columns, where high flow ratios are required. We have initiated an experimental program in which axial dispersion coefficients in packed columns are measured under conditions similar to those in the proposed reductive extraction processes; in this program, mercury and water simulate bismuth and molten salt. The measured axial dispersion coefficients will be used to estimate column performance in the proposed systems. If the required heights for ordinary packed columns are found to be excessive, devices for reducing axial dispersion will be developed.

3.1 Mathematical Model

A steady-state technique was used in making the axial dispersion coefficient measurements; its theoretical development was as follows. Consider a column of constant cross section in which a fluid moves with constant superficial velocity, v. If a tracer material is introduced near the column exit, the tracer will tend to diffuse upstream and a concentration profile will be established. At steady state, the flux of the tracer due to axial dispersion is equal to the convective flux; that is,

$$-E \frac{dC}{dZ} = vC, \tag{1}$$

where
    E = axial dispersion coefficient,
    C = tracer concentration at position Z,
    v = superficial fluid velocity,
    Z = position along the column.

Integration of this relation, assuming that the concentration at point Z_1 is C_1, yields the relation

$$\ln \frac{C}{C_1} = - \frac{v}{E} (Z - Z_1), \qquad (2)$$

which indicates that a semilogarithmic plot of C/C_1 vs Z should yield a straight line of slope $-v/E$.

3.2 Experimental Technique and Equipment

The experimental technique for measuring the concentration profile is illustrated in Figs. 1 and 2. Figure 1 is a schematic diagram of the column and sampling system; Fig. 2 is a photograph of the column with the associated samplers. A small stream of water (flow rate, approximately 1 ml/min) is withdrawn from the column, circulated through a cell containing a light source and a photocell, and then returned to the column at the same elevation. The circulating stream is driven by a small centrifugal pump that uses a magnetically coupled impeller (Fig. 3). The photocells are cylindrical in shape and have a 1/2-in. inside diameter. The light path, 1/2 in. in length, lies along the axis of the cell. The light source is a G.E. No. 253X lamp, and the detectors are Clairex CL707L photoresistors. Two photocells are shown in Fig. 4.

The tracer material, which consists of an aqueous solution of $Cu(NO_3)_2$, is injected near the top of the column with a syringe pump. Several sampling points are located at various positions down the column. The tracer concentration in each photocell is observed until steady state is reached; with a 4-ft column, this normally takes 2 to 4 hr. The solutions to be analyzed are very dilute, and the response of the photoresistors is essentially linear (a limiting form of Beer's law) as confirmed by experiment. Readings from each detector are taken both with no tracer present (i.e., with the column containing water) and with a single calibration solution. The calibration solution is gen-

ORNL DWG 69-10321
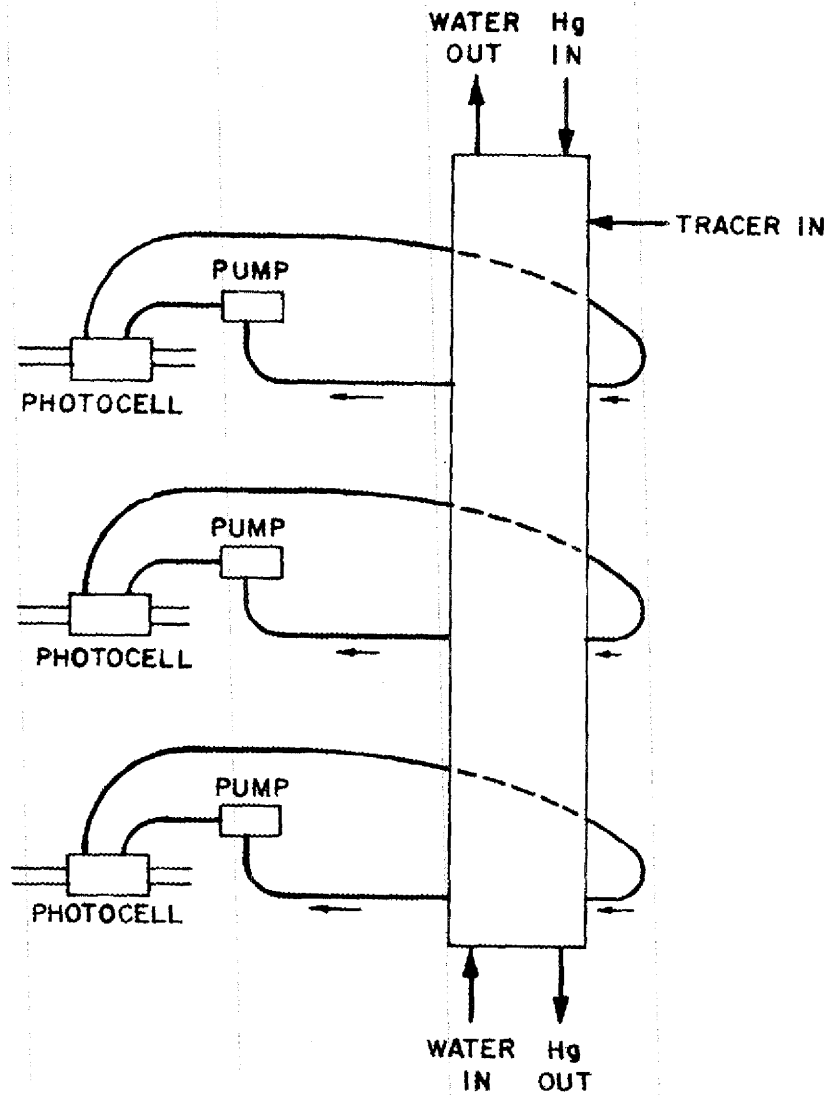
Fig. 1. Schematic of Equipment for Studying Axial Dispersion in a Packed Column During Countercurrent Flow of Mercury and Water.

Fig. 2. Equipment Used for Study of Axial Dispersion in a Packed Column During Countercurrent Flow of Mercury and Water.

PHOTO 97027

Fig. 3. Magnetically Driven Centrifugal Pump Used for Circulating Solution from Column Through Photocell.
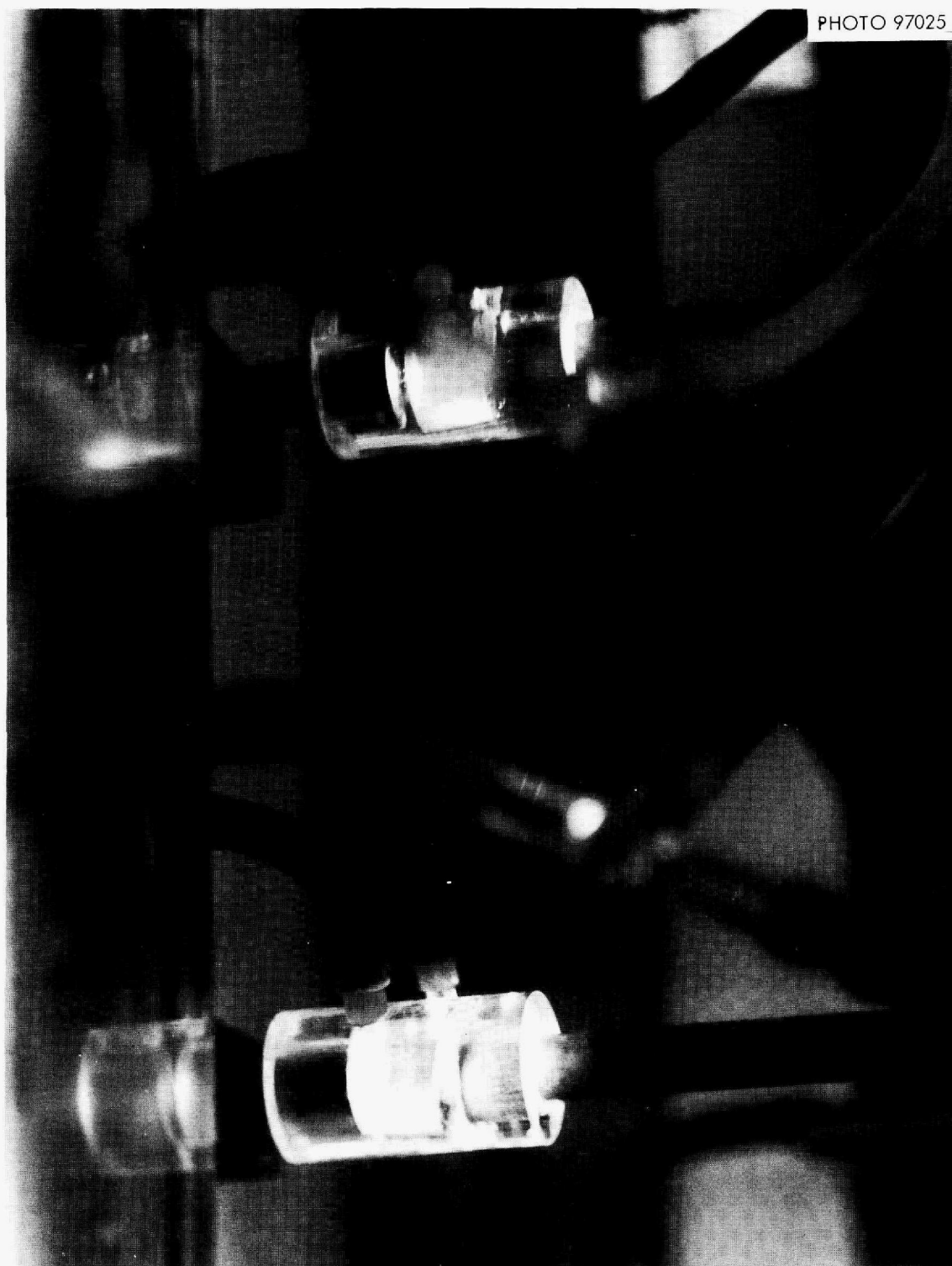
Fig. 4. Photocells Used for Determining the Concentration of Tracer in the Solution Withdrawn from the Column.

erated by injecting a small amount of tracer into the column when no water is flowing; after the tracer has been mixed throughout the column, each detector can be calibrated at the same tracer concentration. Such a calibration is made at the beginning of each run. This procedure requires that only relative concentrations, rather than absolute concentrations, be measured.

3.3 Experimental Results

The results of seven runs with 3/8-in.-diam Raschig rings are shown in Figs. 5 through 11; they are summarized in Table 2 and Fig. 12. Various mercury and water flow rates were used to determine whether the dispersion coefficient is a function of either the dispersed-phase or the continuous-phase flow rate. Figure 12 shows the measured values as a function of the mercury flow rate (the dispersed-phase flow rate was considered more likely to affect axial dispersion). Although considerable scatter exists in the data, there is no evidence that the dispersion coefficient is affected by either of the flow rates. The scatter of the data is most severe at high mercury flow rates, where mercury tends to enter the sample ports, and at both high and low water flow rates, where the concentration profile is either too steep or too shallow for accurate determination of the slope. All of these data were taken at less than 50% of the flooding rate. Although subsequent experiments may show that the axial dispersion coefficient is essentially constant over a wider range of flow rates, one should not presently extrapolate these findings to flooding conditions. It is known that holdup and drop size change significantly just before flooding occurs; it is possible that the axial dispersion coefficient may also change.

Fig. 5.   Steady-State Continuous-Phase Tracer Concentration During Countercurrent Flow of Mercury and Water in a 2-in.-diam Column Packed with 3/8-in. Raschig Rings.

Fig. 6. Steady-State Continuous-Phase Tracer Concentration During Countercurrent Flow of Mercury and Water in a 2-in.-diam Column Packed with 3/8-in. Raschig Rings.

Fig. 7. Steady-State Continuous-Phase Tracer Concentration During Countercurrent Flow of Mercury and Water in a 2-in.-diam Column Packed with 3/8-in. Raschig Rings.

Fig. 8. Steady-State Continuous-Phase Tracer Concentration During Countercurrent Flow of Mercury and Water in a 2-in.-diam Column Packed with 3/8-in. Raschig Rings.

WATER SUPERFICIAL VELOCITY 2.28 ft/hr
MERCURY SUPERFICIAL VELOCITY 121.4 ft/hr
CALCULATED DISPERSION COEFFICIENT 4.33 cm²/sec
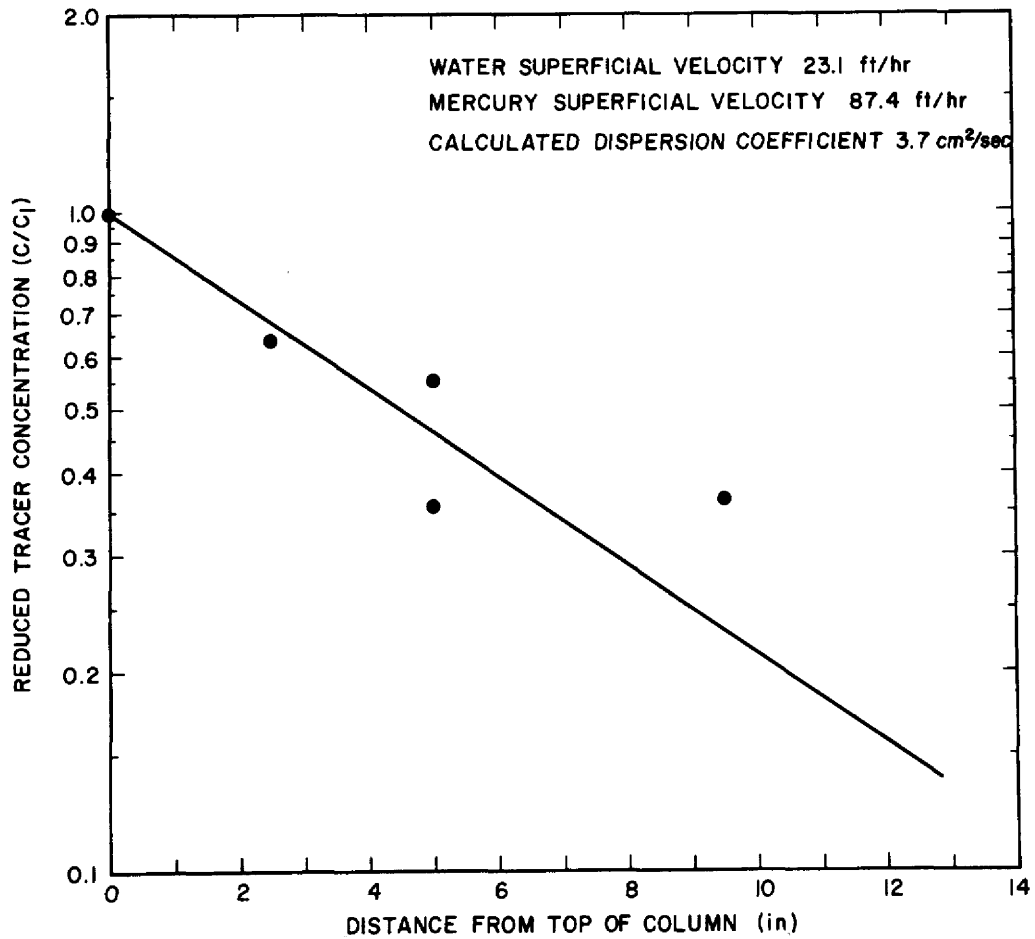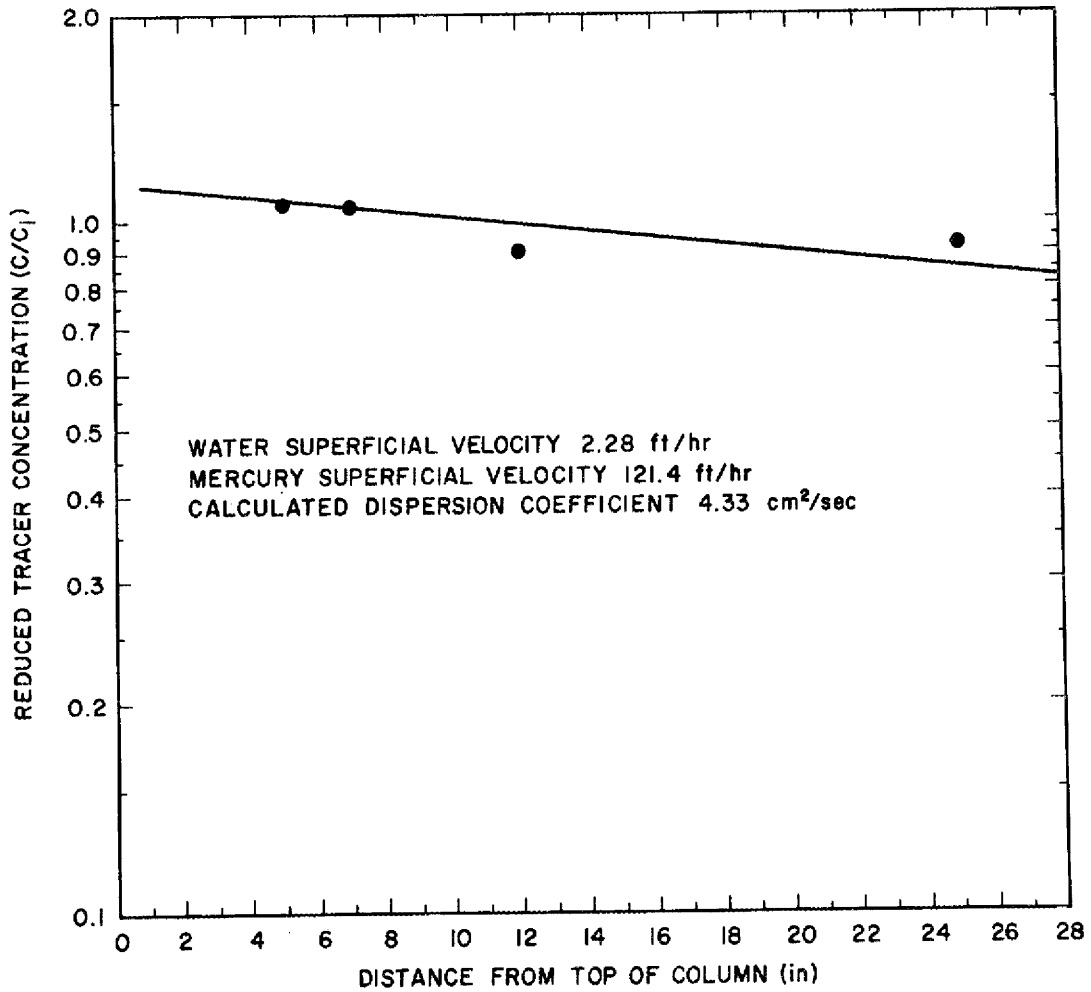
Fig. 9. Steady-State Continuous-Phase Tracer Concentration During Countercurrent Flow of Mercury and Water in a 2-in.-diam Column Packed with Raschig Rings.
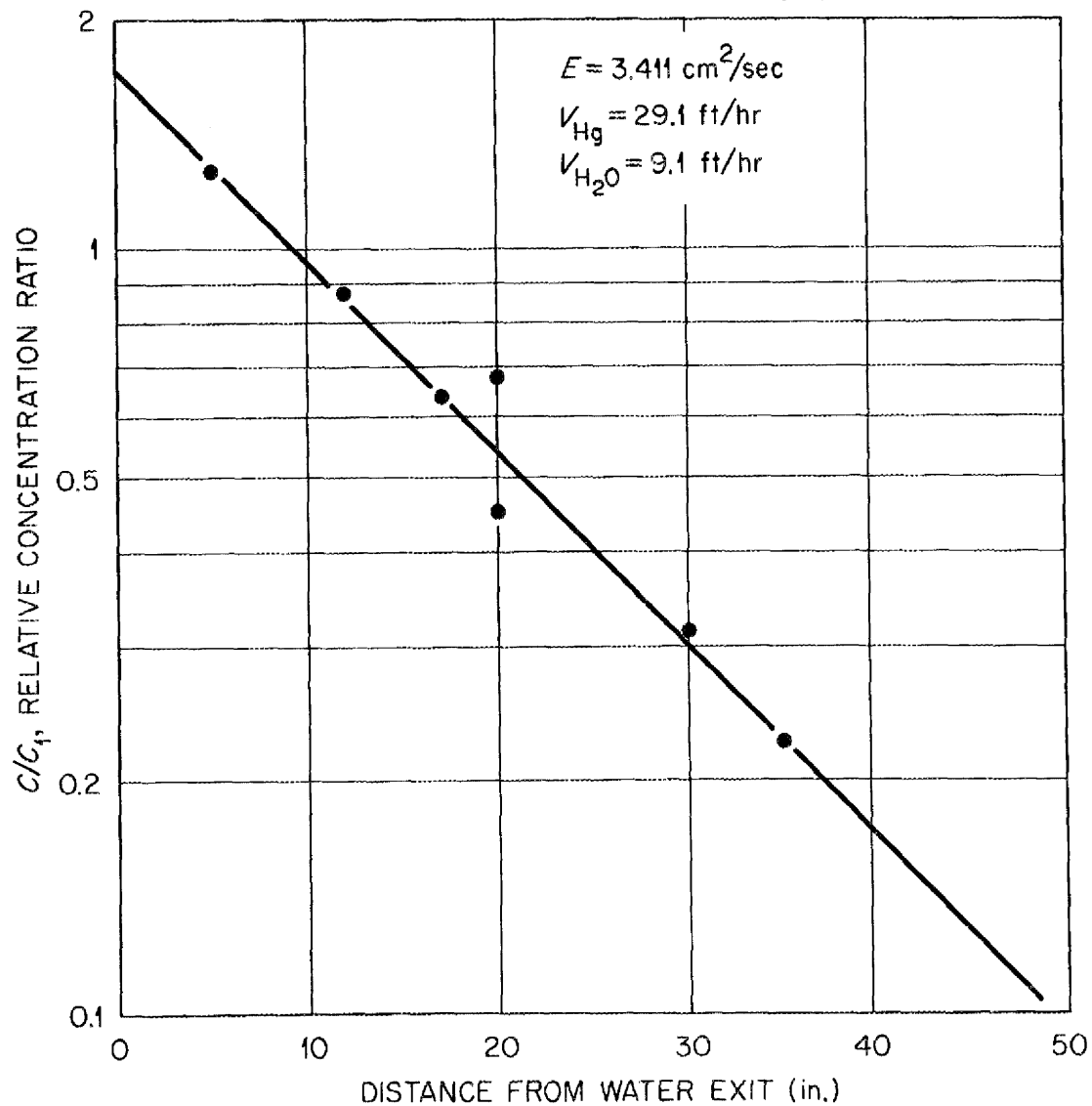
Fig. 10. Variation of Relative Tracer Concentration with Column Length During Countercurrent Flow of Water and Mercury in a 2-in.-diam Column Packed with 3/8-in. Raschig Rings.
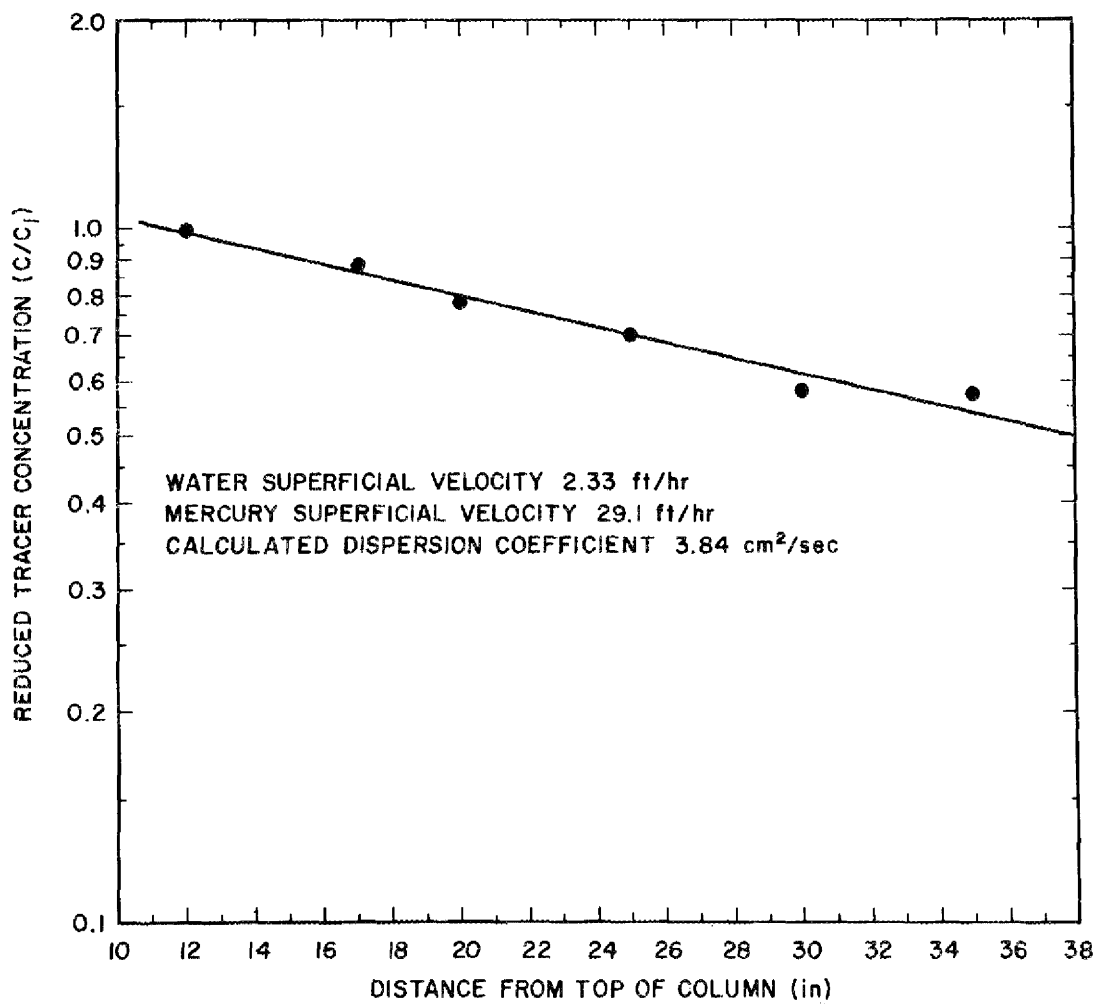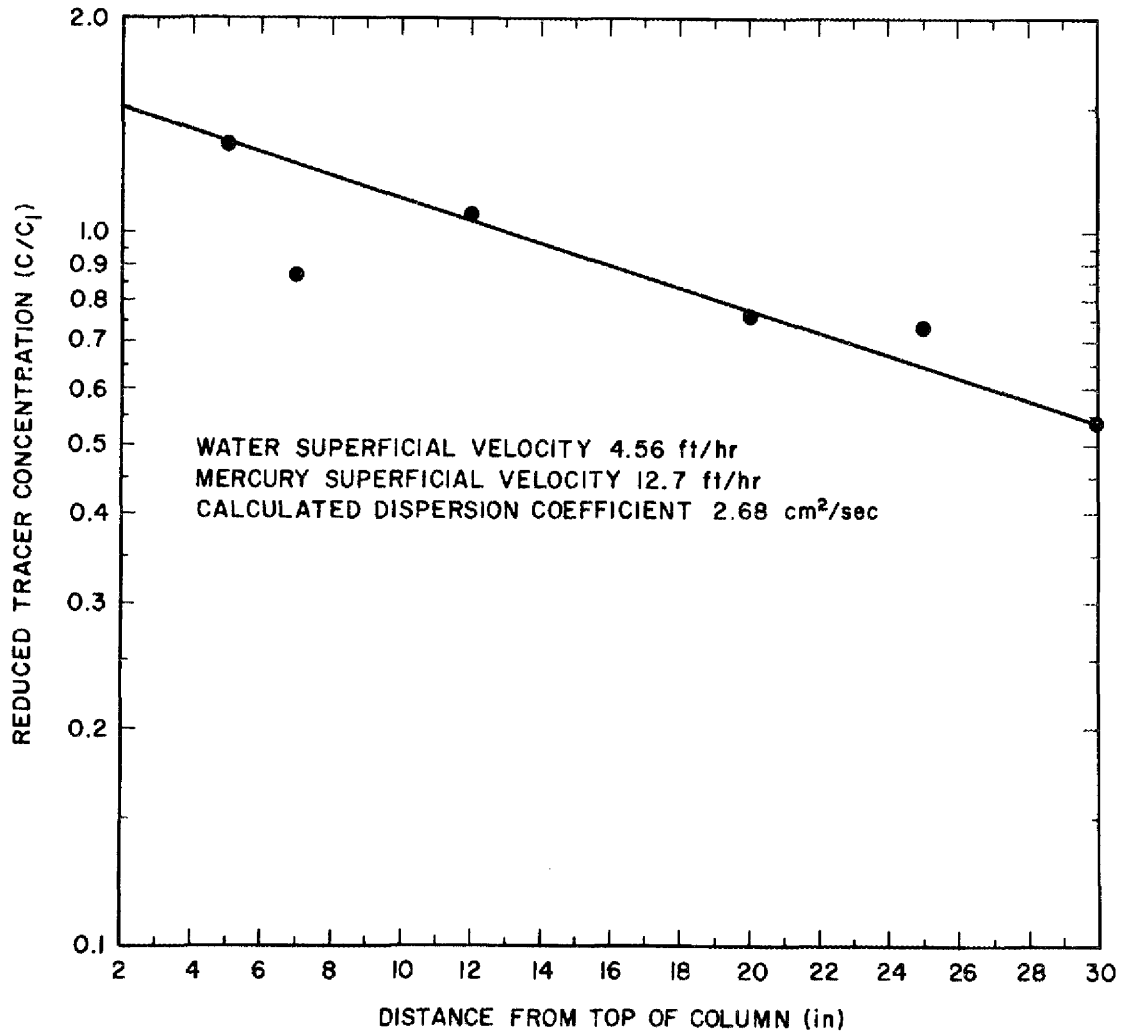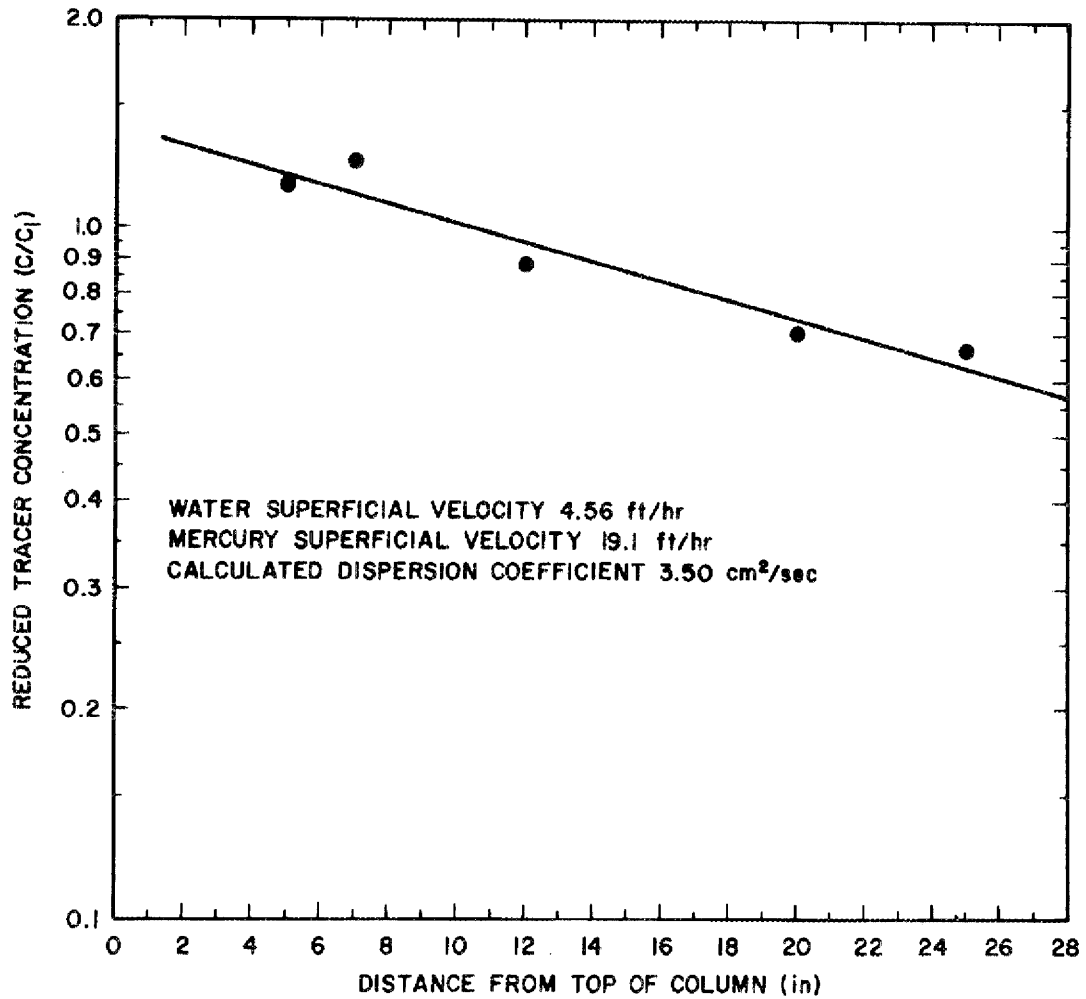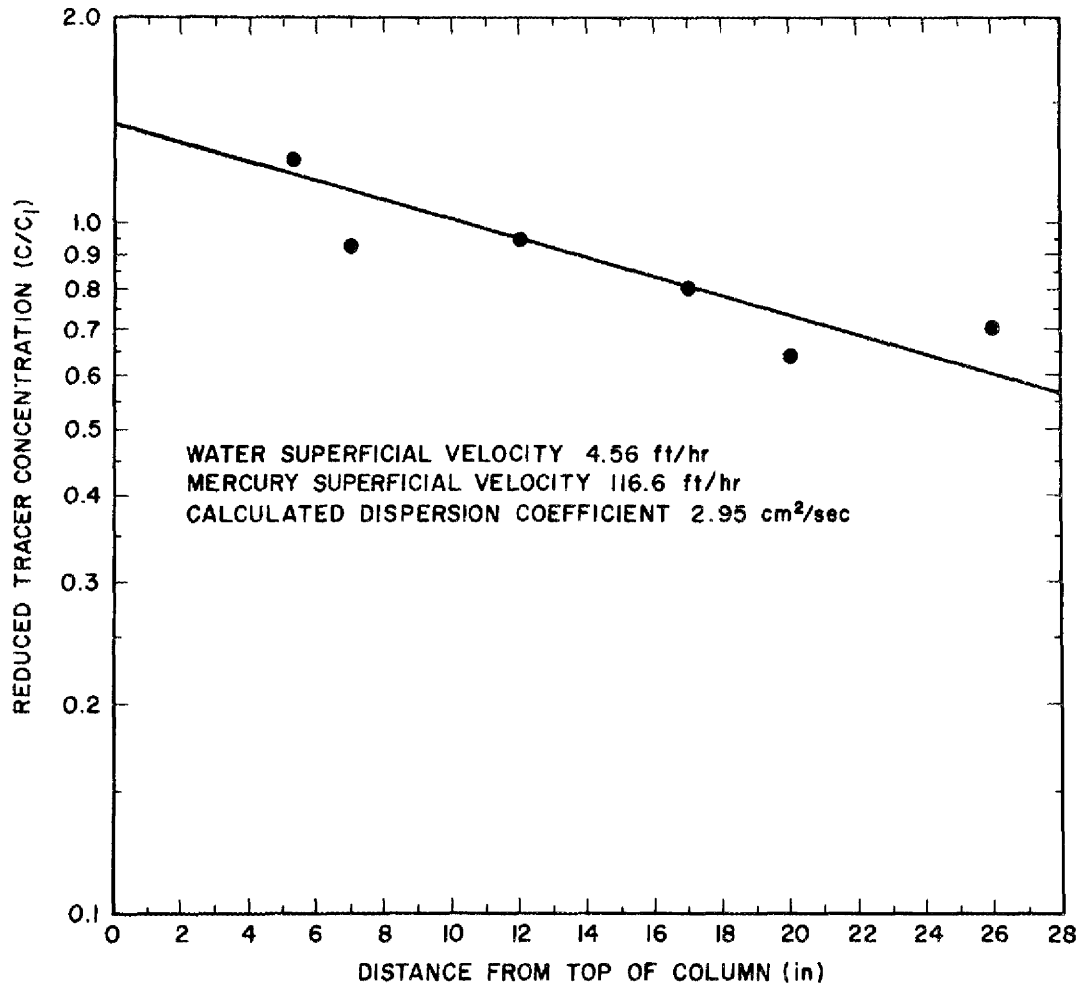
Fig. 11. Steady-State Continuous-Phase Tracer Concentration During Countercurrent Flow of Mercury and Water in a 2-in.-diam Column Packed with 3/8-in. Raschig Rings.

Table 2. Summary of Axial Dispersion Data for Column
Packed with 3/8-in. Raschig Rings

Run No.	Superficial Velocity (ft/hr)		Mercury-to-Water Flow Ratio	Axial Dispersion Coefficient (cm^2/sec)
	Water	Mercury		
1	13.1	87.4	6.67	3.7
2	2.33	29.1	12.5	3.84
4	4.56	58.3	12.7	2.68
5	4.56	87.4	19.1	3.50
6	2.28	121.4	53.2	4.33
8	9.13	29.1	3.19	3.41
11	4.56	116.6	25.5	2.95

ORNL-DWG-71-3803

Fig. 12. Dispersion Coefficients with Countercurrent Flow of Mercury
and Water Through 3/8-in. Raschig Rings.

4. A SIMPLIFIED METHOD FOR ESTIMATING THE EFFECT OF AXIAL DISPERSION ON COUNTERCURRENT COLUMN PERFORMANCE

J. S. Watson   H. D. Cochran, Jr.

In the decade since Sleicher,[2] Miyauchi and Vermeulen,[3] and Hartland and Mecklenburgh[4] published solutions to the continuity equation for countercurrent flow in extraction or absorption towers with axial dispersion, numerous authors have cited their work. Doubtless, many industrial organizations have also employed their solutions. Despite this attention and the obvious practical importance of axial dispersion in many applications, very few attempts[2,3,5,6] have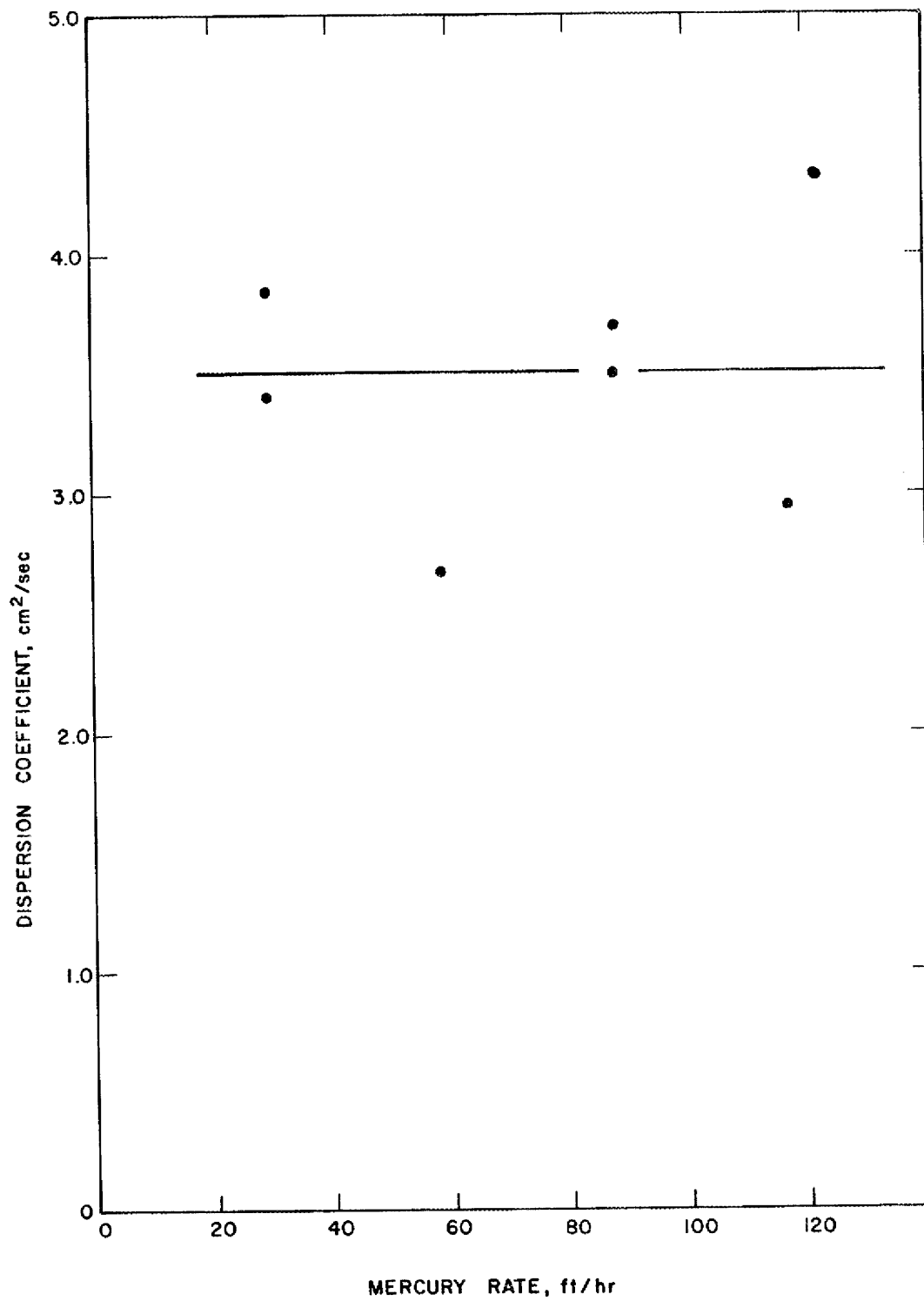 been made to develop a simple, rapid method for estimating the effect of axial dispersion for design purposes or for interpretation of experimental data. Even the simplified methods that have been proposed are complex.

The objective of this study was to develop an expression for column efficiency which consisted of a simple function of the design parameters and directly measurable quantities only. With such an expression, the required column height could be predicted from conventional design information (number of transfer units required under plug flow conditions, height of a transfer unit under plug flow conditions, and axial dispersion coefficient).

4.1 Definition of Column Efficiency

In discussing mass transfer in countercurrent contactors, it is convenient to define a column efficiency, η, which relates the performance of a contactor in which axial dispersion is present to the performance of a contactor in which no axial dispersion occurs (i.e., a plug flow contactor).

Consider a system containing a reference phase x, a second phase y, and a solute which distributes between the phases in a linear manner, as

$$C_x = g + mC_y , \qquad\qquad (3)$$

where

C_x = concentration of solute in the reference phase,

C_y = concentration of solute in the second phase,

g = intercept of equilibrium line,

m = slope of the equilibrium line.

For such a system, the performance of a plug flow contactor can be described in terms of the number of transfer units (NTU) produced, as follows.

For $F \neq 1$,

$$NTU = \frac{\ln \frac{X}{XF + 1 - F}}{F - 1} ,\tag{4}$$

where

NTU = number of overall plug flow transfer units based on the reference phase, x,

F = extraction factor, mV_x/V_y,

V_x = flow rate of the reference phase,

V_y = flow rate of the other phase,

and

$$X = \frac{C_{x(out)} - (g + mC_{y(in)})}{1 - g + mC_{y(in)}} .\tag{5}$$

For $F = 1$,

$$NTU = \frac{1}{X} - 1.\tag{6}$$

Thus, the number of transfer units produced is based on a reference phase and is dependent principally on the changes in solute concentration in the streams and the distribution coefficient between the phases.

The column efficiency has been defined by Sleicher as the ratio of the height of a contactor in which axial dispersion is present to the height of a plug flow contactor that results in the same mass transfer performance; that is,

$$\eta = \frac{HTU_p \cdot NTU}{H} , \qquad (7)$$

where

η = column efficiency,

HTU_p = height of a transfer unit in a plug flow contactor,

H = height of contactor in which axial dispersion is present.

4.2 Column Efficiency for Axial Dispersion in a Single Phase

Miyauchi and Vermeulen[3] obtained a solution for mass transfer with axial dispersion in a system having constant volumetric countercurrent flow rates and a constant equilibrium distribution coefficient. The boundary conditions used were those defined by Danckwerts.[7]

The differential equations defining the solute concentrations in the system were

$$E_x \frac{d^2 C_x}{dZ^2} - V_x \frac{dC_x}{dZ} - k_{ox}a[C_x - (g + mC_y)] = 0 \qquad (8)$$

and

$$E_y \frac{d^2 C_y}{dZ^2} - V_y \frac{dC_y}{dZ} + k_{ox}a[C_x - (g + mC_y)] = 0, \qquad (9)$$

where

E_x, E_y = axial dispersion coefficients in the x and y phases, respectively,

$k_{ox}a$ = the overall mass-transfer coefficient based on the reference phase x,

Z = the distance along the column axis, measured from the reference-phase inlet.

The boundary conditions at $Z = 0$ (x-phase inlet) were as follows:

$$-\left.\frac{dC_x}{dZ}\right|_{Z=0} = \frac{V_x}{E_x}[C_x(1) - C_x(0)] \tag{10}$$

and

$$\left.\frac{dC_y}{dZ}\right|_{Z=0} = 0. \tag{11}$$

At $Z = 1$,

$$\left.\frac{dC_y}{dZ}\right|_{Z=1} = \frac{V_y}{E_y}[C_y(1) - C_y(0)] \tag{12}$$

and

$$\left.\frac{dC_y}{dZ}\right|_{Z=1} = 0. \tag{13}$$

These boundary conditions result from the assumption that there is no dispersive flux across the inlet or outlet boundaries of the column. Consequently, they result in an abrupt change in the concentration at the entrance. The solution to these equations is complex; it is difficult to use for most design purposes since it cannot be solved explicitly for the column height or efficiency. Using the solution, values of the column efficiency were evaluated iteratively from several hundred cases that cover a range of operating conditions. In the generation of these values, the axial dispersion coefficient in the dispersed phase was assumed to be zero. It was found that the results can be approximated over a relatively wide range of conditions by the following simple empirical expression:

$$\eta \approx 1 - \frac{1}{1 + N_{Pex} - F \frac{1}{NTU}} \,, \tag{14}$$

where

$$N_{Pex} = \frac{V_x \, HTU_p}{E_x}.$$

This expression predicts column efficiencies that deviate from the exact values by no more than 0.06 when

$$NTU \leq 2, \tag{15a}$$

$$F \leq 3, \tag{15b}$$

$$\eta \geq 0.20. \tag{15c}$$

and

It is important to note that, because the Peclet number is based on the height of a transfer unit for plug flow, the three required variables--N_{Pex}, F, and NTU--contain only directly measurable quantities or design parameters. The equation gives extremely accurate values for large Peclet numbers where the efficiency approaches unity. Even for NTU = 1, the equation is satisfactory for $N_{Pex} \geq 1$.

Equation (14) was tested for extraction factors from 4 to 0.01, for NTU = 1, 2, and higher values up to 8 or 16 (the dependence on NTU decreases at high NTU), and for $N_{Pe} = 0.1$ to 100 or higher. Several representative curves comparing the estimated efficiency to the exact efficiency are shown in Fig. 13. All of the curves could not be included since some of them lie very near the diagonal. One curve for conditions outside the allowable range, namely, F = 4 and NTU = 2, is included.
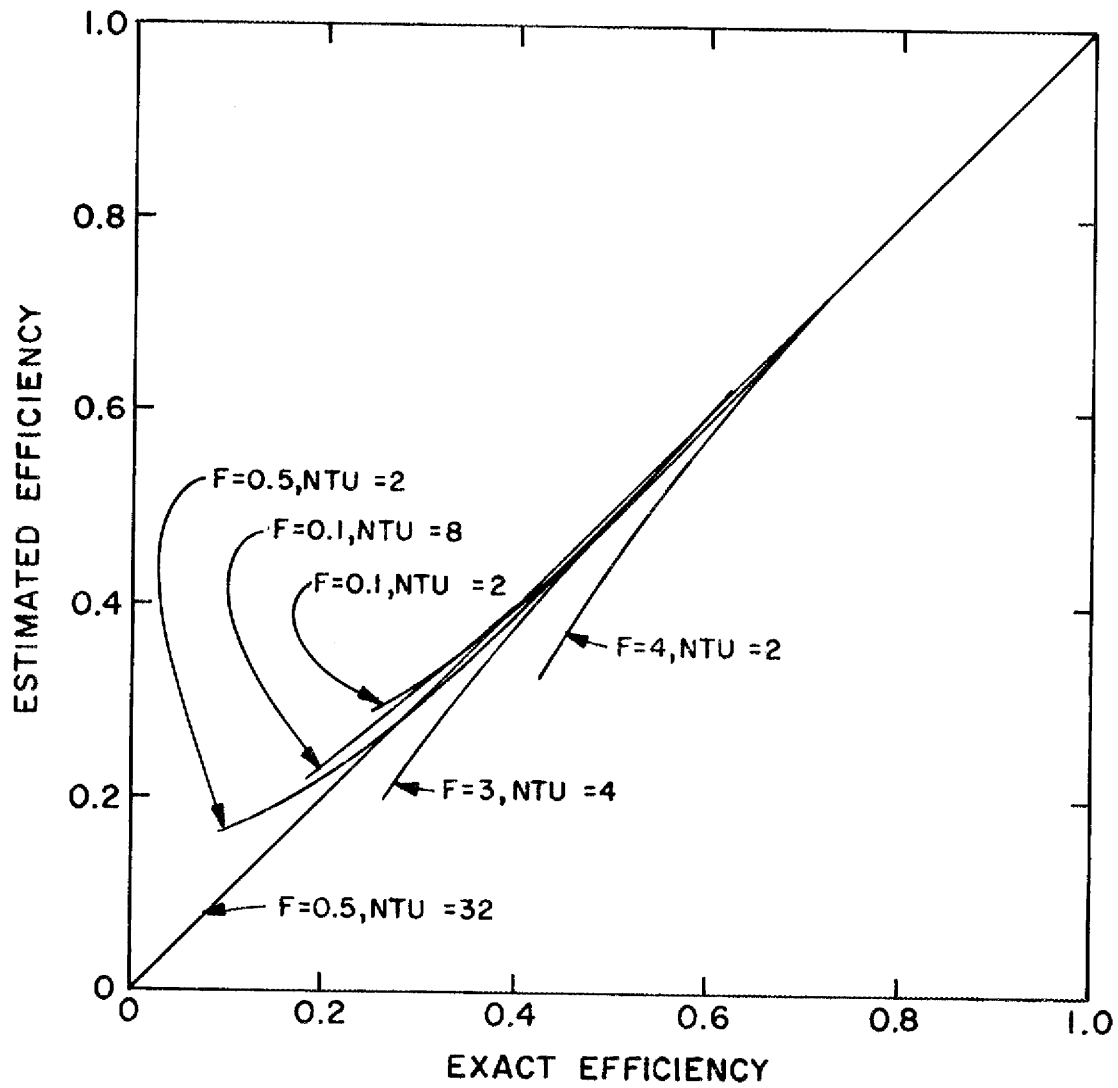
ORNL DWG 70-1474R1

Fig. 13. Comparison of Estimated and Exact Contactor Efficiencies for Axial Dispersion in Only One Phase.

4.3 Column Efficiency for Axial Dispersion in Both Phases

A similar effort was made to fit values of the column efficiency generated from the solution of Miyauchi and Vermeulen with axial dispersion in both phases. In this case, the resulting empirical equation was compared with the tabulated results of McMullen, Miyauchi, and Vermeulen; no new calculations of column performance were made. The column efficiency is given approximately by the following equation:

$$\eta \approx 1 - \frac{1}{N_{Pex} + 1 - F \frac{1}{NTU}} - \frac{F}{N_{Pey} - 1 + F \frac{1}{NTU}} . \tag{16}$$

This equation predicts efficiencies that deviate from the exact values by no more than 0.07 when

$$NTU \geq 2, \tag{17a}$$

$$\eta \geq 0.20, \tag{17b}$$

and when the denominators of both terms on the right are positive. For very low values of N_{Pey} (less than 1.5) and for values of F less than 0.25, the approximate equation becomes slightly overcorrective, and, in turn, predicted efficiencies are too low.

A comparison of efficiency values predicted by Eq. (16) with exact values from the tabulated results of McMullen, Miyauchi, and Vermeulen is given in Fig. 14 for all cases satisfying the specified conditions. The agreement is satisfactory. As in Fig. 13, the accuracy of the predicted efficiencies is found to be highest when the efficiency is greater than 0.50.
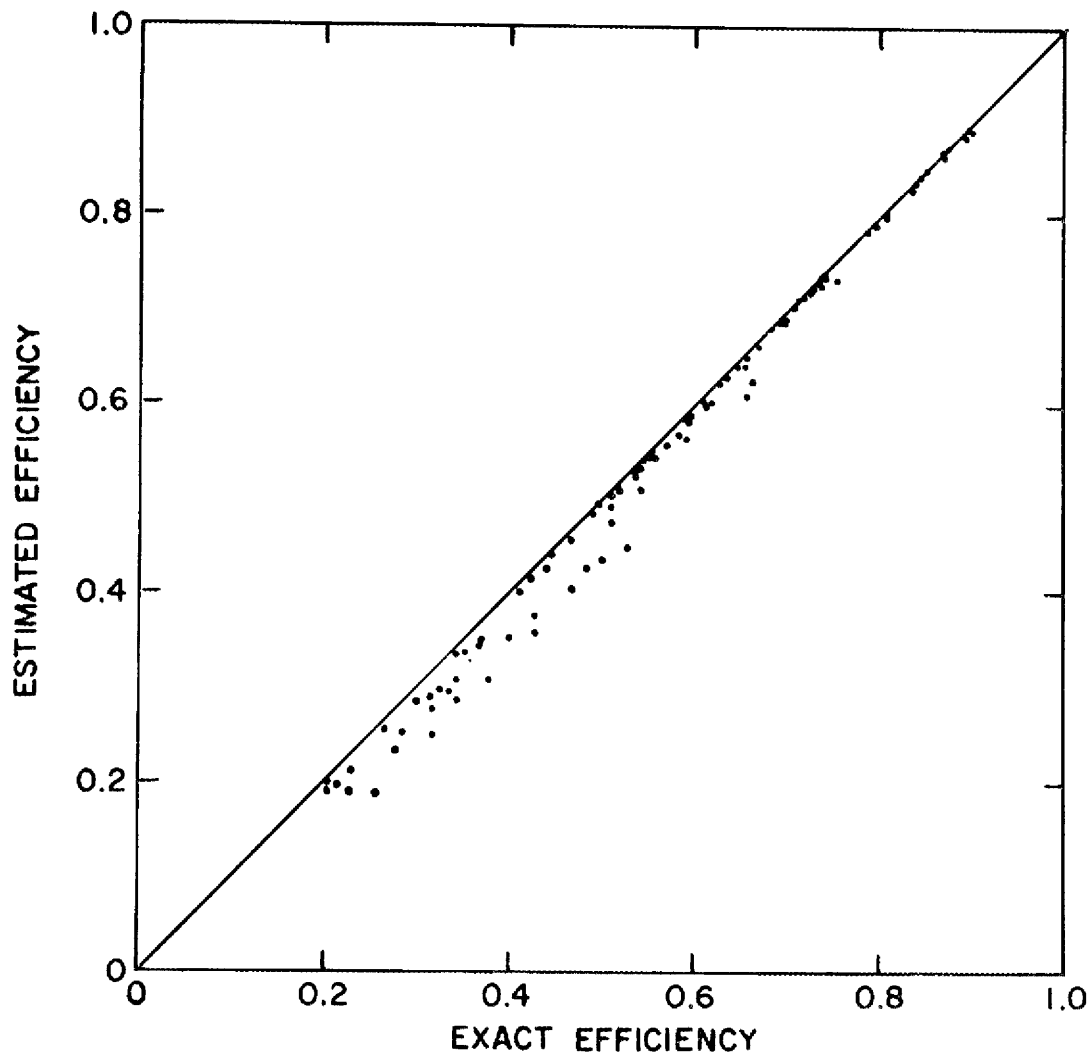
ORNL DWG 70-1475

Fig. 14. Comparison of Estimated and Exact Contactor Efficiencies for Axial Dispersion in Both Phases.

4.4 Prediction of Required Height of Contactors in Which Axial Dispersion Is Present

By combining the relation defining contactor efficiency [Eq. (16)] with the empirical expressions for contactor efficiency when axial dispersion is present, one obtains a relation that can be used to predict the required height of contactors in which axial dispersion occurs in one phase or both phases. The final relation is of the form

$$H = \frac{(HTU) \cdot (NTU)}{\eta} = \frac{(HTU) \cdot (NTU)}{f(N_{Pe}, \, NTU, \, F)} \, . \tag{18}$$

This relation is easily used and is sufficiently accurate for estimating the performance of most countercurrent absorption or extraction columns of interest. Moreover, the accuracy decreases only in cases where the column performance is very poor; in such cases, the estimate will clearly reveal the need for exact solutions. In any event, the estimated efficiency will serve to indicate whether axial dispersion is important in a particular application. The method is believed to be applicable under most conditions encountered in practice, and the accuracy is consistent with the usual uncertainties in values for HTU and N_{Pe}. Although the distribution coefficient may not be constant in some applications, the assumption of a constant distribution coefficient is inherent in the published solutions to the continuity equation. This method of estimation should prove useful in many design studies as well as in making assessments of the effect of dispersion on laboratory- and pilot-scale experiments. Although correlations for axial dispersion coefficients are not readily available, data obtained from several types of contactors have been reported.[8] In many instances, the lack of data on axial dispersion can be used as an argument for using the simple relationships suggested in this study rather than the more complex exact solution. It is believed that less complicated procedures, such as the one described here, will encourage the inclusion of axial dispersion considerations in design problems and stimulate more experimental evaluation and correlation of axial dispersion data.

5. EFFECT OF AXIAL DISPERSION IN PACKED COLUMN CONTACTORS USED FOR MSBR PROCESSING

J. S. Watson   H. D. Cochran, Jr.

Calculations that show the effect of axial dispersion in packed column contactors specified by MSBR processing flowsheets have been made using the method developed for estimating the effect of axial dispersion in countercurrent contactors (discussed in Sect. 4) and values for the axial dispersion coefficient experimentally determined in a 2-in.-diam column packed with 3/8-in. Raschig rings (Sect. 3). The flowsheet calls for packed column contactors in both the protactinium isolation system and the rare-earth removal system. The contactors in each of the systems consist of an upper section and a lower section operating under different conditions. In each case, the number of transfer units required (NTU), the extraction factor (F), and the Peclet Number (N_{Pe}) were estimated for the columns from flowsheet calculations made by McNeese for the reference flowsheet conditions.[9] These values were then used in calculating the column efficiency (η) and the required column length (L^*). The results of these calculations are summarized in Table 3.

In the case of the protactinium isolation columns, where the assumption of a constant distribution coefficient (D) is poor, calculations were made for several values of the distribution coefficient over its range of variation. It was found that the results are largely independent of the value of D. The most important observation was that the efficiencies of the columns are high; that is, dispersion will require the length of the column to be increased by less than 10% over that in which no dispersion occurs. The estimate of HTU (3.2 ft) used in calculating N_{Pe} and L^* was taken from the experimental results of Johnson et al.[10] A value of 3.5 cm^2/sec for E was used in calculating N_{Pe}. This number is based on measurements made with columns packed with 3/8-in. Raschig rings (described in Sect. 3). The calculated column heights are acceptably low.

Table 3. Input Parameters and Results of Calculations with Dispersion Model

	α^a	D	F	N_{Pe}	NTU	η	L* (ft)
Protactinium columns							
Top section		33.4	0.01600	17.6	2-5	0.94	7-17
		16.7	0.03199	17.6	2-5	0.94	7-17
Bottom section		37.3	0.01432	17.6	2-5	0.94	7-17
		0.404	1.325	17.6	2-5	0.94	7-17
Rare-earth columns							
Top section	1.2		1.988	1.5	3-5	< 0.10	> 95
	1.5		1.589	1.5	3-5	0.10-0.20	48-160
	2.0		1.182	1.5	3-5	~ 0.27	35-60
Bottom section	1.2		0.8297	0.61	25	< 0.20	> 350
	1.5		0.6718	0.61	25	< 0.20	> 350
	2.0		0.5038	0.61	25	~ 0.15	~ 500

[a] α = Rare-earth–thorium separation factor.

For the rare-earth removal system, rare earth--thorium separation factors (α) of 1.2, 1.5, and 2.0 were assumed. The HTU and axial dispersion coefficient values (i.e., 3.2 ft and 3.5 cm^2/sec, respectively) that were used in making calculations for the protactinium system were also assumed to apply for the rare-earth columns. In the upper column, efficiencies were quite low and strongly dependent on N_{Pe} and NTU. It appears likely that column heights will be excessive in this section. In the lower part of the rare-earth system, low efficiencies and the need for very long columns are certain since the Peclet number is low and the number of required transfer units is high. It is concluded that axial dispersion preventers or staged columns will be necessary in the rare-earth removal system. A study of devices for reducing axial dispersion in columns has been initiated.

6. AXIAL DISPERSION IN AN OPEN BUBBLE COLUMN

M. S. Bautista   L. E. McNeese

Bubble reactors are commonly used in industrial processes to carry out reactions between a gas phase and a liquid phase. This type of reactor is being developed for recovering uranium from molten salt streams. In operation, fluorine gas is bubbled countercurrently through the molten salt in an open column. Fluorine, which is absorbed in the molten salt, reacts with the uranium to form UF_6. The volatile UF_6 is carried out of the column in the gas stream. One problem associated with a bubble reactor is the inherent axial dispersion caused by the ascending bubbles. The effect of axial dispersion is an averaging of concentrations over the length of the column and hence a decrease in the performance achievable with a countercurrent system. The purpose of this investigation was to measure axial dispersion coefficients in a bubble column for a range of liquid and gas flow rates.

The experimental approach consisted of measuring photometrically the axial concentration gradient of a tracer, $Cu(NO_3)_2$, which was added to the bottom of a column in which water and air were in countercurrent flow. The axial dispersion coefficient was then calculated from the measured concentration gradient. In a previous investigation, the tracer concentration was determined by measuring the transmittance of the aqueous phase containing the tracer directly through the glass column by positioning a light source and a light-detecting device (photo-resistor) diametrically opposite each other at points along the column; the gradient was determined by positioning the light source and photo-resistor at known positions along the length of the column. However, the rising bubbles and the variation of the optical properties of the column wall made accurate transmittance measurements difficult. To eliminate these problems, we devised a technique for measuring the tracer concentration by slowly withdrawing a small amount of solution from the column, pumping the solution through a photocell for analysis, and returning the solution to the column at the same elevation.

6.1 Mathematical Model

The mathematical model used for defining the axial dispersion coefficient is analogous to Fick's law. At steady state, a mass balance on the tracer, performed on a differential height of column, yields the relation

$$D \frac{d^2C}{dZ^2} = -u \frac{dC}{dZ}, \tag{19}$$

where

C = tracer concentration at height Z,

u = superficial liquid velocity,

D = axial dispersion coefficient,

Z = height above reference point.

The assumptions that were used in deriving this equation were as follows:

1. The tracer concentration gradients in the angular and radial directions are negligible.

2. The dispersion coefficient is independent of column length.

3. The effect of molecular diffusion is negligible.

The boundary conditions employed to solve this differential equation were:

(1) at $Z = 0$, $C = C_o$;

(2) at $Z = L$, $uC = -D \frac{dC}{dZ}\Big|_{Z=L}$. (20)

With these boundary conditions, the solution of the differential equation is:

$$\frac{C}{C_o} = \exp\left(-\frac{uZ}{D}\right),$$ (21)

where

C_o = tracer concentration at reference point, $Z = 0$.

Thus, the axial dispersion coefficient can be determined by plotting the logarithm of (C/C_o) vs Z, which should produce a straight line having the slope $-u/D$.

6.2 Experimental Equipment

A schematic flow diagram of the experimental system is shown in Fig. 15. Laboratory air entered the bottom of the column through a 0.04-in.-ID stainless steel tube, and distilled water was pumped to the top of the column through a disperser that was used to distribute the water uniformly across the column cross section. The liquid level in the column was controlled by adjusting the height of the jackleg through which the water exited from the column. Tracer was injected into the bottom of the column through a stainless steel tube.
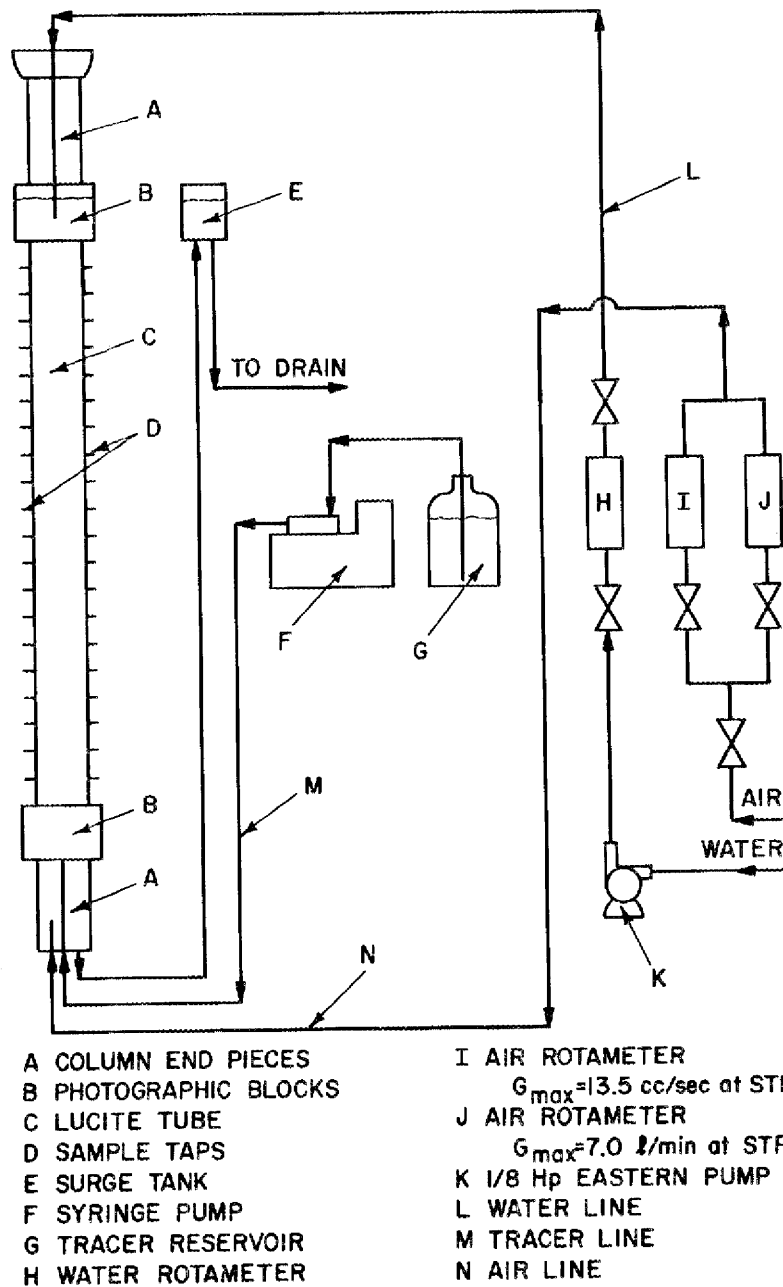
A COLUMN END PIECES
B PHOTOGRAPHIC BLOCKS
C LUCITE TUBE
D SAMPLE TAPS
E SURGE TANK
F SYRINGE PUMP
G TRACER RESERVOIR
H WATER ROTAMETER

I AIR ROTAMETER
  $G_{max}=13.5$ cc/sec at STP
J AIR ROTAMETER
  $G_{max}=7.0$ l/min at STP
K 1/8 Hp EASTERN PUMP
L WATER LINE
M TRACER LINE
N AIR LINE

Fig. 15. Flow Diagram for Equipment Used in Measuring Axial Dispersion Coefficients in an Open Column in Which Air and Water Are in Countercurrent Flow.

6.2.1 Bubble Column; and Air, Water, and Tracer Feed Systems

The bubble column consisted of three sections: a Lucite tube
(2 in. in inside diameter and 72 in. long), two Lucite photographic
blocks located at the ends of the tube, and two glass end pieces at-
tached to the blocks. Twenty sampling taps, spaced 3.5 in. apart
along the length of the tube, were used for measuring the tracer
concentration profile. The first tap was positioned 17.75 in. above
the bottom of the column. Each tap consisted of two Lucite tubes lo-
cated diametrically opposite each other. One tube was used for with-
drawing solution from the column, and the other was used for returning
solution. The photographic blocks were made by drilling a 2-in.-diam
hole through a 3 x 3 x 3 in. Lucite block. Photographs could be taken
through the blocks to determine the average bubble diameter.

Laboratory air entered the bottom of the column through a 0.04-in.
stainless steel tube; the gas inlet point was approximately 4-5/8 in.
above the bottom of the column. The gas flow rate was measured by one
of two rotameters placed in parallel. The maximum volumetric flow rate
was 117 cm^3/sec for the largest rotameter, while the maximum flow rate
was 13.5 cm^3/sec for the other rotameter. To regulate the gas flow rate,
a valve was located upstream of each rotameter. All air flow rates given
in this report are volumetric flow rates measured at the temperature and
pressure at the top of the column.

Distilled water was pumped to the top of the column by a 1/8-hp
Eastern[*] pump. Water was distributed uniformly over the column cross
section by a disperser made by drilling four holes through the sides of
a sealed 1/8-in.-ID stainless steel tube. The liquid flow rate was meas-
ured by a rotameter with a maximum flow rate of 3.5 cm^3/sec and was con-
trolled by two valves, one located upstream and one located downstream
of the rotameter.

---

[*]Eastern Industries, Inc., 100 Skiff Street, Hamden, Connecticut.

The tracer was injected through a stainless steel tube into the bottom of the column by a Harvard Variable Speed Continuous Automatic Infusion Pump. The point of injection was 11-7/8 in. above the bottom of the column.

6.2.2 Solution Sampling and Analysis System

A typical pump and photocell utilized for measuring the tracer concentration in the solution withdrawn from the column are shown in Fig. 16. Details of the pump design are shown in Fig. 17. Each of the pumps was fabricated from Lucite and had a 0.465-in.-long, 2-in.-diam pump body. The chamber in which the impeller operated consisted of a 15/16-in.-diam, 3/8-in.-deep hole drilled along the axis of the pump body. The chamber was sealed by a 3/8-in.-thick, 1-in.-diam Lucite seal plate that was machined to a diameter of 15/16 in. over a distance of 1/8 in. The machined end of the seal plate was inserted into the pump body chamber. The inlet to the pump consisted of a 1/8-in.-diam hole drilled on the axis of the seal plate. The outer 1/4 in. of the inlet was drilled and tapped to receive a 1/8-in.-ID, 1-in.-long section of stainless steel tubing. The pump outlet consisted of a 1/8-in.-diam hole through the pump body; the outlet was tangential to the surface of the pump chamber. The outlet was also provided with a 1-in. section of 1/8-in.-diam stainless steel tubing. The pump impeller consisted of a 3/4-in.-long, Teflon-coated magnet, which was magnetically coupled to the pump drive system.

Details of the photocell design are shown in Fig. 18. The cell body, fabricated from Lucite, was 1 in. in diameter and 1.75 in. long. A 0.438-in.-diam hole was drilled from both ends of the cell body in such a manner that a 1/8-in.-thick partition, 0.5 in. from one end of the cell body, was formed. The cell compartment was formed by gluing a 0.438-in.-diam, 1/8-in.-thick Lucite disk (shaded area) inside the drilled hole, 0.5 in. from the other end of the cell body. The inlet and the outlet of the
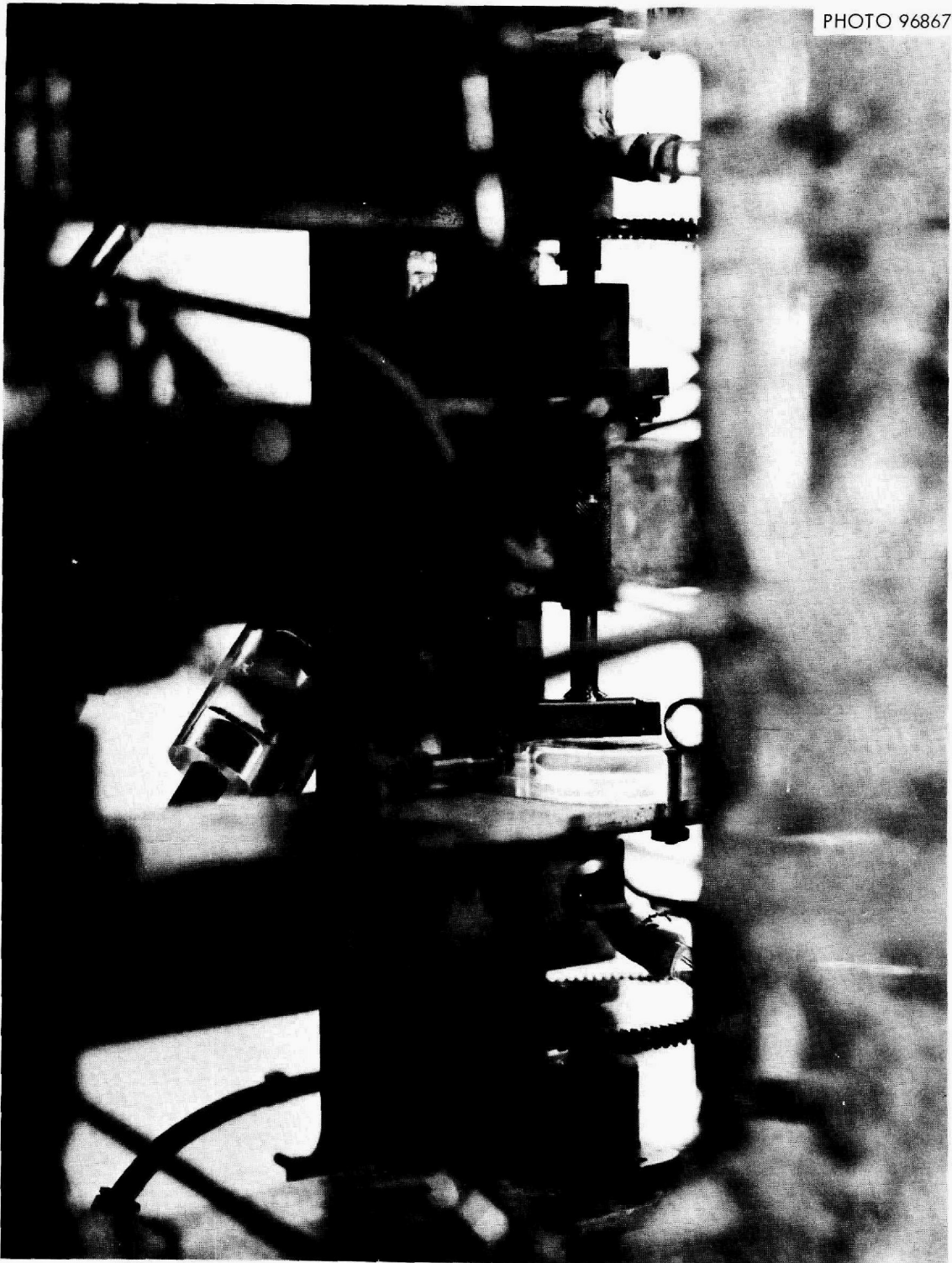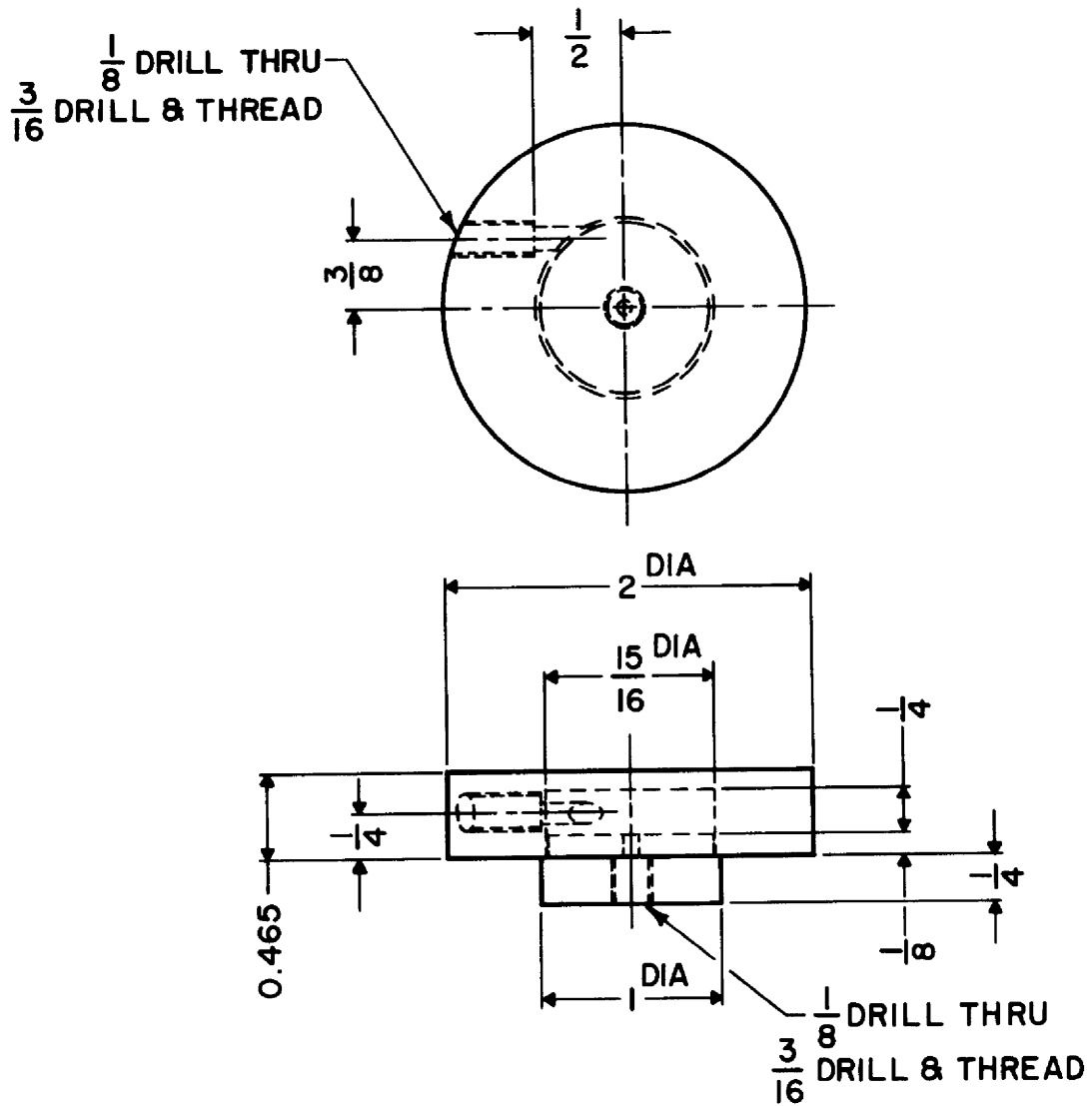
PHOTO 96867

Fig. 16. Pump and Photocell Used for Measuring Tracer Concentration
in Studies of Axial Dispersion in Open Columns.

ORNL DWG 71-13

$\frac{1}{8}$ DRILL THRU

$\frac{3}{16}$ DRILL & THREAD

$\frac{1}{2}$

$\frac{3}{8}$

$2\frac{DIA}{}$

$15\frac{DIA}{16}$

$\frac{1}{4}$

$\frac{1}{4}$

$\frac{1}{4}$

$\frac{1}{4}$

$\frac{1}{8}$

0.465

$1\frac{DIA}{}$

$\frac{1}{8}$ DRILL THRU

$\frac{3}{16}$ DRILL & THREAD

NOTE: ALL DIMENSIONS ARE IN INCHES.

Fig. 17. Details of the Pump Design.

ORNL DWG 71-14
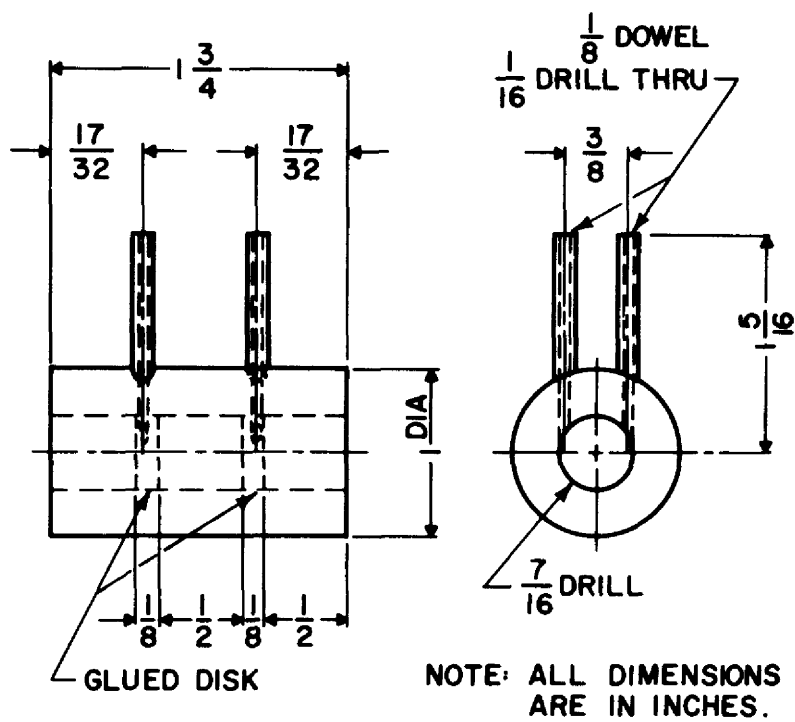
Fig. 18. Details of the Photocell Design.

cell were formed by drilling two 1/16-in. holes through the solid portion of the body, tangential to the inner circular surface of the cell compartment. Two short sections of 1/16-in.-ID Lucite tubing were inserted into these holes.

A trap was provided between each sample outlet and the pump inlet to prevent accumulation of bubbles inside the pump. These traps consisted of Pyrex tees that were positioned in such a manner that one of the legs pointed upward. A small section of clamped rubber tubing was fitted over the leg pointing upward, and air was removed from the trap by opening the clamp. To purge the cell and the pump of air, another Pyrex tee constructed in the same manner was placed between the photocell outlet and the sampling tap. The sampling tubes, trap, pump, photocell, and purge tee were connected with rubber tubing.

The light source for the photocell was a GE 253X bulb, and the transmittance of the cell was measured by a Clairex 707L photoresistor, which has maximum sensitivity at a wavelength of 6150 Å. To collimate the light passing through the cell, the light source and the photoresistor were mounted inside 0.436-in.-OD, 6-in.-long brass tubes that were inserted into the outer compartments of the cell.

The pump drive apparatus, shown in Fig. 16, consisted of a permanent iron magnet firmly attached to an iron rod, a chuck employed to adjust the height of the magnet above the pump, and a sprocket wheel bolted to the iron shaft that supported the chuck.

The main drive system for the pumps consisted of two drive shafts, one of which was located on each side of the column. The shafts were driven at the same speed by a variable-speed electric motor. Drive sprockets were mounted on the shafts, and nonslip sprocket belts connected the drive sprockets with the pump sprockets.

6.2.3 Electronics System

The electrical schematic diagram of a cell circuit is shown in
Fig. 19. The electrical signal from the photoresistor is amplified by
a transistorized operational amplifier circuit and displayed on a
Honeywell Brown recorder (voltage range, -0.5 to 10.5 mV). Basically,
the span adjustment regulates the amplifier feedback, and the zero ad-
justment controls the amplifier input voltage. The 20 electrical cir-
cuits for the cells were connected to the recorder by two 10-position
selector switches that allowed the desired cell reading to be displayed.

6.3 Calibration of Photocells

6.3.1 Relation Between Relative Tracer Concentration and Cell Reading

A relation between the relative tracer concentration (C_i/C_o) and
the photocell reading displayed on the recorder was developed from the
limiting case of Beer's law. Beer's law can be expressed in terms of
the transmittance of the cell as

$$T = \exp(-abc), \tag{22}$$

where

T = transmittance,

a = molar extinction coefficient,

b = cell length,

c = tracer concentration.

By a Taylor expansion of the exponential, $(1 - T)$ can be shown to be
directly proportional to the tracer concentration for dilute concentra-
tions. It is assumed that the photocell reading is proportional to
$(1 - T)$ and, therefore, proportional to the tracer concentration. Using
this approximation and assumption, the following equation can be derived:
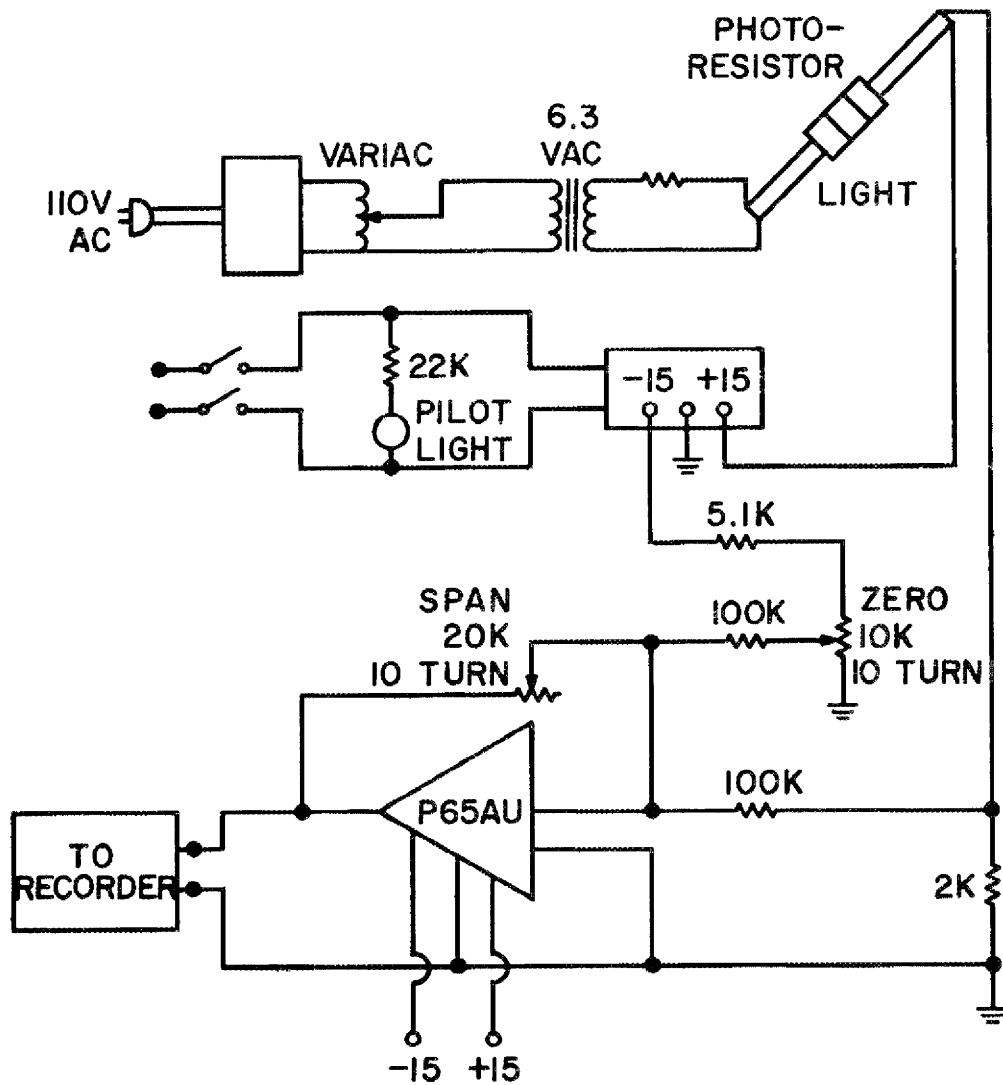
ORNL DWG 71-15

Fig. 19. Electrical Schematic Diagram of a Cell Circuit.

$$\frac{C_i}{C_o} = \frac{\dfrac{R_{ei} - R_{wi}}{R_{si} - R_{wi}}}{\dfrac{R_{eo} - R_{wo}}{R_{so} - R_{wo}}} \quad ,$$

(23)

where

C_i/C_o = relative tracer concentration at column height Z,

R_e = experimental cell reading,

R_s = standardized, calibrated cell reading,

R_w = cell reading with distilled water,

i = ith cell (subscript),

o = reference cell (subscript).

The advantage of this approach is that a directly determined relation between the cell reading and the tracer concentration is not required.

6.3.2 Method for Calibrating Photocells

In calibrating the photocells, it was necessary (1) to determine the maximum tracer concentration for which the linear approximation between the fraction of incident light absorbed (absorbance) and the tracer concentration would be valid, and (2) to confirm the assumption of a linear relationship between the cell reading and the tracer concentration. Figure 20 shows results which verify that behavior corresponding to Beer's law was observed. In this examination, a Beckman infrared spectrophotometer and quartz cells (1 cm in length) were used. The data were obtained by varying the wavelength of the incident light for several tracer concentrations and recording the transmittance for each. The maximum sensitivity of the photoresistor occurred at a wavelength of 6150 $\overset{\circ}{\text{A}}$. At this wavelength, a $Cu(NO_3)_2$ tracer concentration
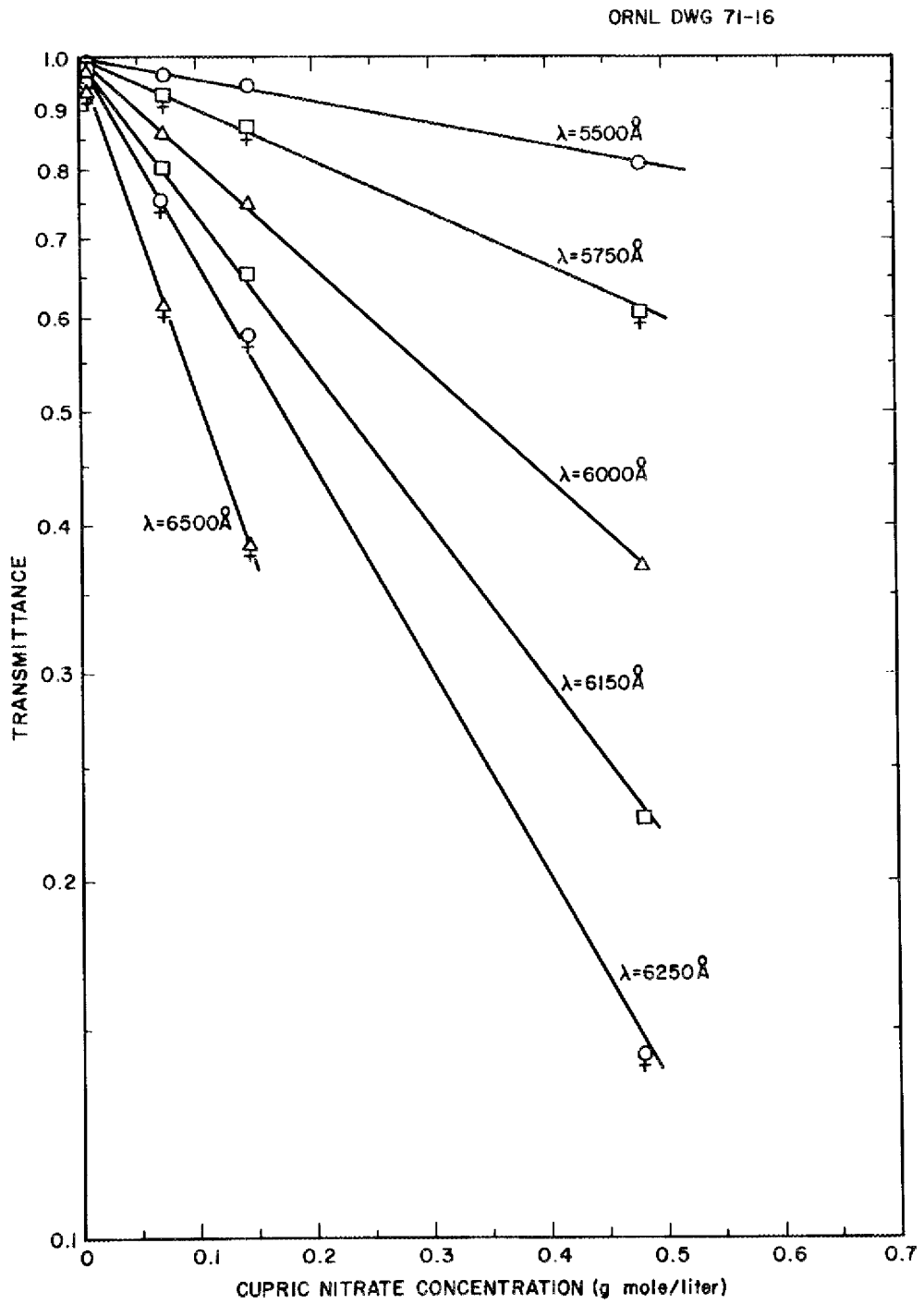
ORNL DWG 71-16

Fig. 20. Verification of Beer's Law Behavior for $Cu(NO_3)_2$ Tracer.

of 0.045 M resulted in an absorbance of 0.13. The absorbance based on
the linear approximation was calculated by using this concentration and
the molar extinction coefficient at 6150 Å; the error in absorbance
caused by the linear approximation was only 6% of the actual absorbance.
The tracer concentration of 0.045 M was chosen as the upper limit for the
linear approximation. The assumption of a linear relation between the
cell reading and the tracer concentration is verified by the data shown
in Fig. 21. In obtaining these data, the readings of two cells were
measured at four tracer concentrations.

The 20 photocells were calibrated initially at tracer concentrations
below the experimentally determined concentration limit by the following
procedure. First, the column was filled with distilled water. Then the
pumps were activated, and their pumping rates were adjusted to 0.12 cm^3/sec.
A 15-min period was allowed for the cells to reach thermal equilibrium.
The cell readings with distilled water were zeroed on the recorder by ad-
justing the voltage input to each cell amplifier. Next, the bottom cell
was disconnected from the column and filled with a 0.041 M $Cu(NO_3)_2$ solu-
tion. The amplifier feedback of the cell was adjusted so that the cell
reading on the recorder was 95% of full scale. The bottom cell was re-
connected to the system. Air flow through the column was then started
at a volumetric flow rate of 4.30 cm^3/sec. The infusion pump was started,
and the tracer flow rate was adjusted to 0.407 cm^3/sec. Injection of
tracer was terminated when the bottom cell reading on the recorder was
80% of full scale. A uniform tracer concentration was assumed to be
present in the column when the top cell reading maintained a constant
value for 15 min. The amplifier feedback of the 19 cells was then ad-
justed so that all cell readings were equal to the reading of the bottom
cell. Finally, the column was drained, flushed, and refilled with dis-
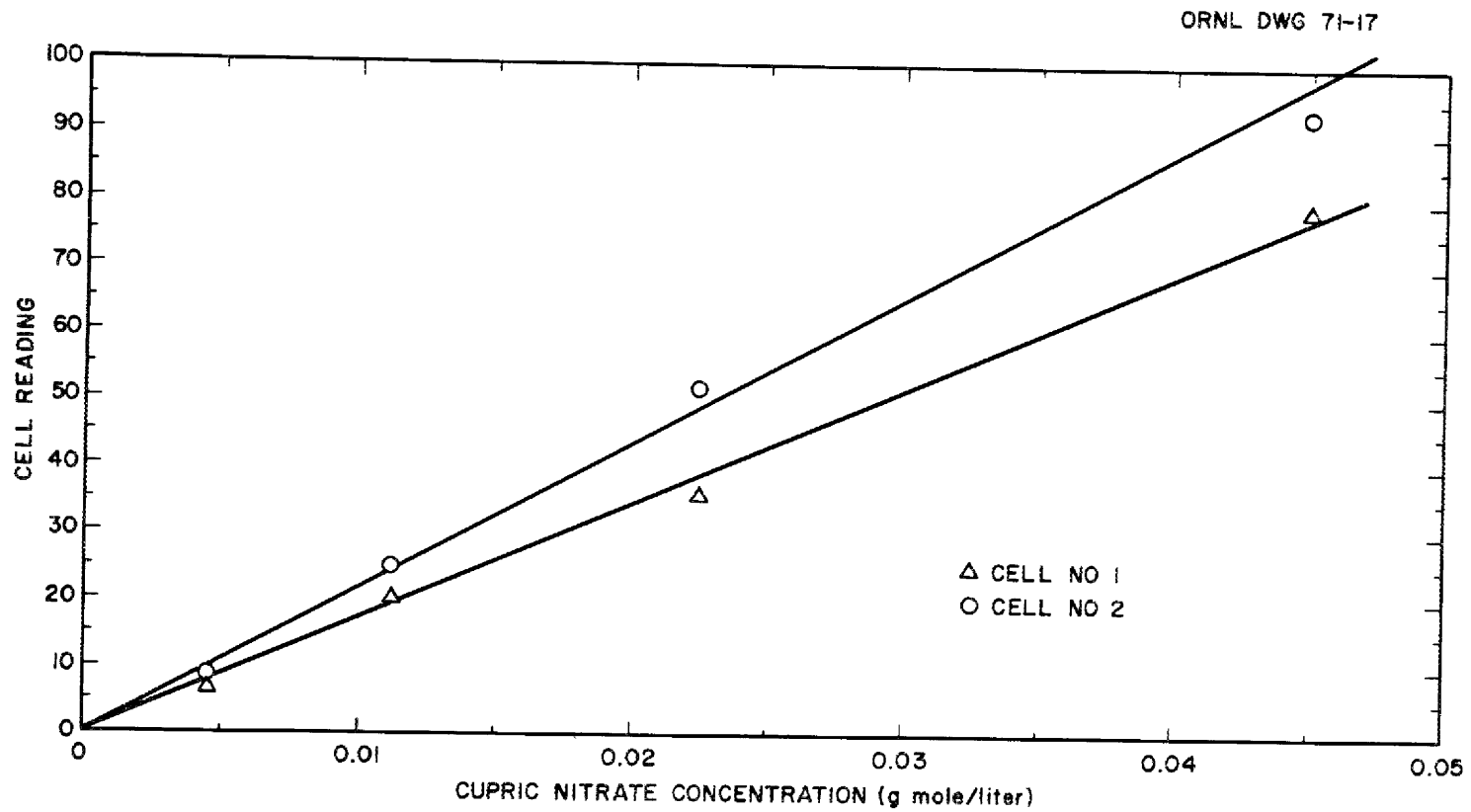tilled water in preparation for experimental work.

Fig. 21. Cell Reading vs Tracer Concentration.

6.3.3 Preparation of Tracer Solution

Preparation of the tracer involved dissolving 230 g of laboratory-grade $Cu(NO_3)_2 \cdot 3H_2O$ crystals in a 2-liter volumetric flask half-filled with distilled water, adding 20 ml of concentrated nitric acid, and diluting to volume with distilled water. The $Cu(NO_3)_2$ concentration was approximately 0.48 $\underline{M}$.

The nitrate anion was selected to prevent reduction of the cupric ion. The tracer was acidified with concentrated nitric acid to further ensure against reduction of the cupric ion.

6.4 Experimental Procedure

The cells were calibrated at the beginning of each day. The calibration procedure can be described as follows. Distilled water was passed through the column with the cell pumps operating at the rate of 0.12 cm^3/ sec. A period of approximately 30 min was allowed to ensure complete removal of tracer from previous runs and to obtain thermal equilibrium in the cells. Cell readings for distilled water were then recorded. Next, the second set of readings required for calibrating the cells was obtained. Air flow was started through the column at a volumetric flow rate of 4.5 liters/min, the water flow was terminated, and tracer was injected into the column by operating the infusion pump at the rate of 0.41 cm^3/sec. The injection of tracer was stopped when the recorder reading of the bottom cell reached 80% of full scale, and the tracer solution was allowed to mix in the column. A uniform tracer concentration was assumed to be present when the reading of the top cell maintained a constant value for 10 min. Cell readings for the standardized tracer concentration were then recorded.

At the beginning of an experiment, the desired air and water flow rates were set. Also, the liquid level in the column was adjusted to

prevent excessive liquid entrainment in the air stream leaving the top of the column. An appropriate setting for the flow rate of the tracer was chosen to ensure that the tracer concentration at the bottom of the column would have the desired value when steady state was reached. To avoid gas buildup inside the pumps, the traps were periodically purged of air. Steady state was assumed to have been reached when the reading for the top cell maintained a constant value for 10 min. To ensure that steady-state conditions existed, the stability of the reading for the bottom cell was also observed. The cell readings were then recorded, and the subsequent experimental run was started by readjusting the water, air, and tracer flow rates.

At the end of each day, the pumps were stopped and the column was drained and refilled with distilled water. Water was fed through the column for 30 min with the pumps activated in order to remove the tracer from the cells. Cell readings taken at this time were compared with those recorded at the beginning of the experiment. If the final value for a particular cell deviated by more than 5% from the initial value, data from that particular cell were discarded.

6.5 Experimental Results

Experimental data obtained during this study are presented in Figs. 22-42, which are plots of the measured values of the tracer concentration at various points along the column for a range of operating conditions. In general, the data points deviate only slightly from the expected linear relationship; this deviation is believed to be the result of random scatter in the data. The axial dispersion coefficient for each experiment was calculated by a least-squares method.

Values for the axial dispersion coefficient are summarized in Fig. 43, where the dispersion coefficient is plotted as a function of the volumetric gas flow rate at the top of the column.
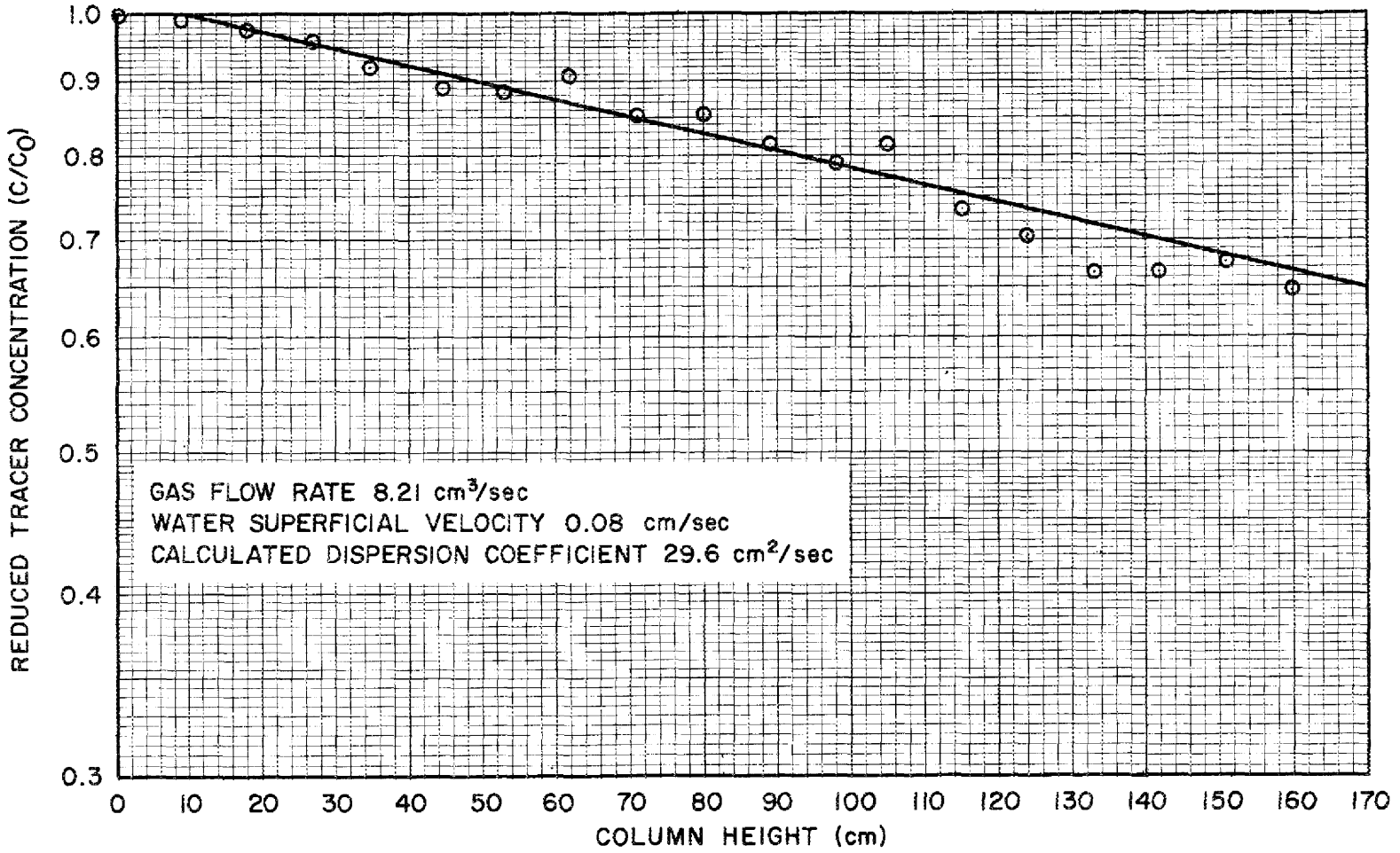
Fig. 22. Variation of Reduced Tracer Concentration with Column
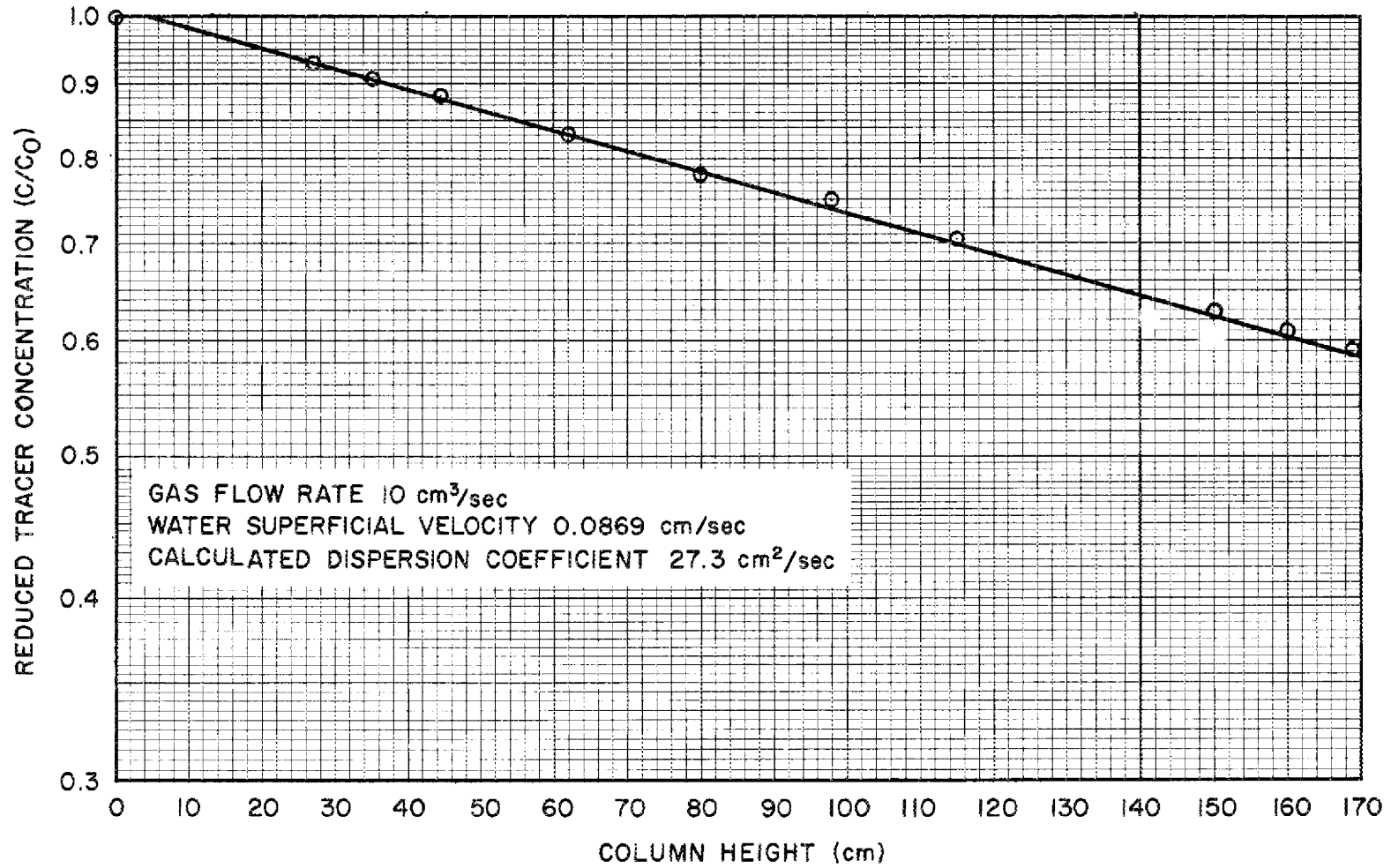Height for Run 1.

Fig. 23. Variation of Reduced Tracer Concentration with Column
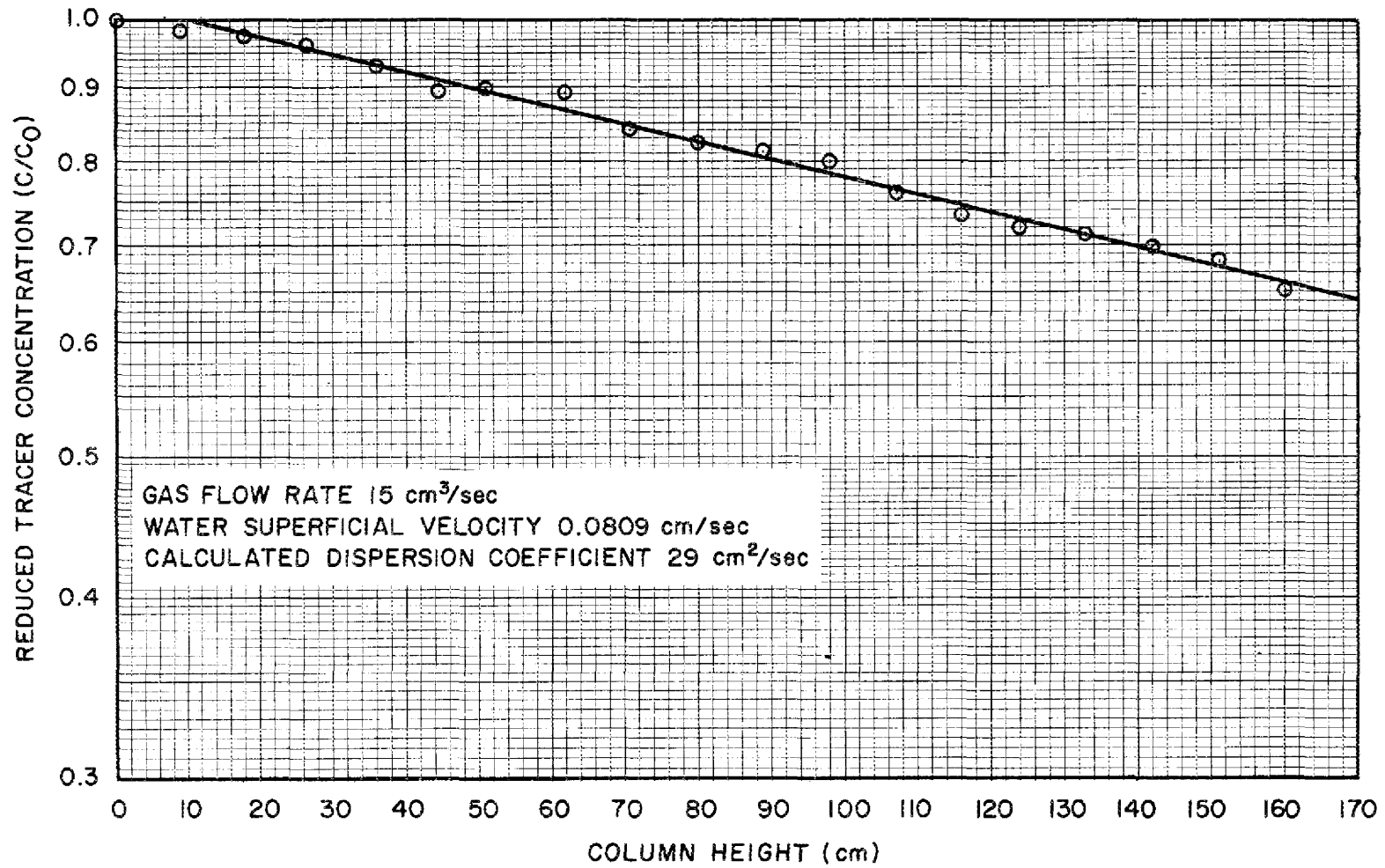Height for Run 2.

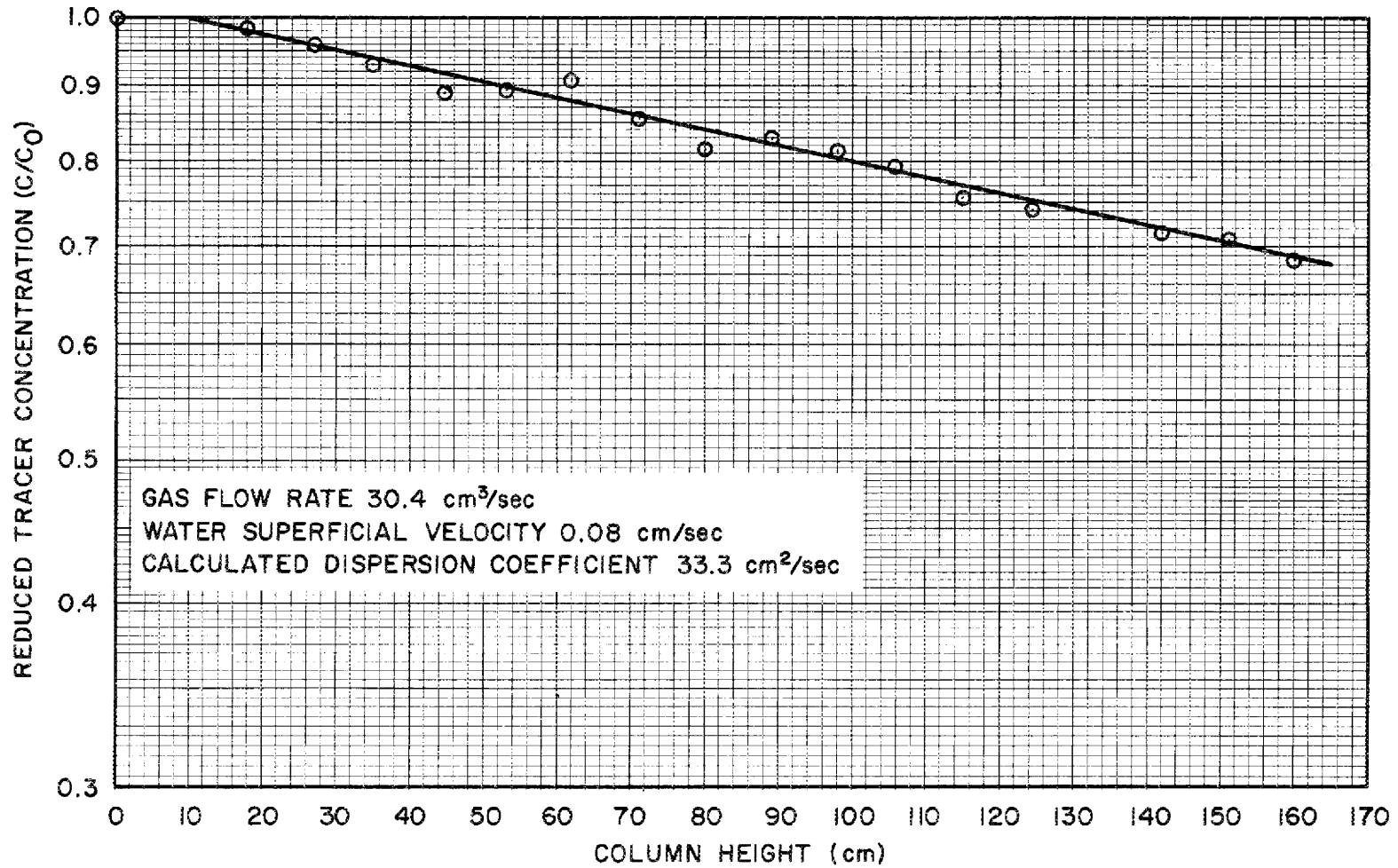Fig. 24. Variation of Reduced Tracer Concentration with Column
Height for Run 3.

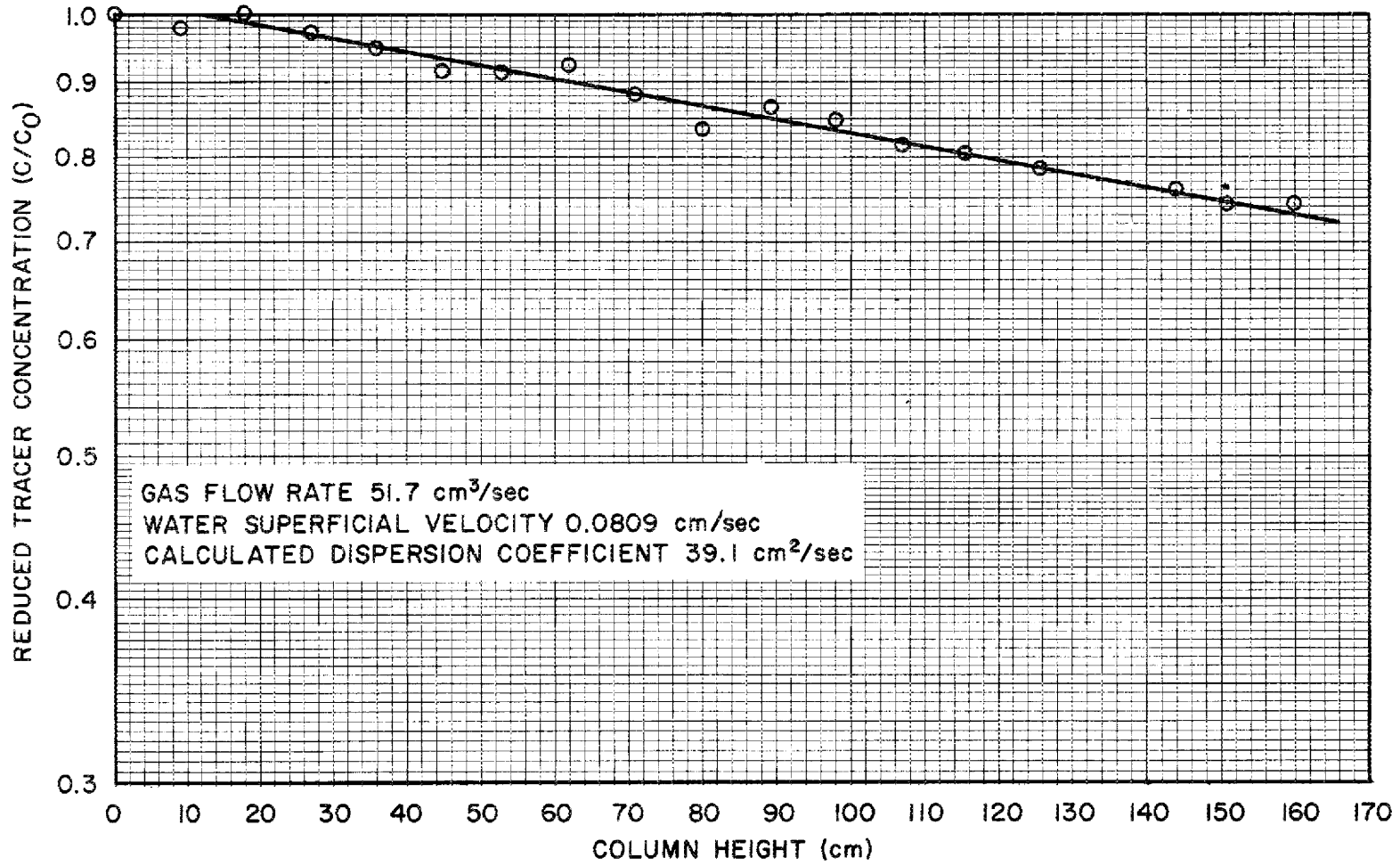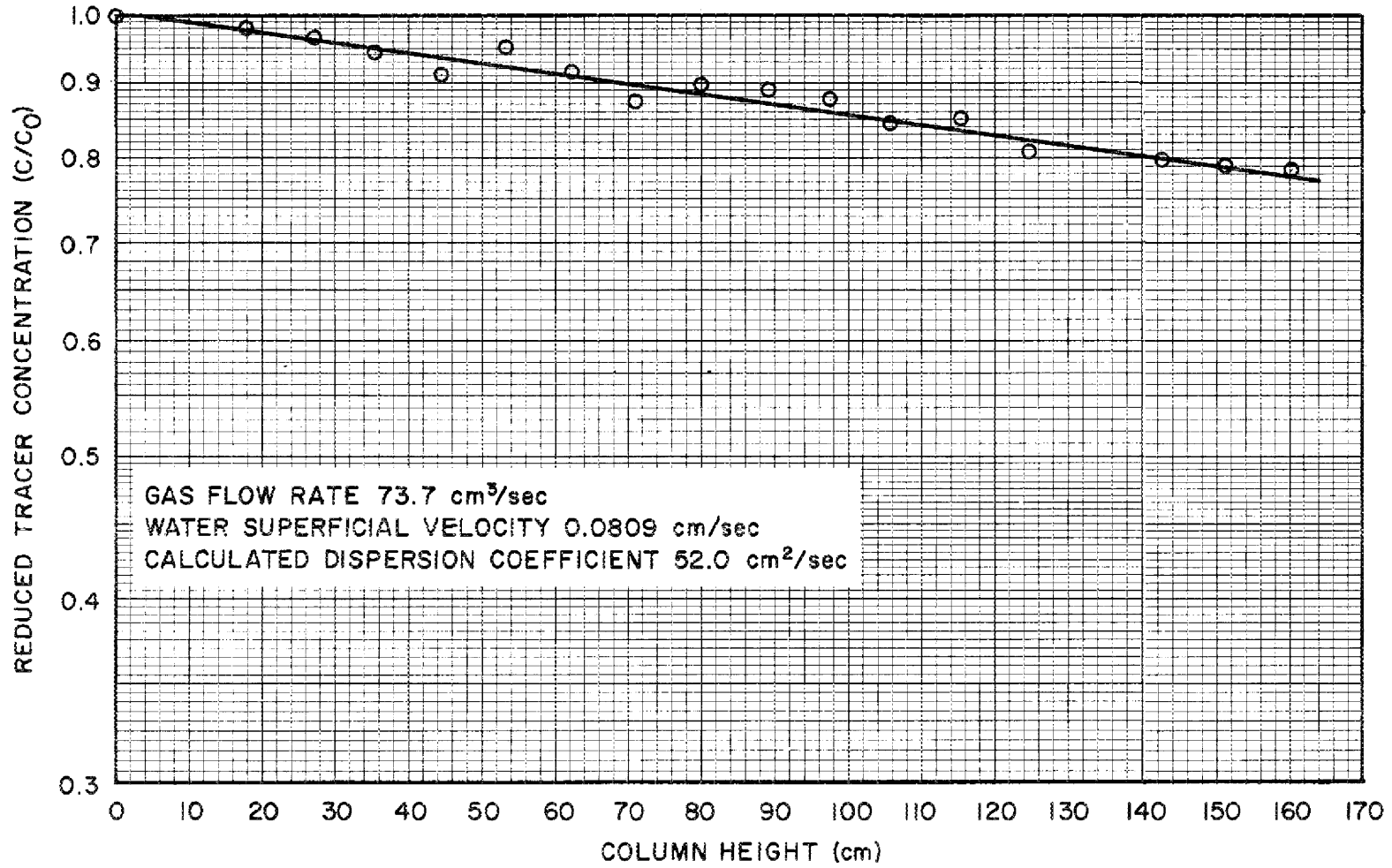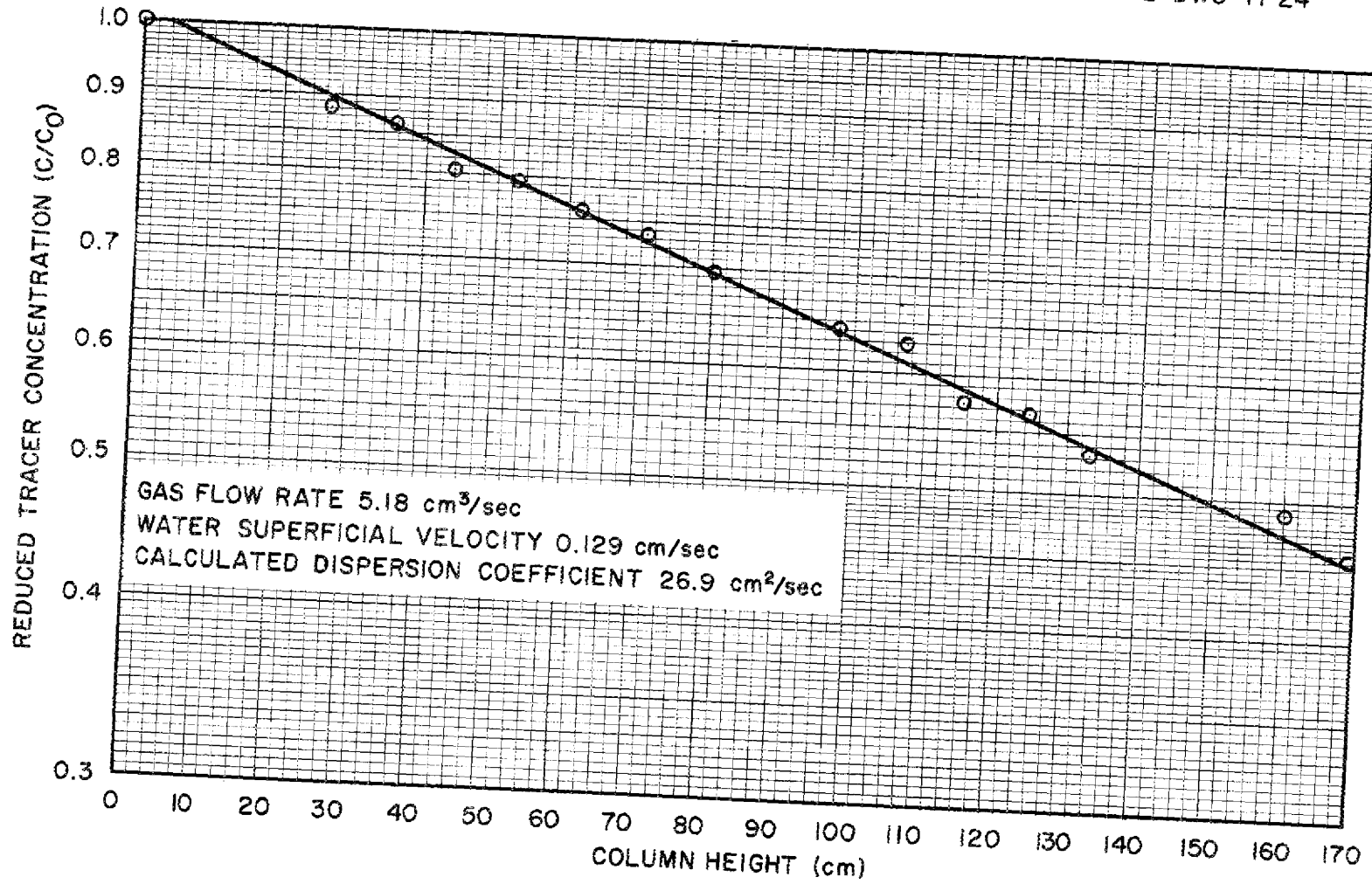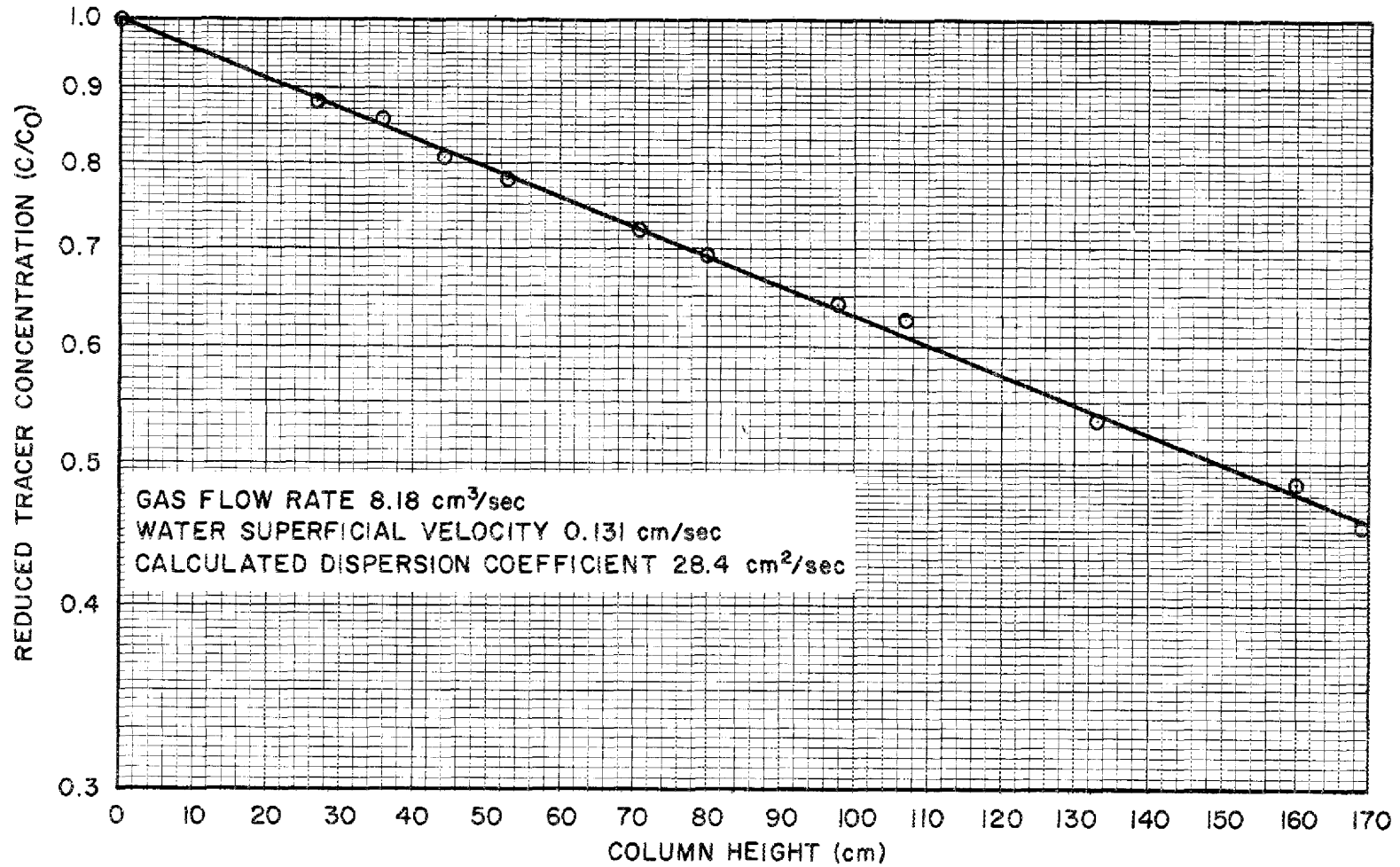Fig. 25. Variation of Reduced Tracer Concentration with Column Height for Run 4.

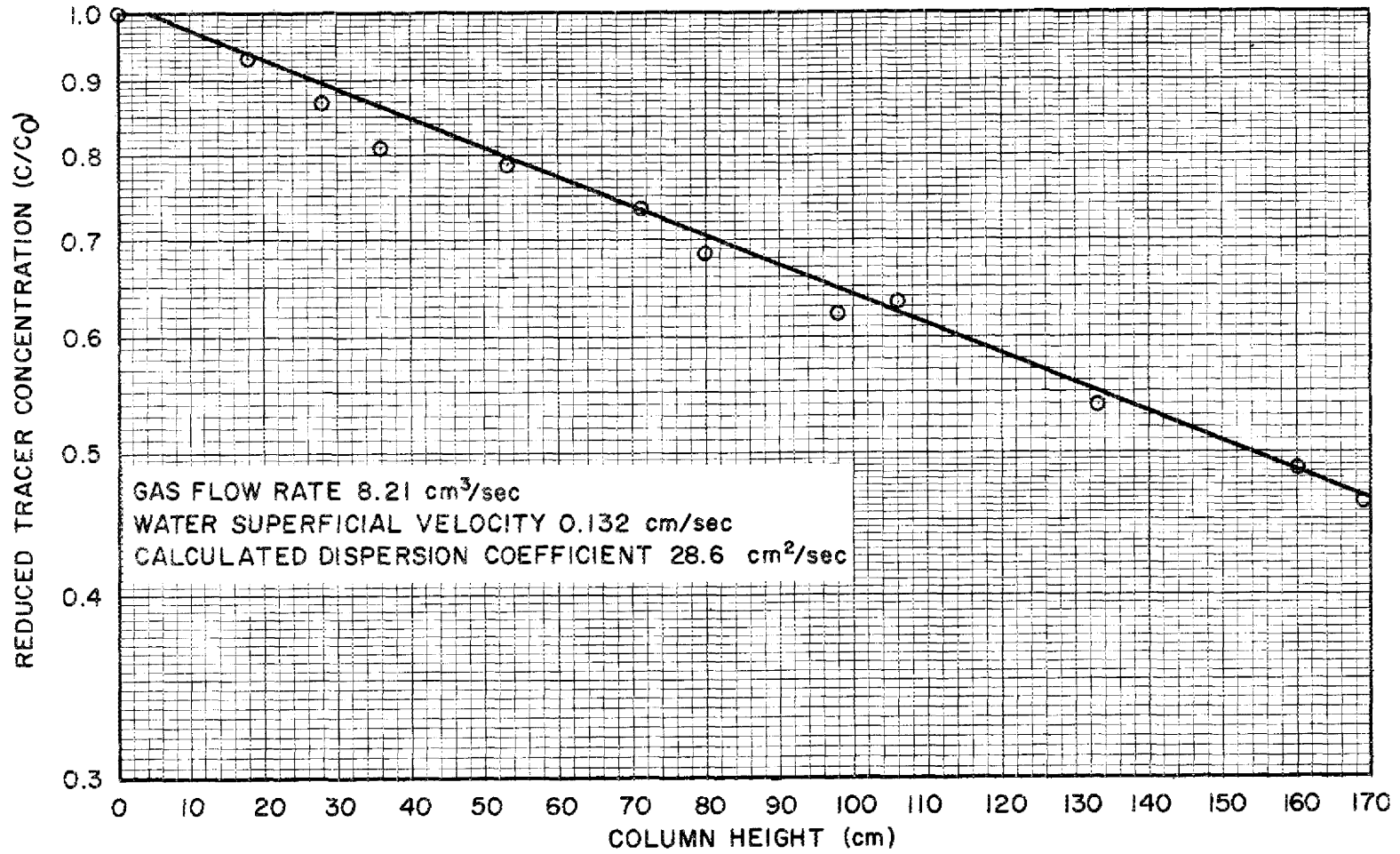Fig. 26. Variation of Reduced Tracer Concentration with Column
Height for Run 5.

Fig. 27. Variation of Reduced Tracer Concentration with Column Height for Run 6.

Fig. 28. Variation of Reduced Tracer Concentration with Column
Height for Run 7.

Fig. 29. Variation of Reduced Tracer Concentration with Column
Height for Run 8.

Fig. 30. Variation of Reduced Tracer Concentration with Column
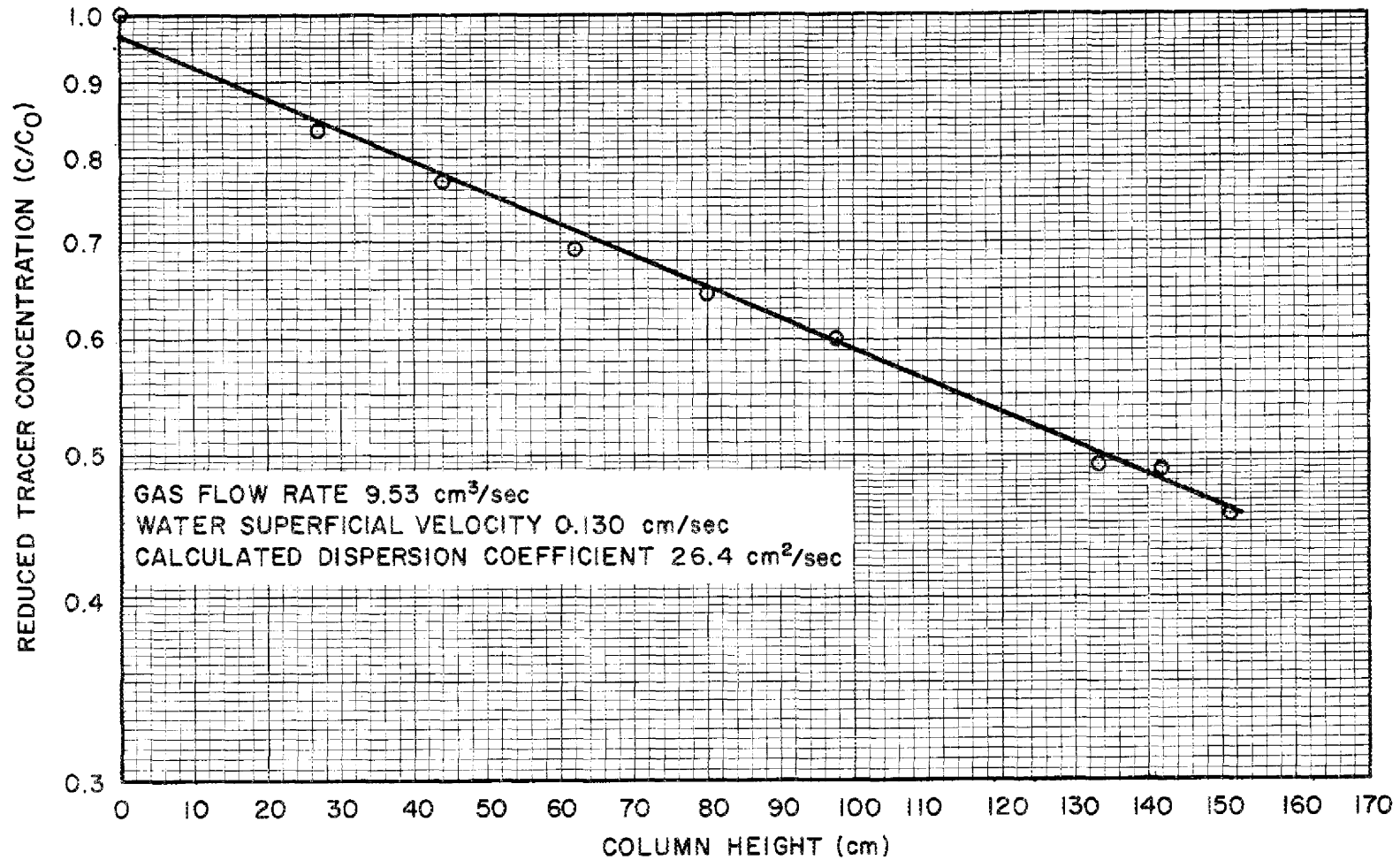Height for Run 9.

Fig. 31. Variation of Reduced Tracer Concentration with Column
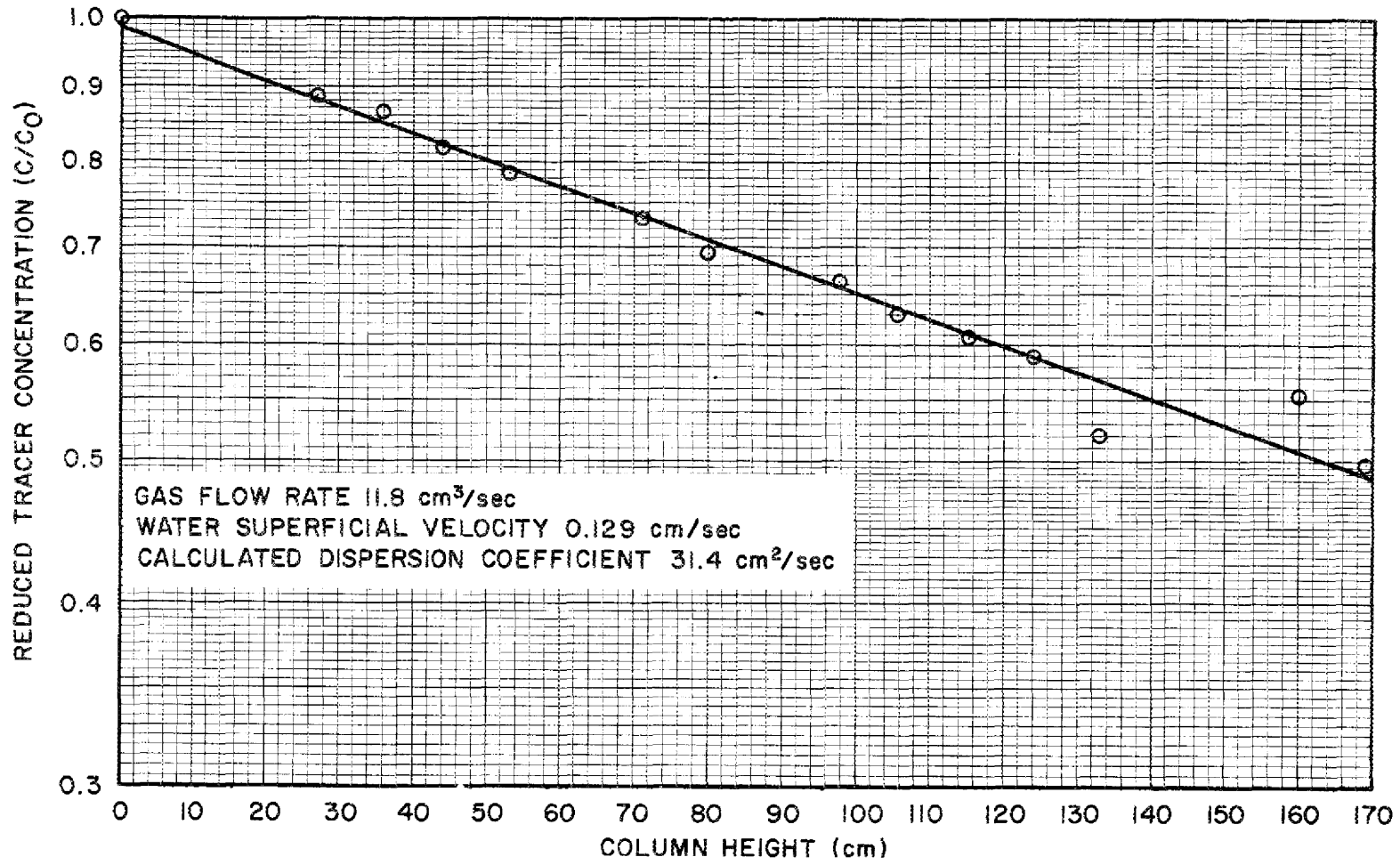Height for Run 10.

Fig. 32. Variation of Reduced Tracer Concentration with Column Height for Run 11.
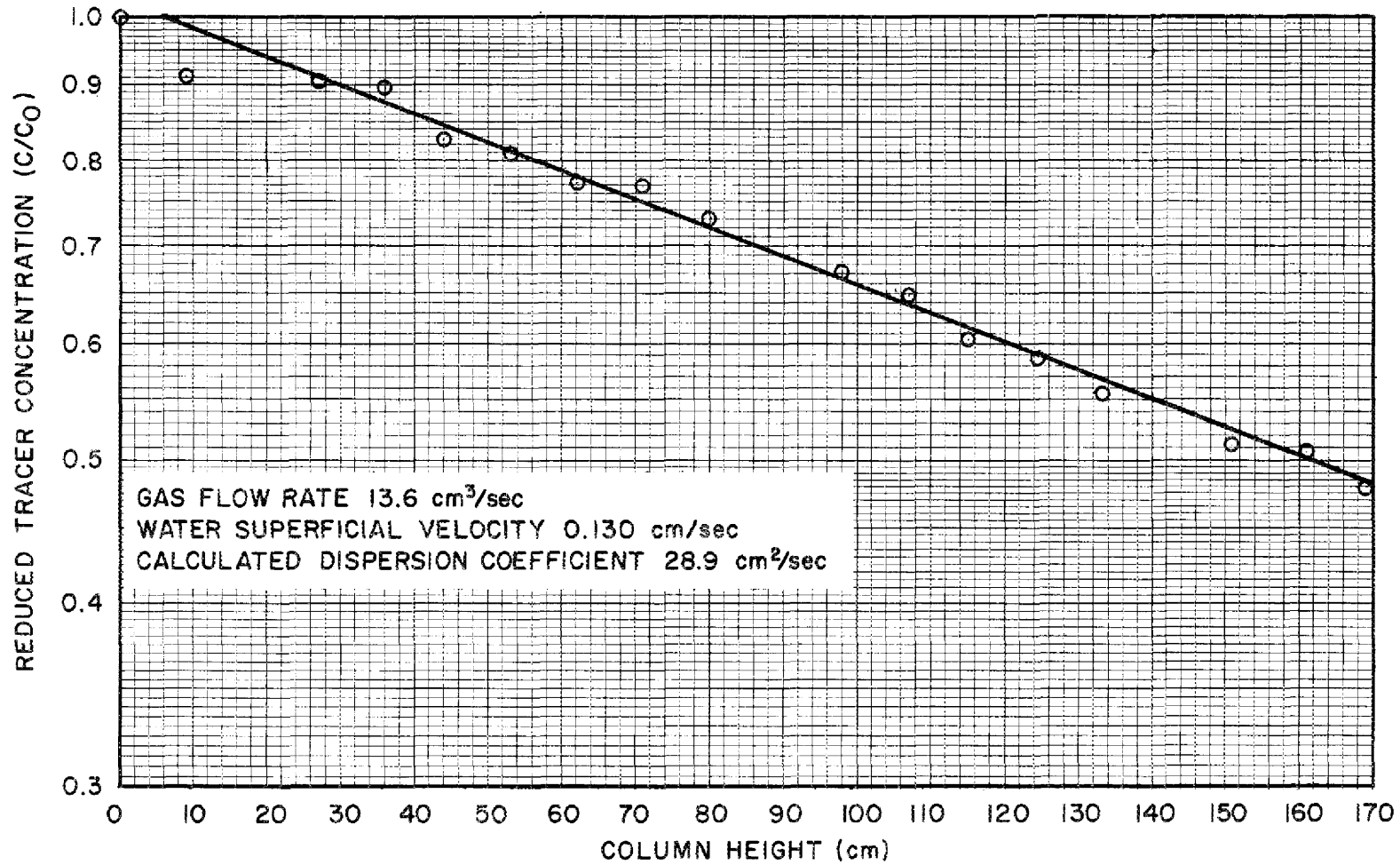
Fig. 33. Variation of Reduced Tracer Concentration with Column
Height for Run 12.

Fig. 34. Variation of Reduced Tracer Concentration with Column
Height for Run 13.

Fig. 35. Variation of Reduced Tracer Concentration with Column Height for Run 14.
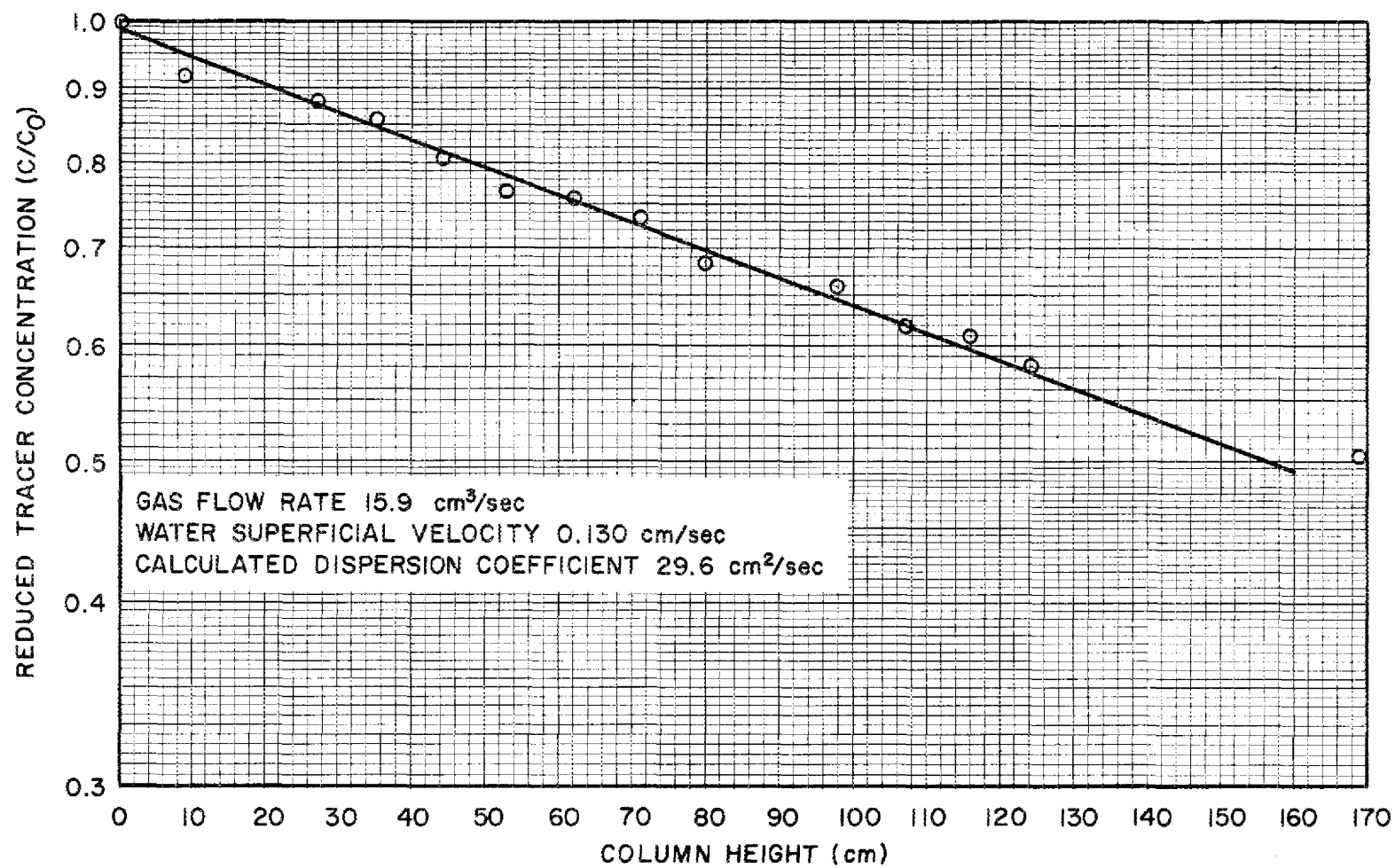
Fig. 36. Variation of Reduced Tracer Concentration with Column
Height for Run 15.

Fig. 37. Variation of Reduced Tracer Concentration with Column
Height for Run 16.

Fig. 38. Variation of Reduced Tracer Concentration with Column
Height for Run 17.

Fig. 39. Variation of Reduced Tracer Concentration with Column
Height for Run 18.

Fig. 40. Variation of Reduced Tracer Concentration with Column Height for Run 19.

Fig. 41. Variation of Reduced Tracer Concentration with Column Height for Run 20.

Fig. 42. Variation of Reduced Tracer Concentration with Column
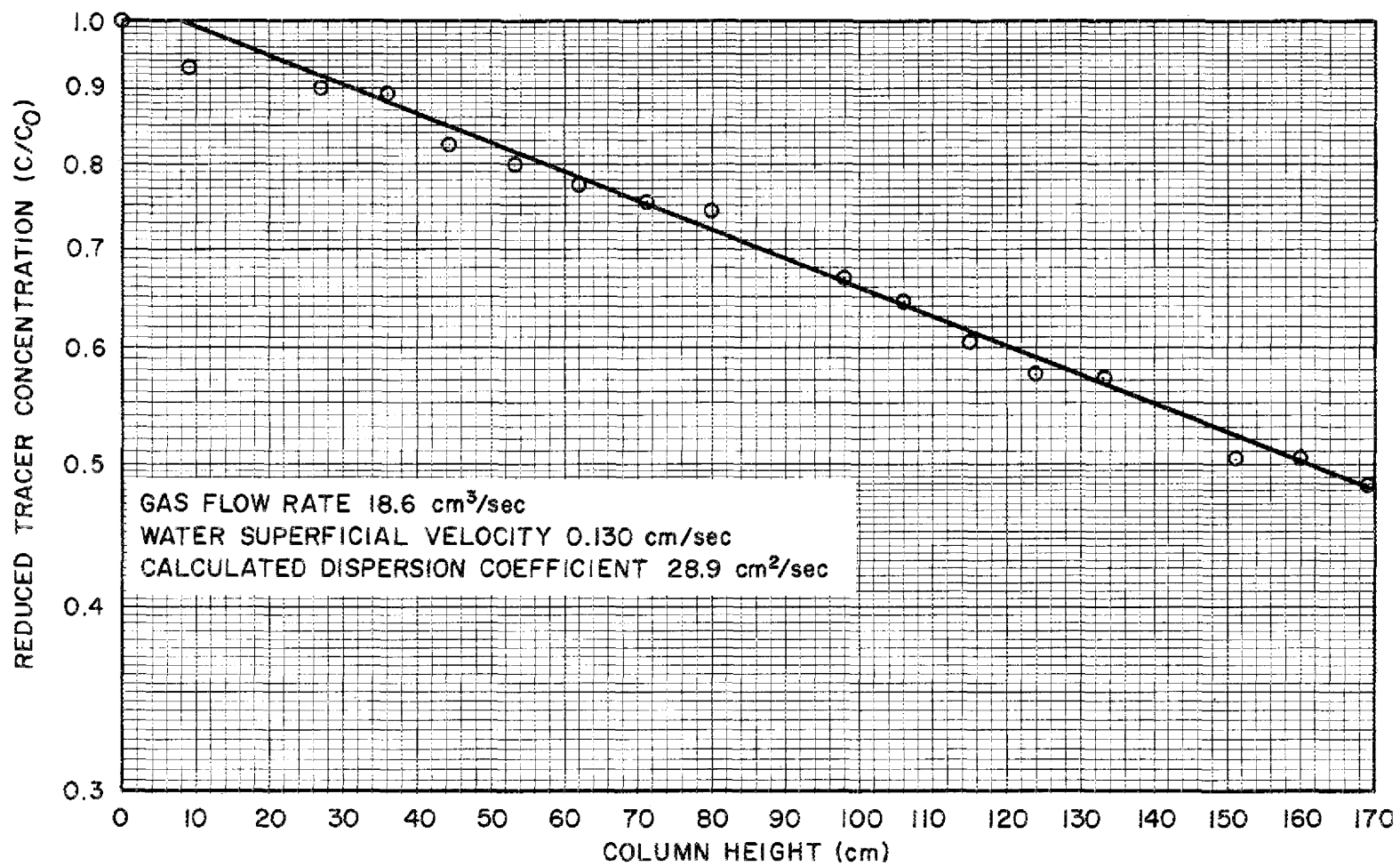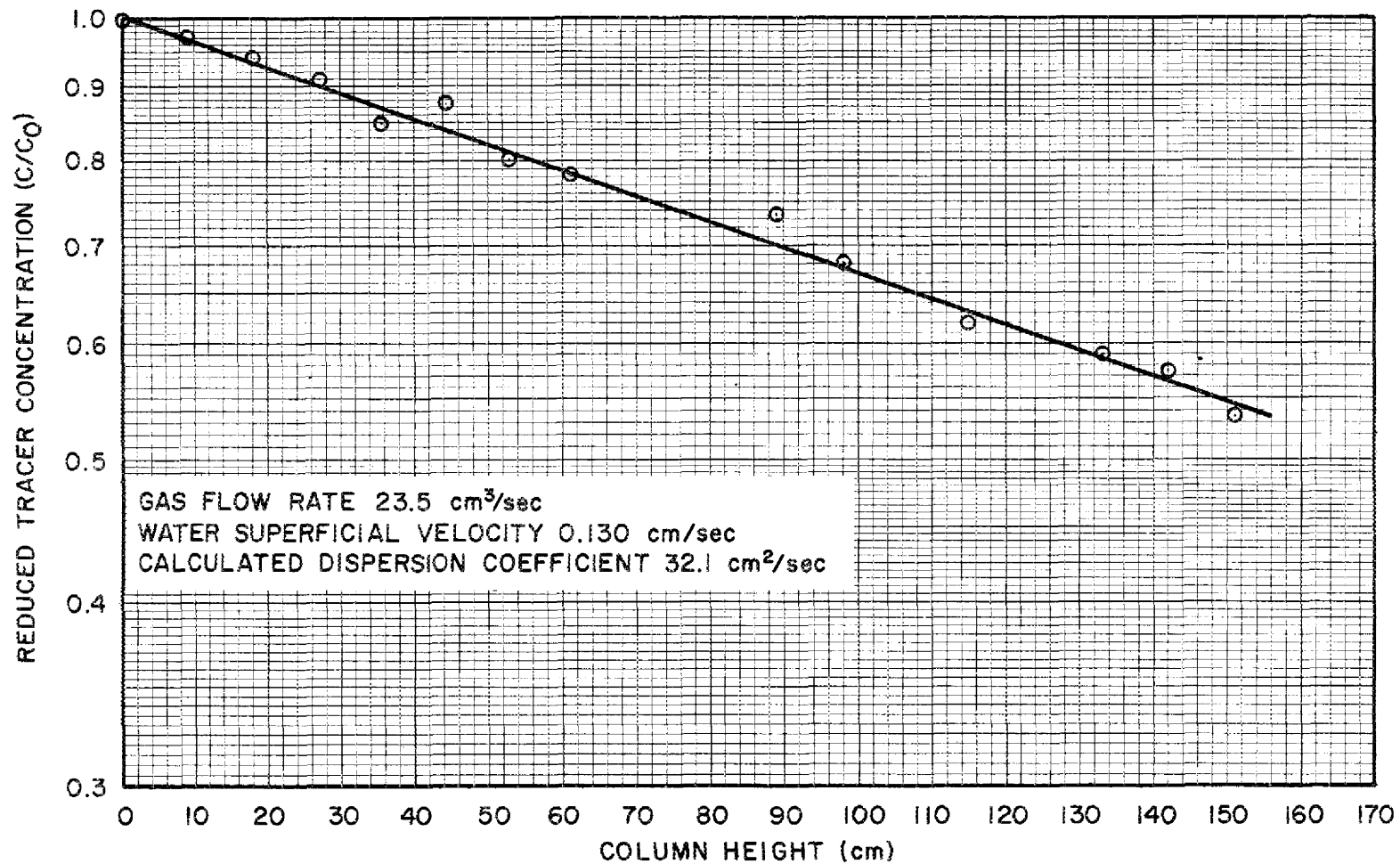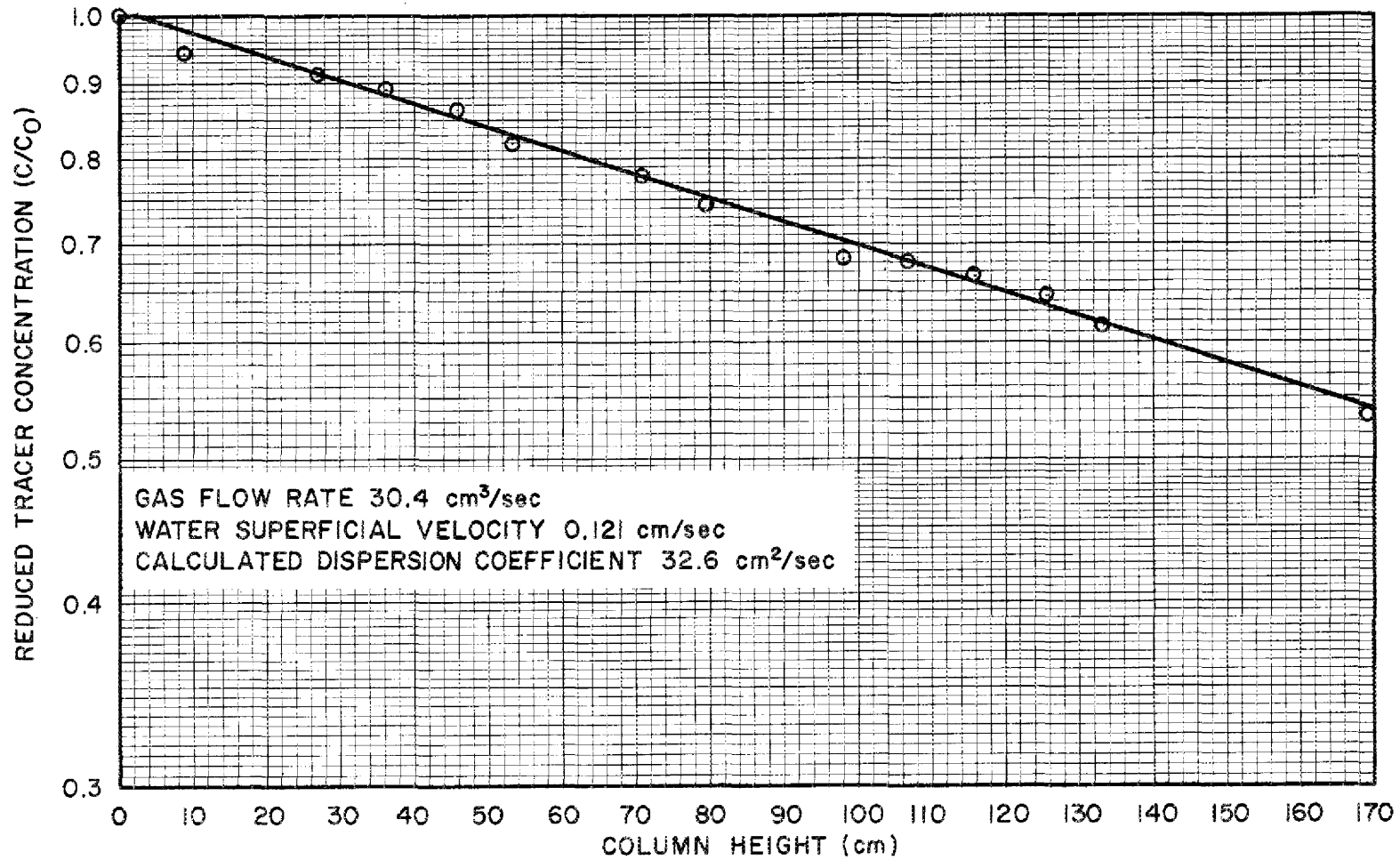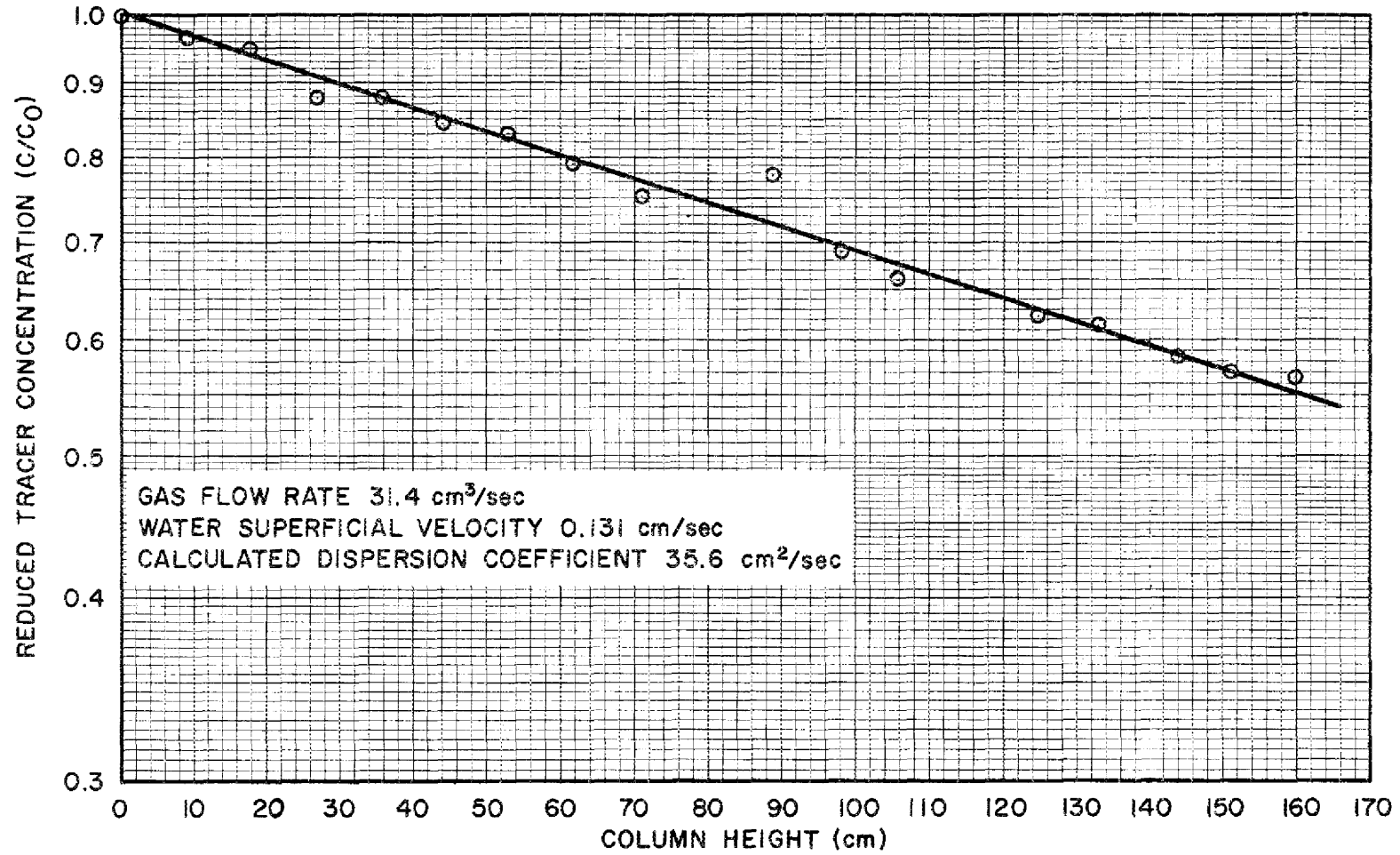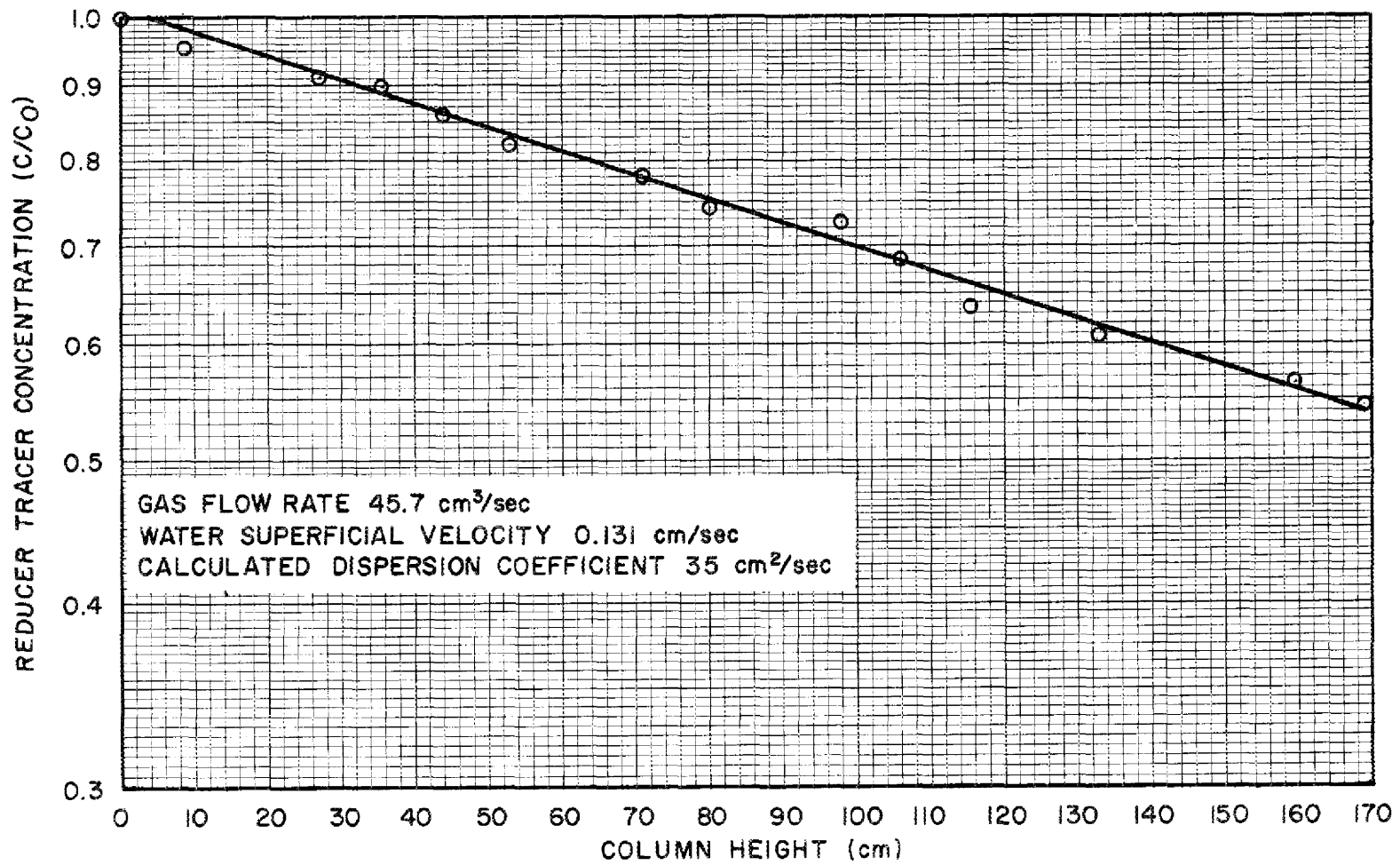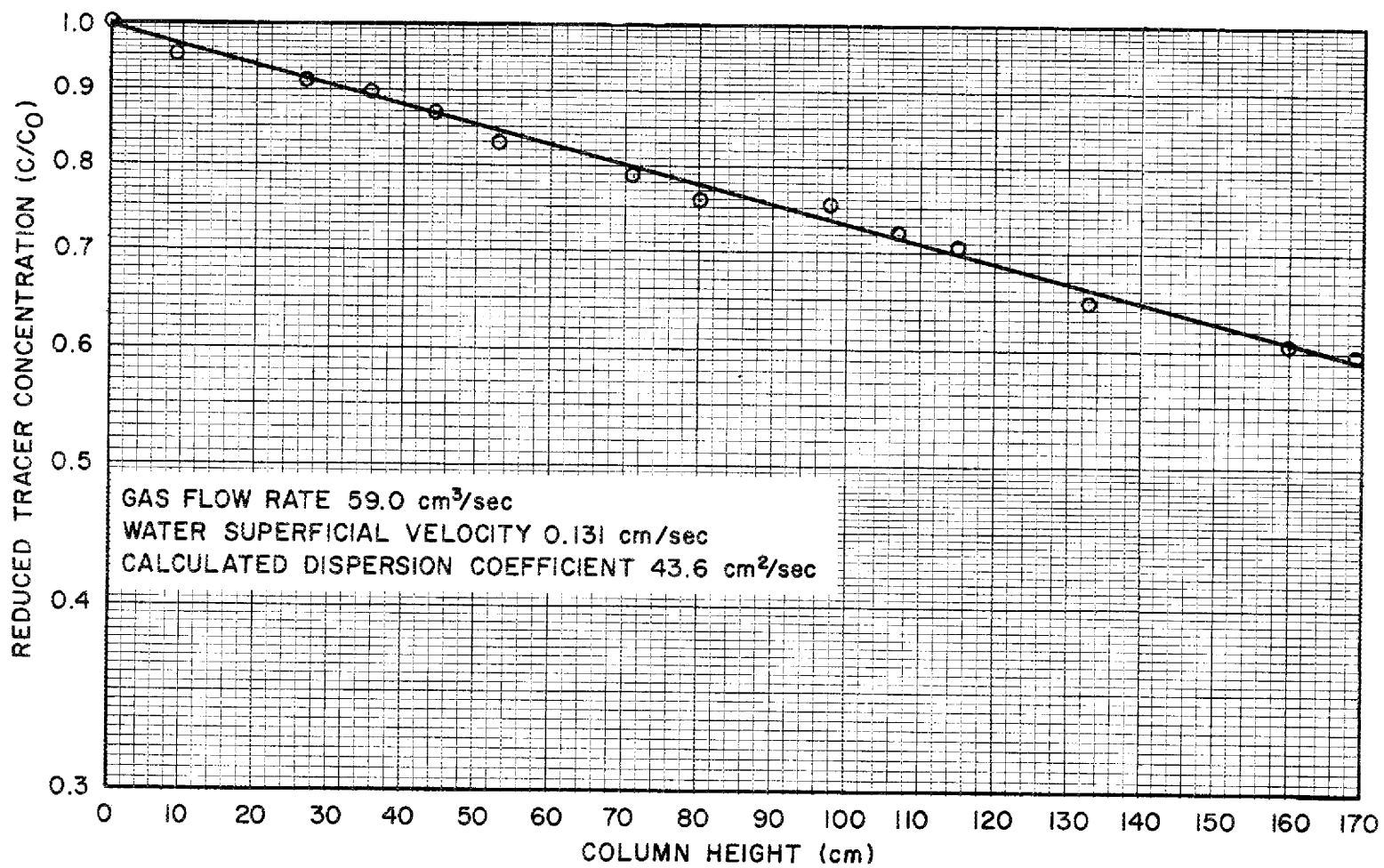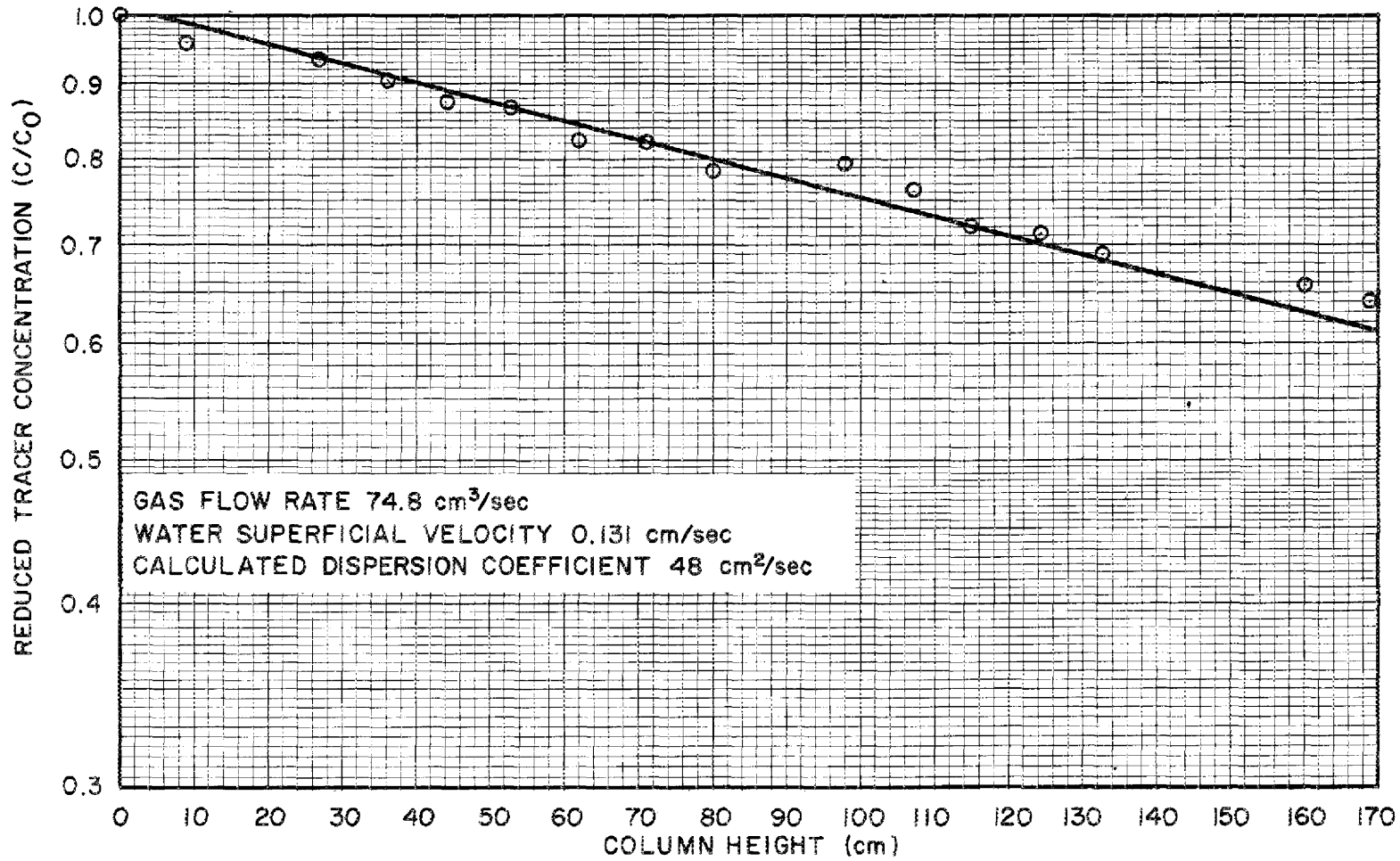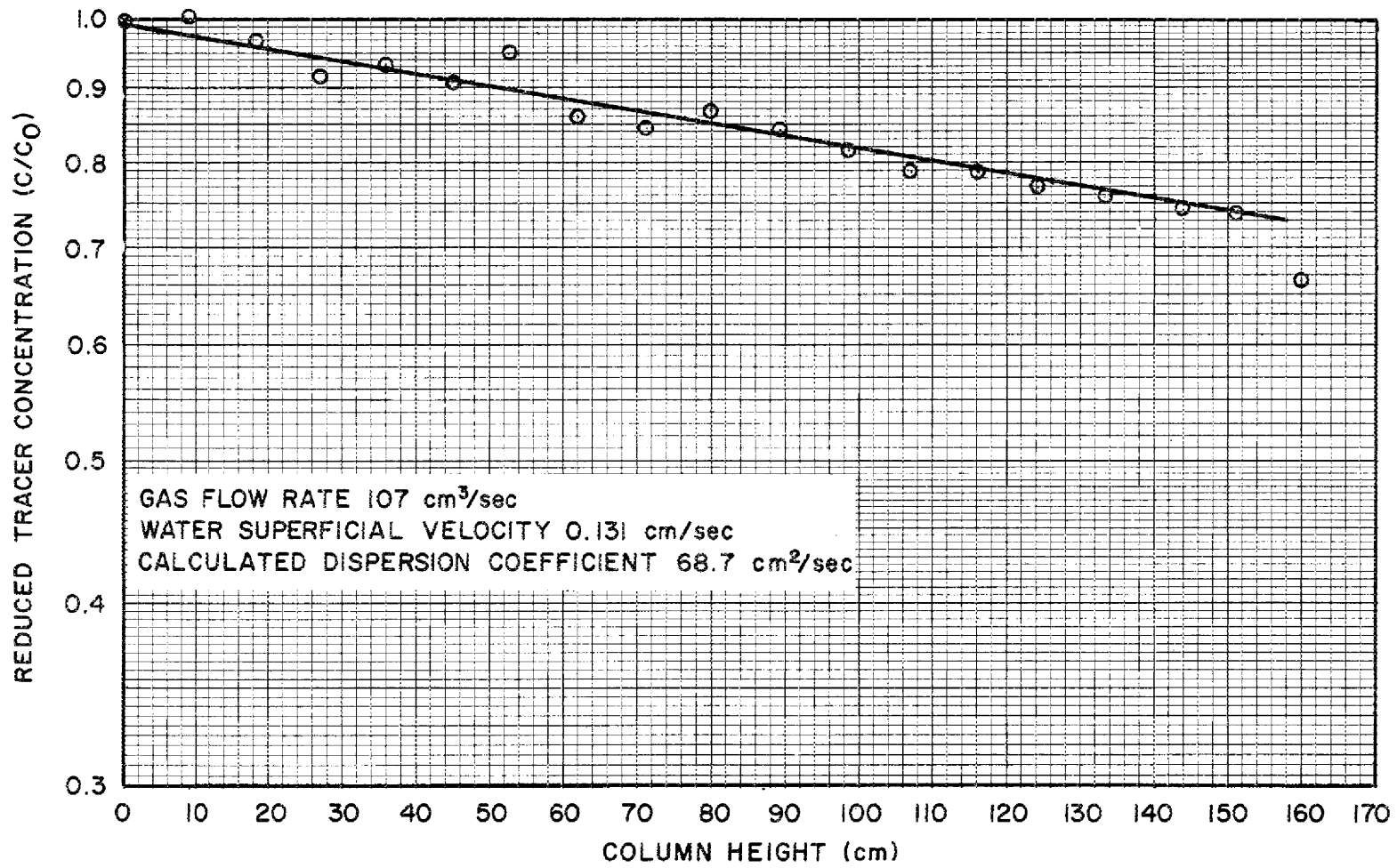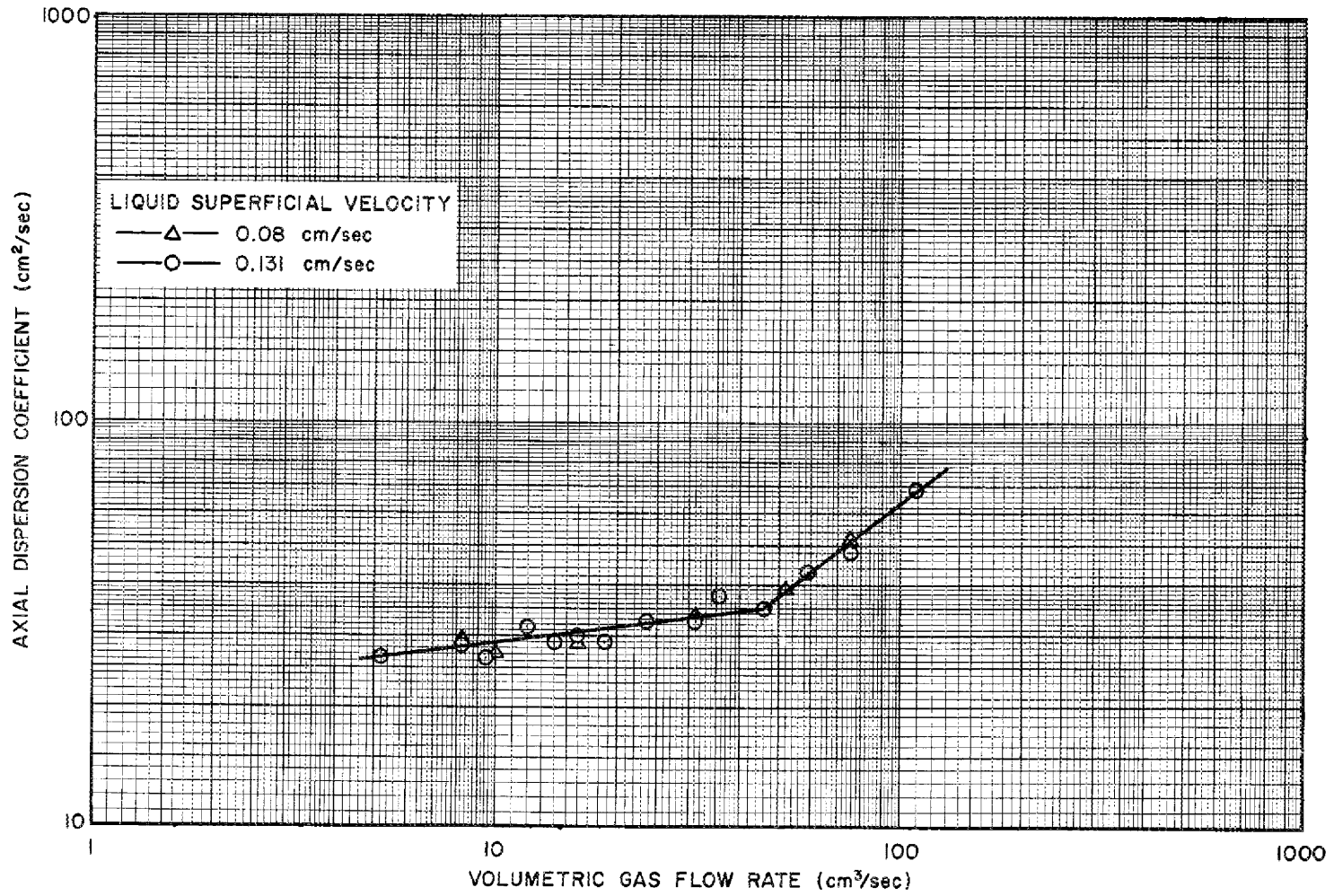Height for Run 21.

Fig. 43. Variation of Axial Dispersion Coefficient with Gas Flow
Rate in a 2-in.-diam Open Bubble Column.

6.6 Discussion of Results

6.6.1 Effects of Gas and Liquid Flow Rates on Axial Dispersion Coefficient

The axial dispersion coefficient was not influenced by the superficial velocity of the liquid at the flow rates used (0.131 and 0.080 cm/sec) (see Fig. 43). The results indicate that the mixing regime in the column was the same for the two liquid velocities and that the water velocities were not high enough to affect the bubble formation or to attenuate the rate of rise of the bubbles.

The effect of the gas flow rate on the axial dispersion coefficient is also shown in Fig. 43. Two distinct operating regions, which are distinguished by a sharp change in the dependence of dispersion coefficient on gas flow rate at a flow rate of 44 cm^3/sec, are observed in the figure. Visual observations and photographs indicate a difference in bubble behavior in these two operating regions. At the lower gas rates, the bubbles rise independently of each other as seen in Fig. 44, which shows the bubble distribution at the bottom photographic block at a gas flow rate of 16.0 cm^3/sec. This type of flow is denoted as "bubbly flow." Figure 45 shows the bubble distribution at a gas flow rate of 58 cm^3/sec: a range of bubble sizes is observed. The larger bubbles ascend more rapidly than the smaller ones, and a considerable amount of coalescence occurs. The coalesced bubbles grow in size until their diameter equals that of the column, and the length of the resulting bubbles increases as the gas flow rate is increased. This type of flow is denoted as "slug flow." In slug flow, a circulatory flow of liquid develops around each bubble and results in increased mixing as a result of the large bubble sizes. From visual observations, bubble coalescence appears to begin at a gas flow rate of about 44 cm^3/sec.

ORNL DWG 71-50

Fig. 44. Air Bubble Distribution During Countercurrent Flow of Air and Water in a 2-in.-diam Open Bubble Column. Gas flow rate, 16 cm^3/sec; water superficial velocity, 0.130 cm/sec.

ORNL DWG 71-51
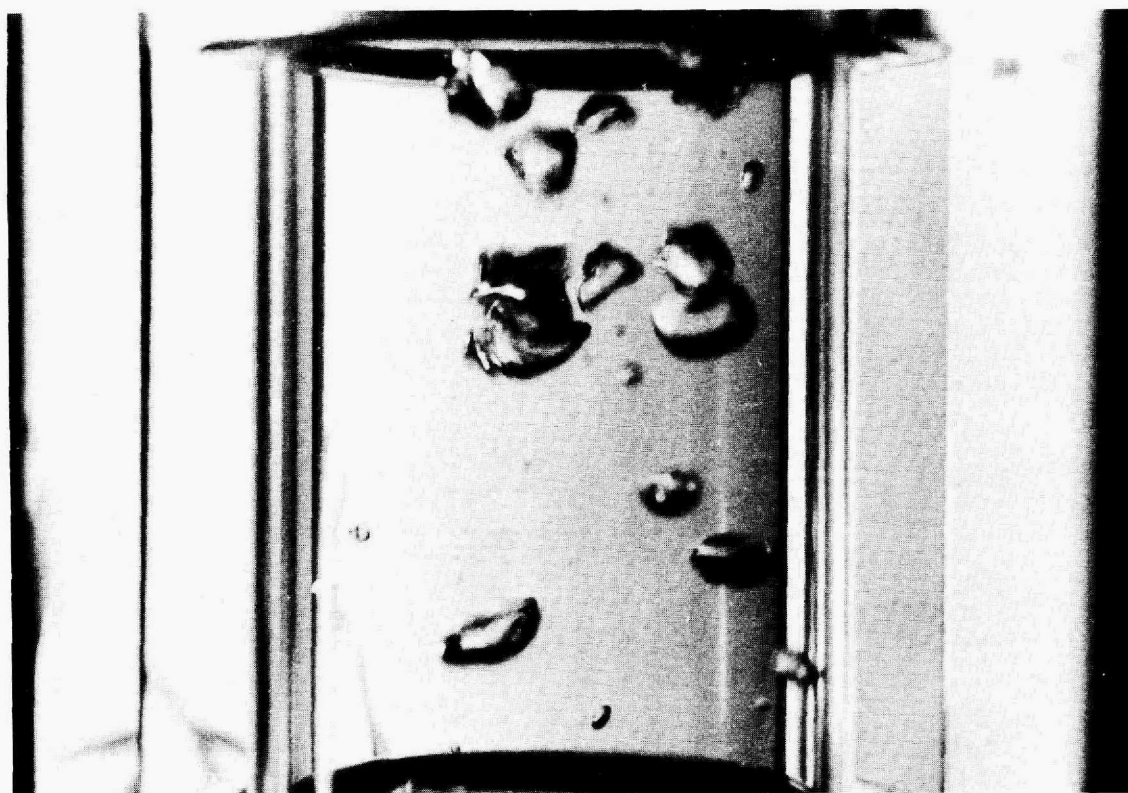

Fig. 45. Air Bubble Distribution During Countercurrent Flow of Air and Water in a 2-in.-diam Open Bubble Column. Gas flow rate, 58 cm^3/sec; water superficial velocity, 0.130 cm/sec.

6.6.2 Comparison of Measured Dispersion Coefficients with Literature Values

The dispersion coefficients that we measured in this work are higher than coefficients reported in the literature (see Fig. 46). Argo and Cova[11] and Siemes and Weiss[12] used multiple-orifice gas dispersers, which may account for the difference in the results. However, the transition from bubbly flow to slug flow reported by Siemes and Weiss appears to coincide with that observed in our study.

6.7 Verification of Assumptions in Mathematical Model

Several assumptions were made in deriving the mathematical model used for correlating the data; verification of the more important assumptions is discussed below.

6.7.1 Invariance of Dispersion Coefficient Along the Length of the Column

The assumption of invariance of dispersion coefficient along the length of the column is verified by the fact that straight lines are produced when the logarithm of the reduced tracer concentration is plotted vs column height (see Figs. 22-42).

6.7.2 Effect of Photocell Pumping Rate

Dispersion in the column could be affected by the withdrawal of solution from, and return of solution to, the column. The magnitude of this effect was checked by comparing axial dispersion coefficients measured at two pumping rates ($0.18 \text{ cm}^3/\text{sec}$ and $0.12 \text{ cm}^3/\text{sec}$) but a fixed superficial liquid velocity (0.13 cm/sec) and gas flow rate ($8.2 \text{ cm}^3/\text{sec}$). The measured dispersion coefficients were $28.6 \text{ cm}^2/\text{sec}$ and $28.4 \text{ cm}^2/\text{sec}$ for pumping rates of $0.12 \text{ cm}^3/\text{sec}$ and $0.18 \text{ cm}^3/\text{sec}$, respectively; the deviation of these coefficients from their average was less than 1%.
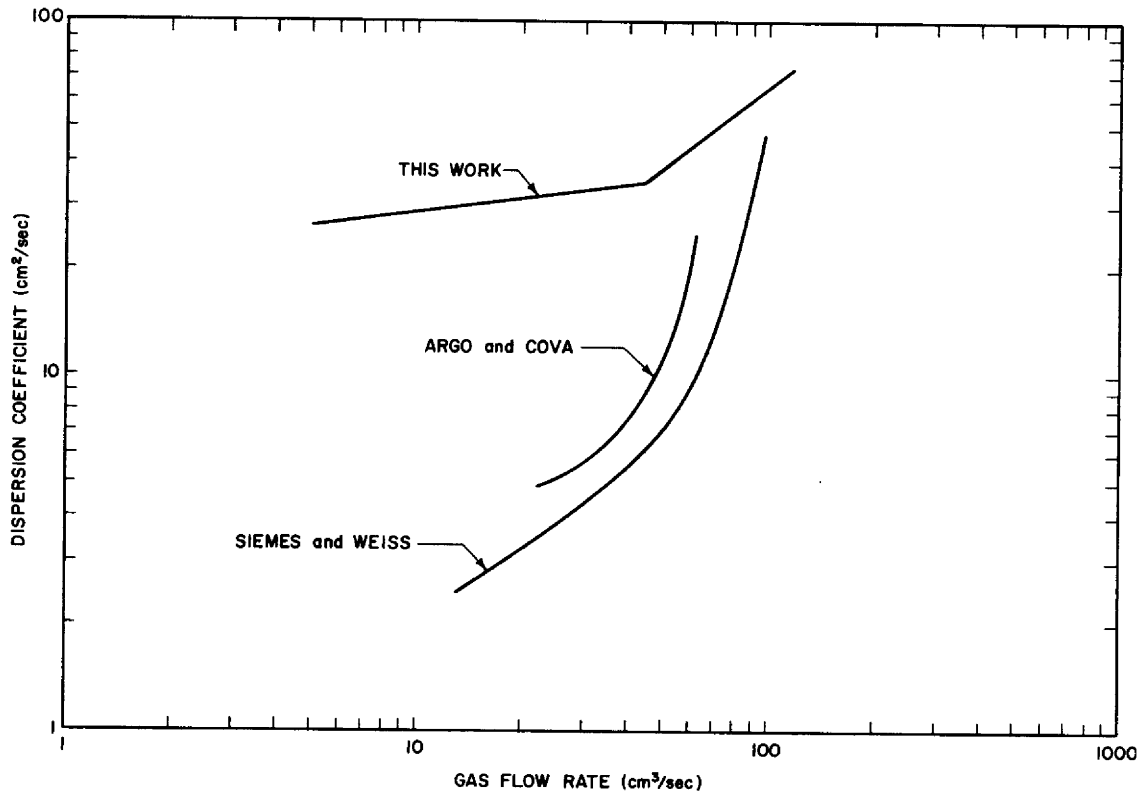
ORNL DWG 71-52

Fig. 46. Comparison of Measured Dispersion Coefficients with Literature Values.

6.7.3 Effect of Tracer Feed Rate

The effect of tracer feed rate was determined by comparing dispersion coefficients measured at two different tracer feed rates but at the same liquid and gas flow rates. This effect must be considered since the lower tracer feed rate of 0.081 cm^3/sec was used at the superficial liquid velocity of 0.08 cm/sec in order to avoid exceeding the tracer concentration limit at the bottom of the column. The dispersion coefficients were 28.4 cm^2/sec and 26.7 cm^2/sec for tracer feed rates of 0.407 cm^3/sec and 0.163 cm^3/sec, respectively; the deviation of each of these values from their average value was less than 4%.

6.7.4 Comparison of Tracer Concentration Profiles Measured Photometrically and Determined by Chemical Analysis

A comparison was made of the axial dispersion coefficients determined by the technique employed in these studies and the coefficients determined from a tracer concentration profile that was obtained by withdrawing solution at different points along the column and chemically analyzing the samples for copper. The results are shown in Fig. 47. The samples were withdrawn at a rate sufficiently low that the photocell readings did not change. The dispersion coefficient values were 23.1 cm^2/sec and 30.3 cm^2/sec for the photocell and the copper analysis data, respectively. The deviation of the value based on the photocell data from the value based on copper analysis was less than 8%.

7. ELECTROLYTIC CELL DEVELOPMENT: STATIC CELL EXPERIMENTS

J. R. Hightower, Jr.   M. S. Lin
L. E. McNeese

The proposed flowsheet for processing a molten-salt breeder reactor requires the use of electrolytic cells for reducing lithium and thorium fluorides at a bismuth cathode and for oxidizing materials from bismuth solutions at a bismuth anode. Experiments directed toward two problems
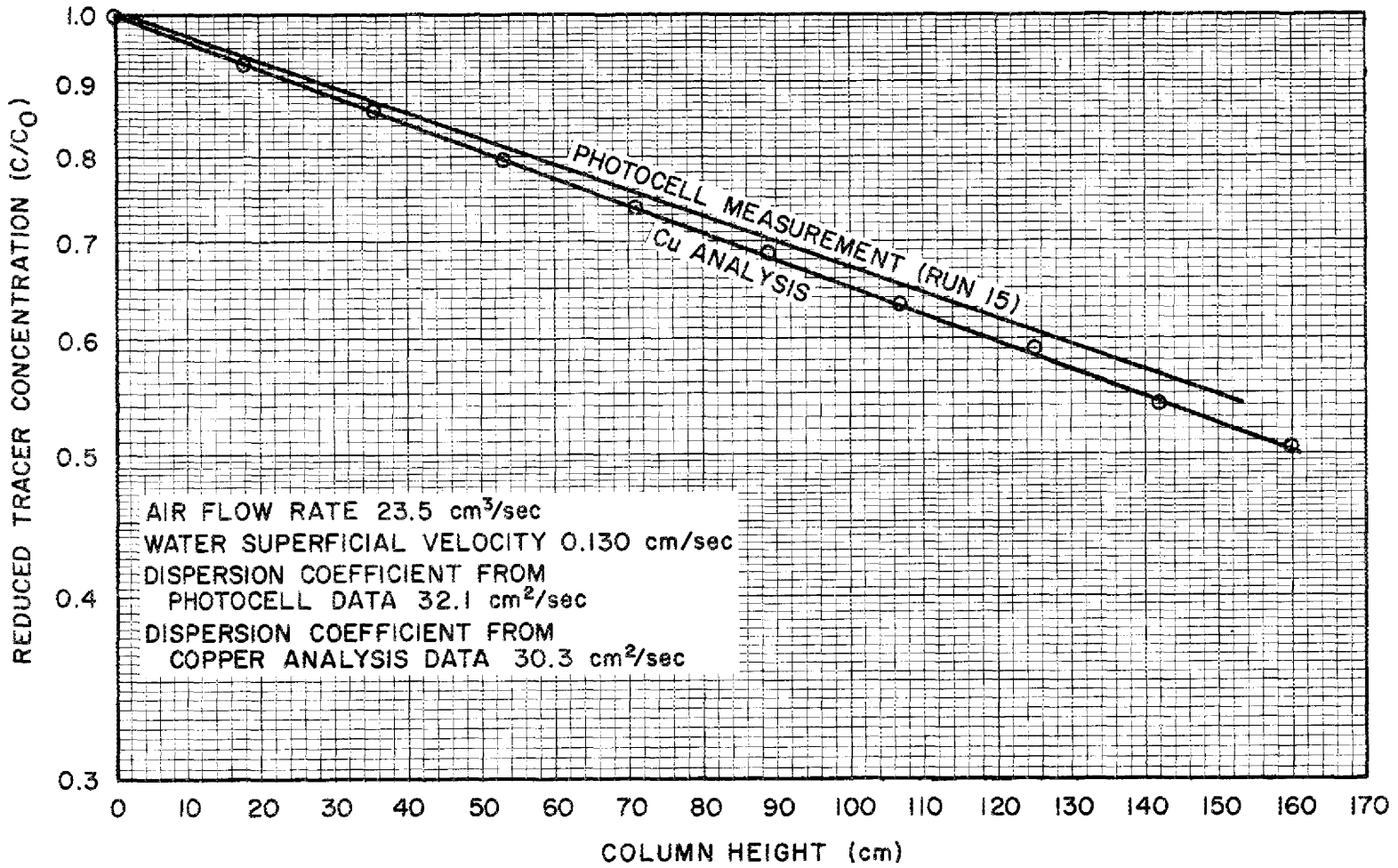
Fig. 47. Comparison of Tracer Concentration Profile Measured Photo-
metrically with That Measured by Analysis of Samples Withdrawn Along the
Column.

related to cell development were carried out in static cells. The objectives were: (1) determination of conditions under which a protective frozen salt film can be maintained on electrode dividers in the presence of high heat generation in the salt, and (2) identification of a black material which has formed in the salt during all static-cell experiments carried out to date. In one experiment, frozen salt films were formed around the top of a BeO electrode divider located in a region of high current density. In the second experiment, lead-acid batteries were used to provide a constant voltage in order to determine whether an ac component in the nominal dc power contributed to the formation of the black material in the salt.

7.1 Formation of Frozen Salt Films on a BeO Electrode Divider

Because BeO has several properties that would be useful in constructing an electrolytic cell, its use is being explored. An experiment utilizing a BeO electrode divider was carried out in a 4-in.-diam quartz cell, which has been described previously.[13] The anode for the experiment consisted of a 2-1/2-in.-diam by 1-1/4-in.-high cup made of BeO. The cup was clad with metal on the inner and outer surfaces and had provisions for forming a frozen film of salt around the upper rim of the cup. During the experiment, the BeO was used as the electrical insulator between the anode and cathode; it was not exposed to molten salt. The anode area was 15 cm^2 before a frozen salt layer was formed on the rim of the BeO cup.

The bismuth that was used in the experiment was treated with hydrogen in a separate mild-steel vessel at 700°C before being transferred to the cell vessel. The molten salt used in the experiment had the composition 66-34 mole % LiF-BeF$_2$.

Although the cell was operated for about 25 min, satisfactory operation was not obtained. Current densities of 2 to 5 A/cm^2 (based on initial anode area) were observed with an applied potential of about

2.1 V. The cell resistance was in the range 0.2 to 0.5 ohm. The operational difficulties that were encountered, and the methods that were used to correct them during the second experiment carried out in this type of cell, are discussed below.

1. The salt in the cell remained transparent only a short time after its introduction into the cell. There was some indication that the salt contained HF, which attacked the mild-steel components of the anode. In the second experiment, the salt was sparged with hydrogen in a separate vessel prior to being transferred into the cell.

2. The anode was too large for the 4-in.-OD quartz cell. The salt in the small annular space between the anode and the cell wall froze completely, causing the quartz vessel to break. This problem was solved in the second experiment by using a 6-in.-diam quartz cell vessel.

3. Bismuth droplets clinging to the inner and outer mild-steel cups caused shorting between the anode and the cathode. In the second experiment, the outer steel cup was removed.

4. The frozen salt layer at the coolant outlet was very thin. In the second experiment, an auxiliary coolant inlet was placed at the outlet of the cooling ring to provide frozen salt on the coolant outlet.

5. At the end of the run, the BeO cup was found to be cracked. The cracking probably occurred due to freezing of the bismuth and salt that were trapped between the steel cladding and the BeO cup. Holes were drilled in the inner cup for the next experiment to reduce the possibility of material becoming trapped between the BeO and the steel cup.

The cell used in the second experiment was similar to that used in the first experiment except for incorporation of the changes mentioned above. The cell used a 2-1/2-in.-OD BeO cup to contain bismuth for the anode (Fig. 48) and to electrically insulate the anode from the cathode. The cup was supported by a cooling ring, made of low-carbon steel, that was located just above the cup and was used to cover its rim with a protective frozen salt film. Coolant was introduced to the ring and removed from it through tubes that served as the anode electrical lead. The anode, which had an initial cross section of about 15 cm^2, was placed in the 6-in.-diam quartz vessel that contained the bismuth cathode pool. The assembled cell is shown in Fig. 49. The cell was charged with 16 kg of purified bismuth and 2.4 kg of salt (66-34 mole % $LiF-BeF_2-ThF_4$). The salt had been sparged with hydrogen at 600°C in a separate treatment vessel to remove residual dissolved HF. Two successful runs were made in which a frozen salt film was maintained on the portion of the BeO cup in contact with salt. The steps in the operating procedure were as follows.

1. The salt and bismuth temperatures were set between 465 and 470°C. (The liquidus temperature of 66-34 mole % $LiF-BeF_2$ is 458°C.)

2. With the cooling ring located about 1/4 in. above the normal cell operating position and completely in the salt phase, the nitrogen coolant flow was started (see first diagram in Fig. 50) at about 1 scfm. This flow of coolant caused a layer of frozen salt to form on the cooling ring and on the coolant inlet and outlet tubes.

3. When frozen salt had completely covered the cooling ring and inlet and outlet tubes, the BeO cup was lowered to a position about 1/8 to 1/4 in. below the operating level. This allowed frozen salt to form on the coolant inlet and outlet tubes and ensured that they would be completely insulated (see the second diagram in Fig. 50).
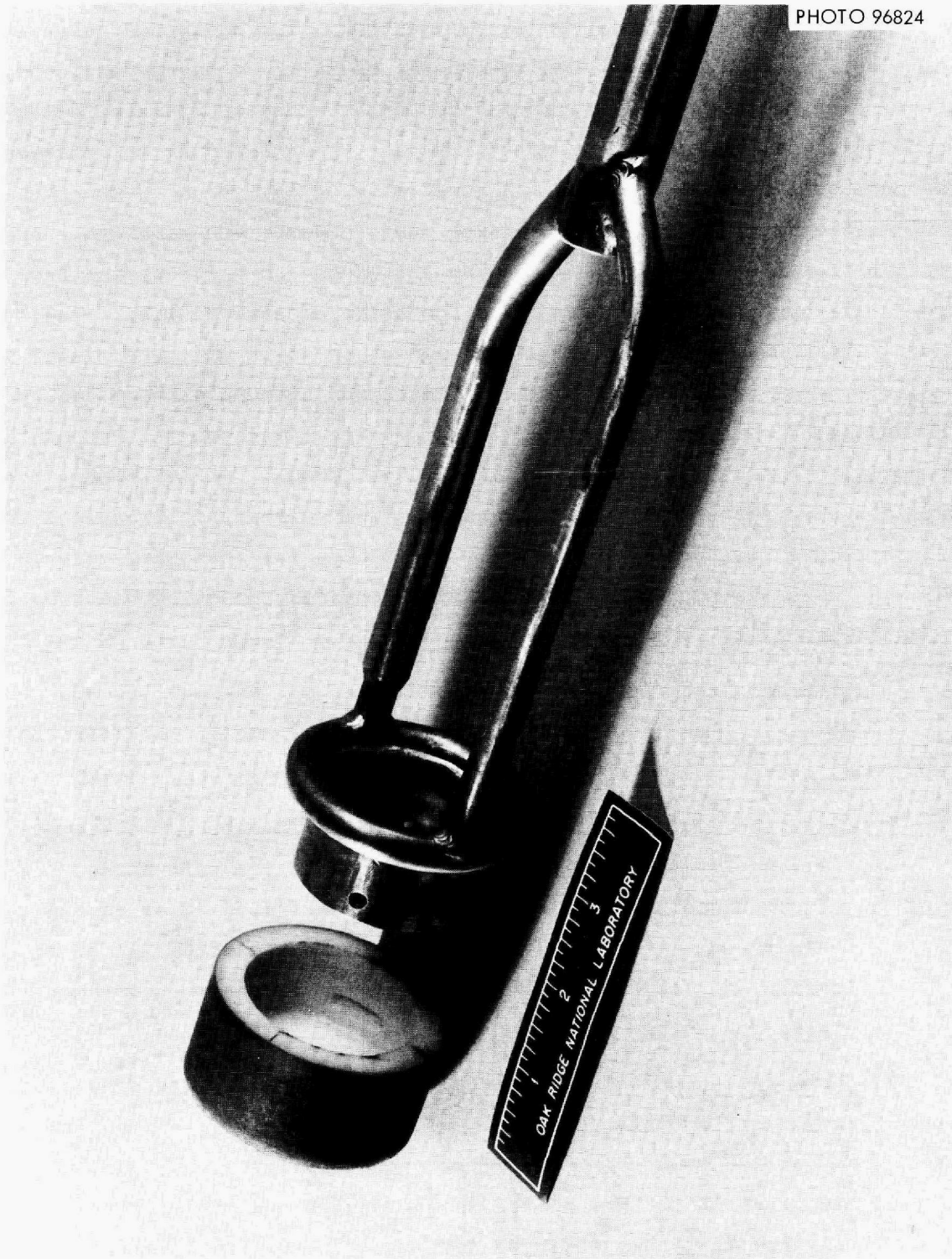
PHOTO 96824

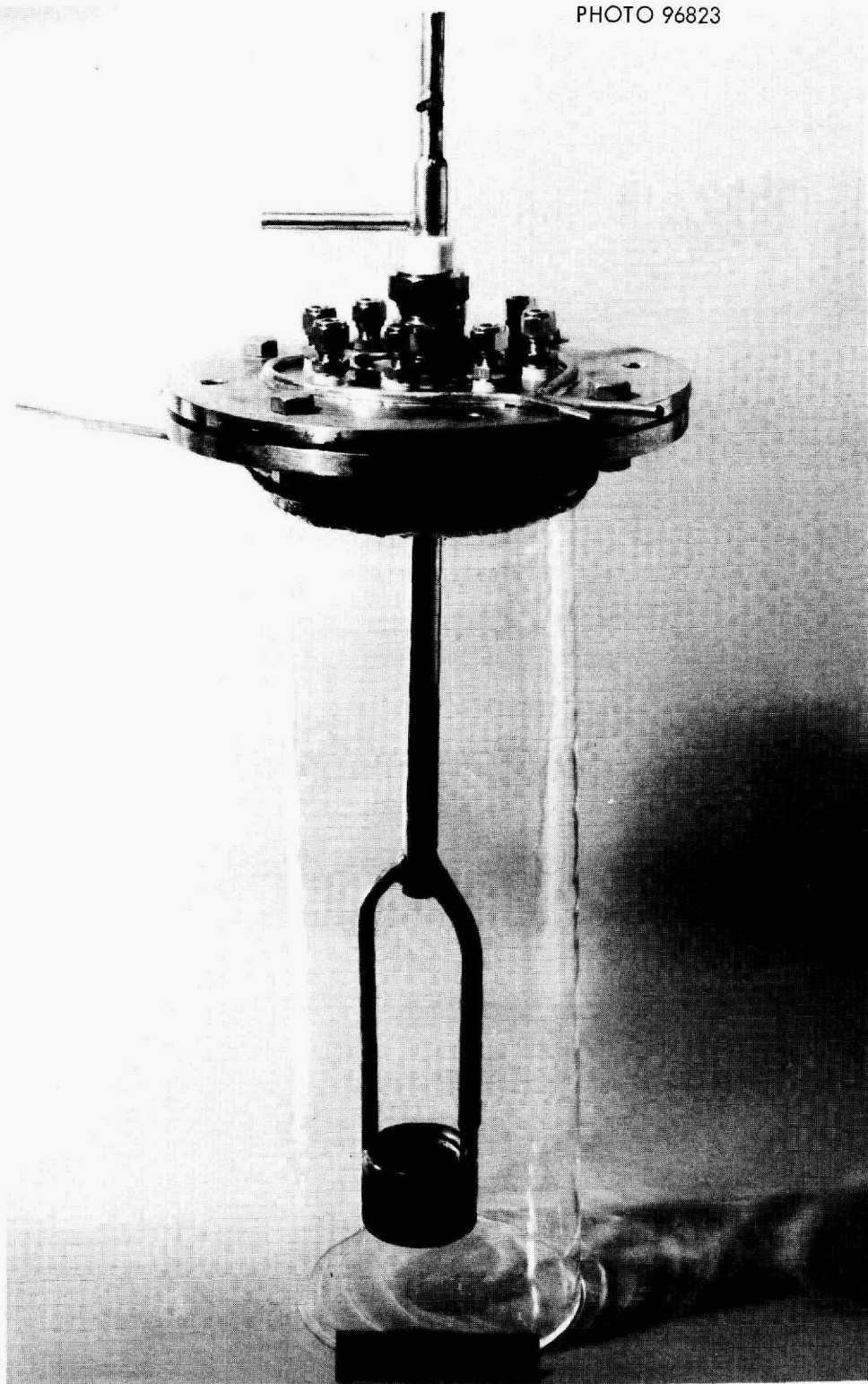Fig. 48. Unclad BeO Cup Used to Hold Anodic Bismuth Pool.

PHOTO 96823

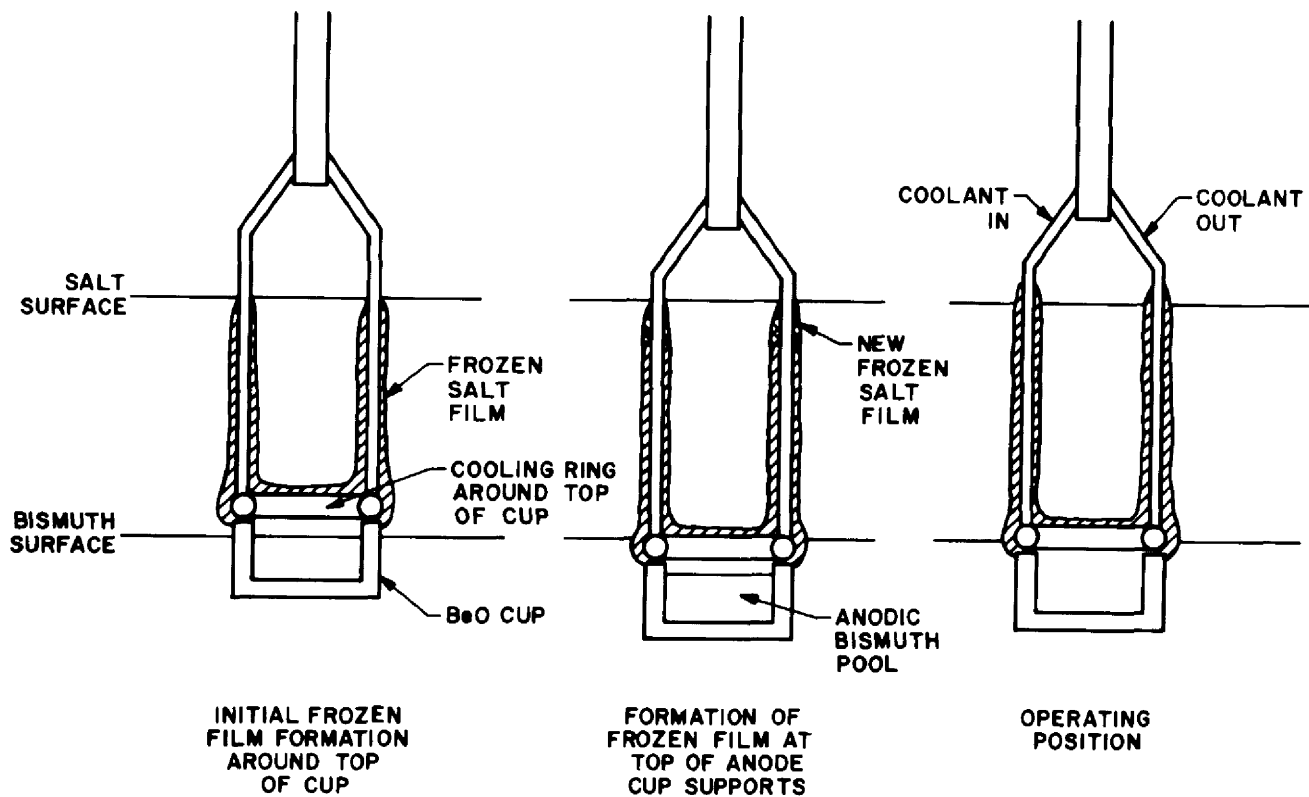Fig. 49. Assembled 6-in.-diam Quartz Cell Vessel Showing BeO Anode Cup Assembly.

Fig. 50. Steps in Startup of Cell with Anode Cup Protected with Frozen Salt Film.

4. During steps 2 and 3, salt was prevented from freezing com-
    pletely over the bismuth surface in the anode cup by moving
    a 3/8-in.-diam steel rod up and down at the center of the
    cup.

5. On completion of step 3, the anode cup was raised slightly
    to move any bare metal at the top of the coolant tubes out
    of the salt phase (see third diagram in Fig. 50). This
    final position allowed the bismuth in the cathode pool to
    contact the metal cooling ring in case the frozen salt on
    the cooling ring melted. This would cause a short circuit,
    an unmistakable indication of removal of the frozen film.

6. Voltage was then applied to the cell, and was increased step-
    wise until the desired value was reached. As the cell current
    increased, the rate of coolant flow was also increased.

In the first run, nitrogen was used as the coolant at flow rates
of 1 to 6 scfm. In the second run, water was atomized into the nitrogen
stream in order to increase the cooling capacity and to allow operation
for a longer period before exhaustion of the nitrogen supply. The second
run used ac power rather than dc power. In each run, the current was in-
creased stepwise, allowing steady-state conditions to be attained before
proceeding further. The maximum current densities reached in the first
and second runs were 1.9 A/cm^2 and 2.8 A/cm^2, respectively. Table 4
summarizes the data from these runs.

These experiments indicated that a layer of frozen salt can be main-
tained in the presence of high current densities if sufficient cooling is
provided. It is also necessary for the initial salt and bismuth temp-
eratures to be within about 10°C of the liquidus temperature of the salt.

Table 4. Summary of Data on Frozen Film Formation Obtained from Experiments
with the 6-in.-diam Quartz Static Cell

Run	Current Density (A/cm^2)	Duration (min)	Remarks
1	0-1.5	90	
	1.5	30	
	1.7	10	~6 scfm of nitrogen for cooling
	1.9	20	
	1.9-0	~5	Nitrogen supply depleted; current reduced without shorting the cell
2	0-1.5	~60	
	1.5-2.3	30	
	2.3	10	~1.3 scfm of nitrogen and >20 cc/min water as coolant
	2.5	23	
	2.6	7	
	2.8	9	Cell shorted; insufficient cooling

7.2 Experiment Using Lead-Acid Storage Batteries for Power Supply

The rectifier that is normally used to supply dc power for electrolysis experiments produces current with an appreciable ac ripple due to incomplete filtering. The ac component has been suspected to cause the formation of a dark-colored material, which has been repeatedly observed in the salt in all static-cell experiments to date, since it has been reported[14] that sols of electrode metals can be produced in molten salts by use of alternating current. Therefore, an experiment was carried out to determine whether the dark-colored material would be formed with direct current having no ac component. The cell used for this experiment was made from a 4-in.-diam quartz tube and contained a 3-in.-high quartz divider, which separated two hemicylindrical bismuth electrodes having a surface area of about 30 cm^2 each. The cell contained bismuth that had been purified by hydrogen sparging and molten salt (66-34 mole % LiF-BeF_2) that had been sparged with hydrogen to remove residual HF. The power supply consisted of five 6-V lead-acid storage batteries, each of which was rated at 200 A-hr.

The cell was operated initially at 500°C with a current of 3 A. Dark-colored material, accompanied by some gas evolution, could be seen rising from the anode surface; within 9 min, the salt became opaque. The salt cleared up after being allowed to stand overnight. In another run made at 600°C with a current of 2 A, the salt became opaque within 6 min as a result of material emanating from the anode. Again, the salt became clear after standing overnight.

Two additional runs were made: one with a cell temperature of 675°C and a current of 2.8 A, and the other at a cell temperature of 680°C with currents as high as 45 A. No dark material was formed during these runs. Another run was attempted at 500°C, but the presence of a large amount of precipitate in the salt (apparently produced during the previous runs) obscured visibility to such an extent that we could not tell whether any of the dark-colored material was formed.

The conclusions drawn from this experiment are: (1) ac ripple in the power supply is not responsible for production of the dark-colored material, and (2) the dark-colored material may not be formed at high temperatures. The black-colored material may be BiF_3 (an anode reaction product), which may react with quartz. At high temperatures, the dark-colored material is either completely soluble or it is not visible due to the high rate at which it reacts with quartz.

8. DESIGN AND INSTALLATION OF THE FLOW ELECTROLYTIC CELL FACILITY

J. R. Hightower, Jr.   L. E. McNeese
E. L. Nicholson   W. F. Schaffer, Jr.

A facility for continuously circulating molten salt and bismuth through electrolytic cells at temperatures up to 600°C is being installed in Bldg. 3541. The equipment associated with this facility will allow us to test a variety of cell designs under conditions similar to those expected in processing plants. The equipment consists of a 16-in.-diam vessel that will contain the cell to be tested, a mixer-settler tank in which the salt and bismuth streams from the cell will be equilibrated, gas-lift pumps and orifice--head pot flowmeters for circulating and metering the streams to the cell, and a vessel containing a graphite crucible for purifying the salt and bismuth. Also provided are a gas supply station for metering HF, hydrogen, argon, and nitrogen; a system for disposing of unreacted HF; a 750-A dc power supply; and instrumentation for recording pressures, temperatures, current, and voltage.

A detailed description of this equipment is given in the remainder of this section.

8.1 Flow Diagram

A flow diagram for the system is shown in Fig. 51. Bismuth and salt are circulated by gas-lift pumps at nominal flow rates of 0.5 and 0.25 gpm,
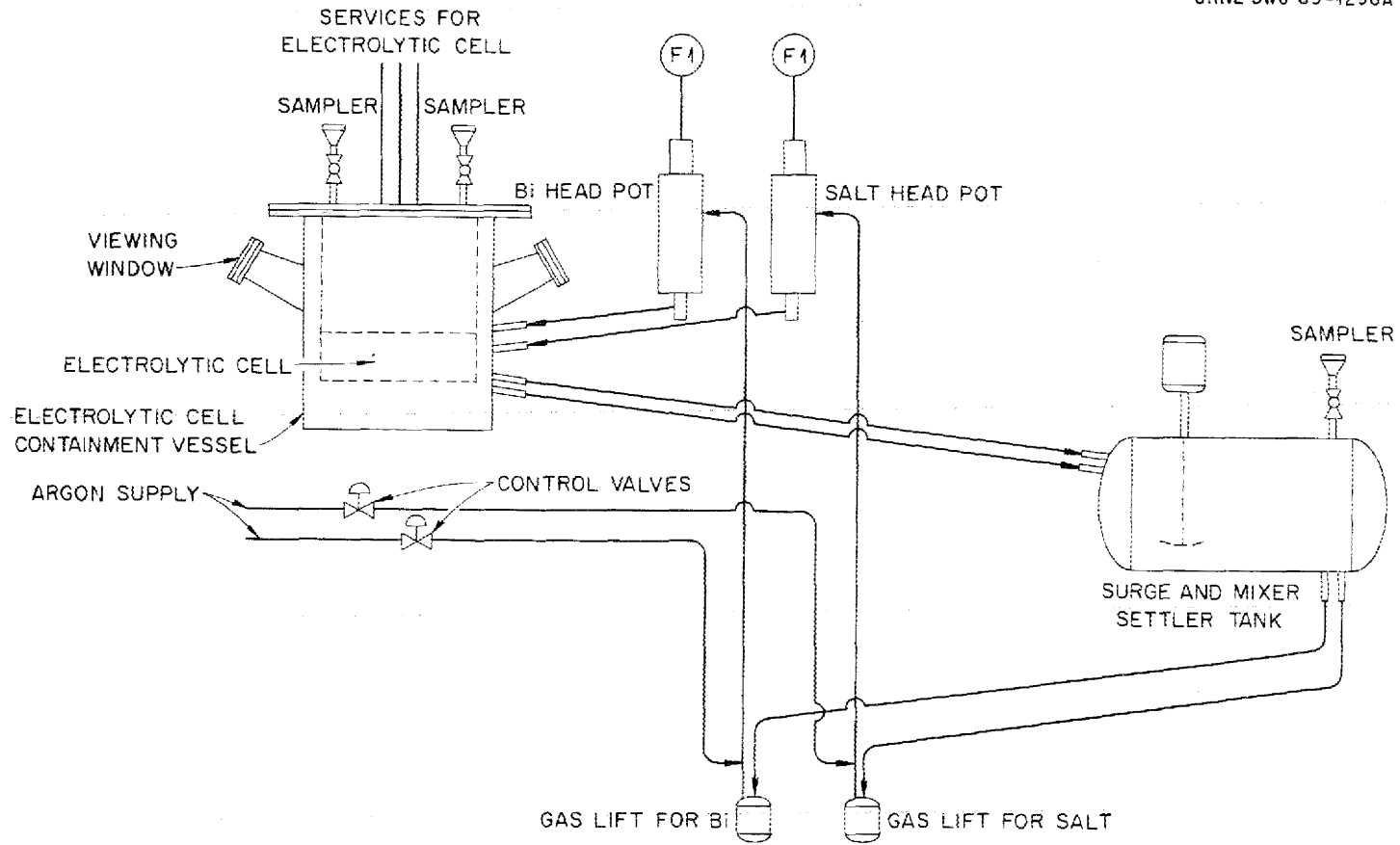
Fig. 51.   Flow Diagram of Salt and Bismuth Recirculation System for Flow Electrolytic Cell Test Facility.

respectively. The bismuth flows into the cathode compartment of the cell, and the salt flows into the region adjacent to the anode and cathode. After exiting from the cell, the salt and bismuth flow to a mixer-settler tank, where they are equilibrated in order to reverse the reaction carried out in the cell. Figures 52 and 53 show the equipment before thermal insulation was applied, while Fig. 54 shows it after installation in a walk-in hood in Bldg. 3541.

8.2 Cell Containment Vessel

The cell containment vessel (Fig. 52) is a 16-in.-diam, 21-in.-high vessel constructed of 1/4-in.-thick stainless steel. The usable space is 15-1/2 in. in diameter and 16 in. deep. The nominal operating temperature is 600°C. Two sight glasses, placed 180° apart in the vessel wall, allow visual observation of the cell. Ports in the top flange allow the cell effluent streams to be sampled. An argon atmosphere is provided.

8.3 Mixer-Settler Vessel

The mixer-settler vessel (Fig. 55) is a carbon-steel horizontal tank, 8 in. in diameter with dished heads, and has a total capacity of about 960 in.^{3}. This vessel is divided into a mixing chamber and a settling chamber by an internal partition. The mixing chamber contains a motor-driven agitator surrounded by four fixed baffles for efficient mixing. A hermetically sealed magnetic clutch couples a variable-speed motor to the tank agitator. The agitator blades and shaft are constructed of molybdenum. Thermocouple wells and bubbler tubes for measuring the liquid level are provided; both are made of molybdenum.

8.4 Gas-Lift Pumps

Tests with mercury have shown that gas lifts are suitable for pumping dense liquids [15] at low flow rates. Two gas-lift tubes ($\sim$ 0.3 in.
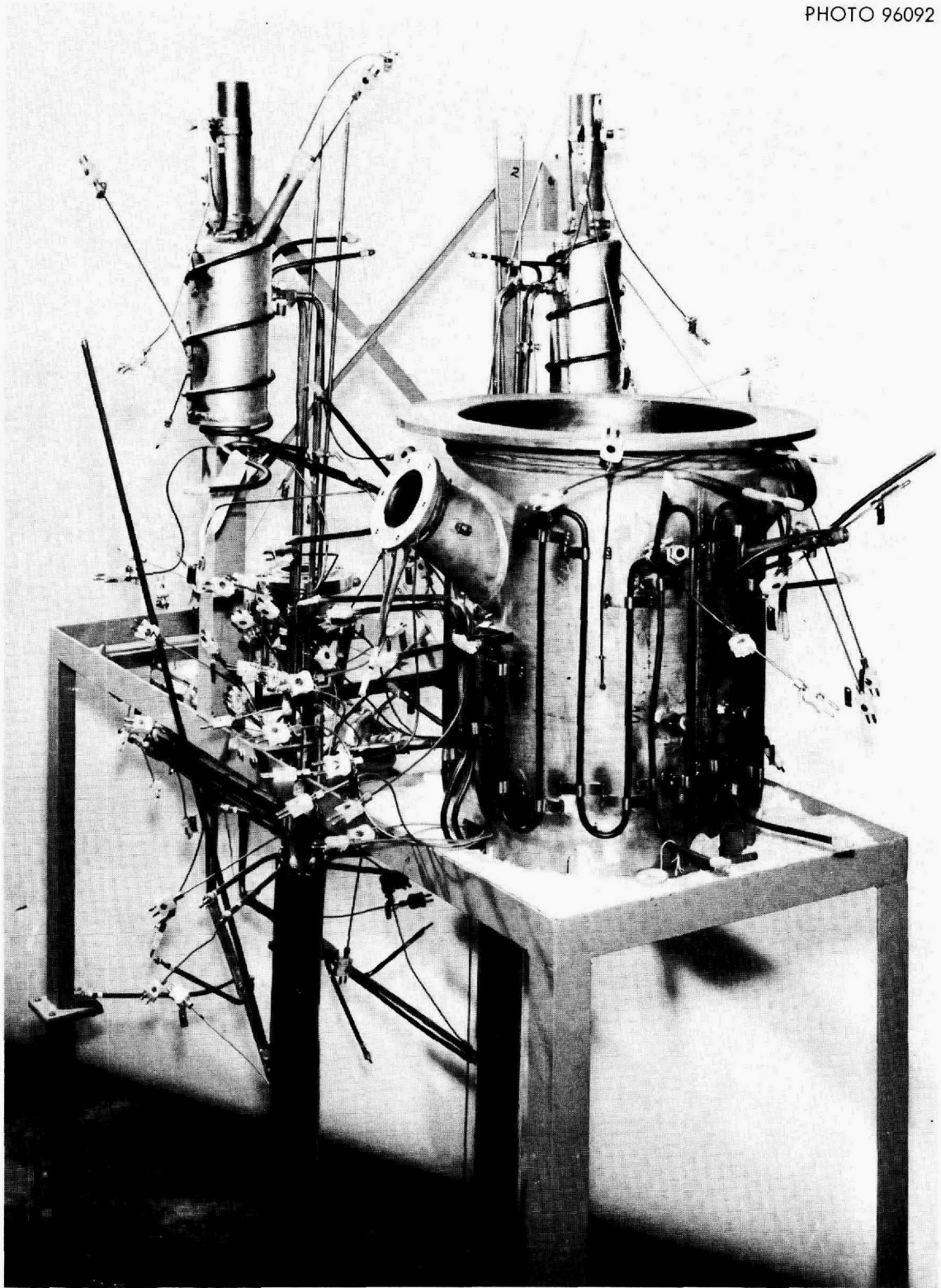
PHOTO 96092

Fig. 52. Flow Electrolytic Cell Test Facility During Construction. View of cell containment vessel and gas-liquid separator vessels.
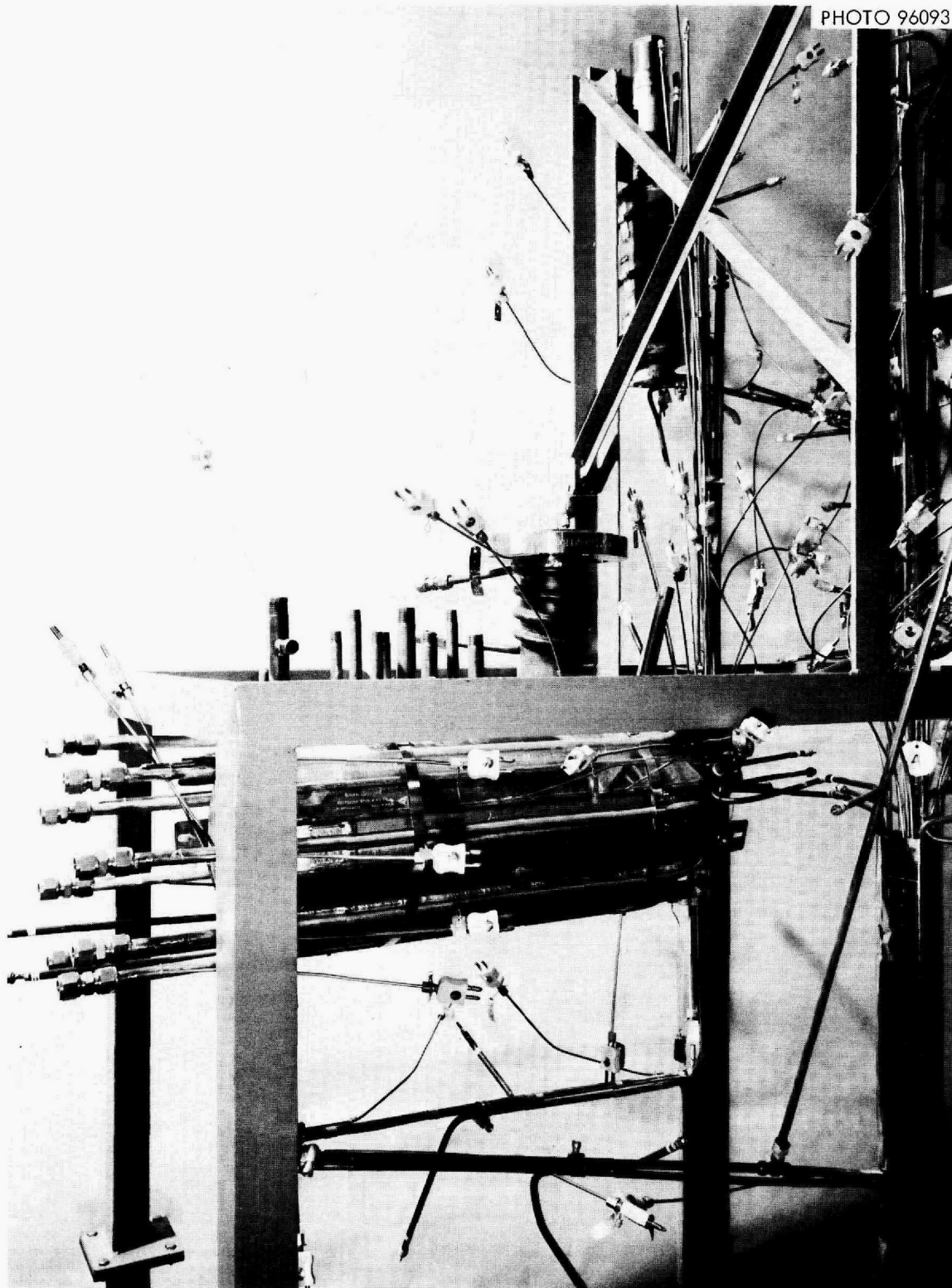
Fig. 53. Flow Electrolytic Cell Test Facility During Construction.
View of mixer-settler vessel.

PHOTO 98569
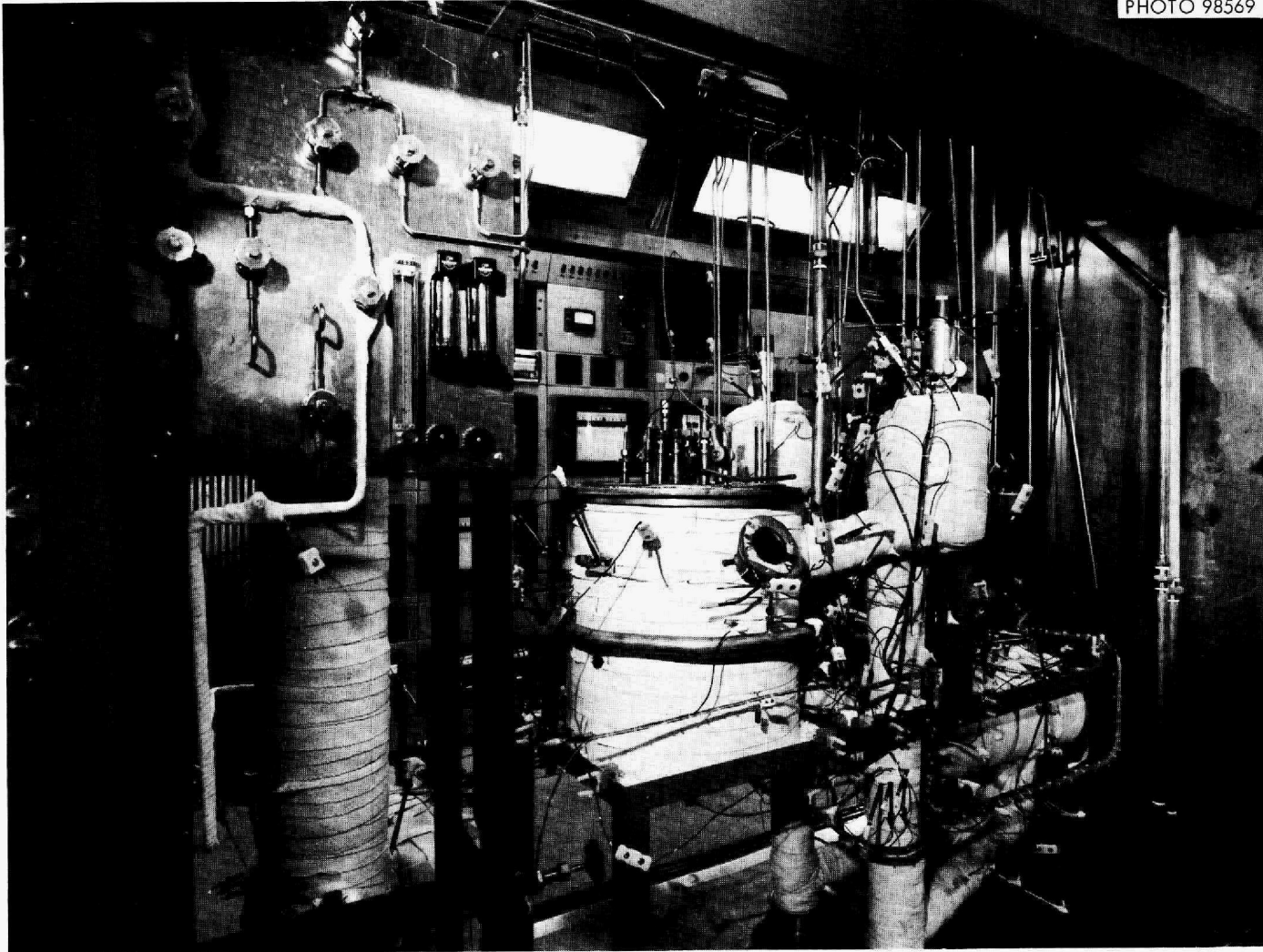
Fig. 54. Flow Electrolytic Cell Test Facility Installed in Hood in Bldg. 3541.

ORNL-DWG-70-8920

NOZZLES FOR BUBBLERS & THERMOWELLS

SAMPLER

BISMUTH INLET

SALT INLET

VESSEL SUPPORTS

22.5in

SAMPLER

MOUNTING FLANGE FOR AGITATOR DRIVE

NOZZLE FOR INSERTION OF CORROSION SPECIMEN

AGITATOR BAFFLES

7.98in

PARTION TO DIVIDE MIXING CHAMBER FROM SEPARATION CHAMBER

SALT OUTLET

8 in. SCHEDULE 40 PIPE, CARBON STEEL

BISMUTH OUTLET

Fig. 55. Diagram of Mixer-Settler Vessel.

ID) are used in parallel for pumping the bismuth; one tube is used for pumping salt. The salt pump and the bismuth pump have submergences of about 58% and about 54% of the lift height, respectively.

8.5 Orifice--Head Pot Flowmeters

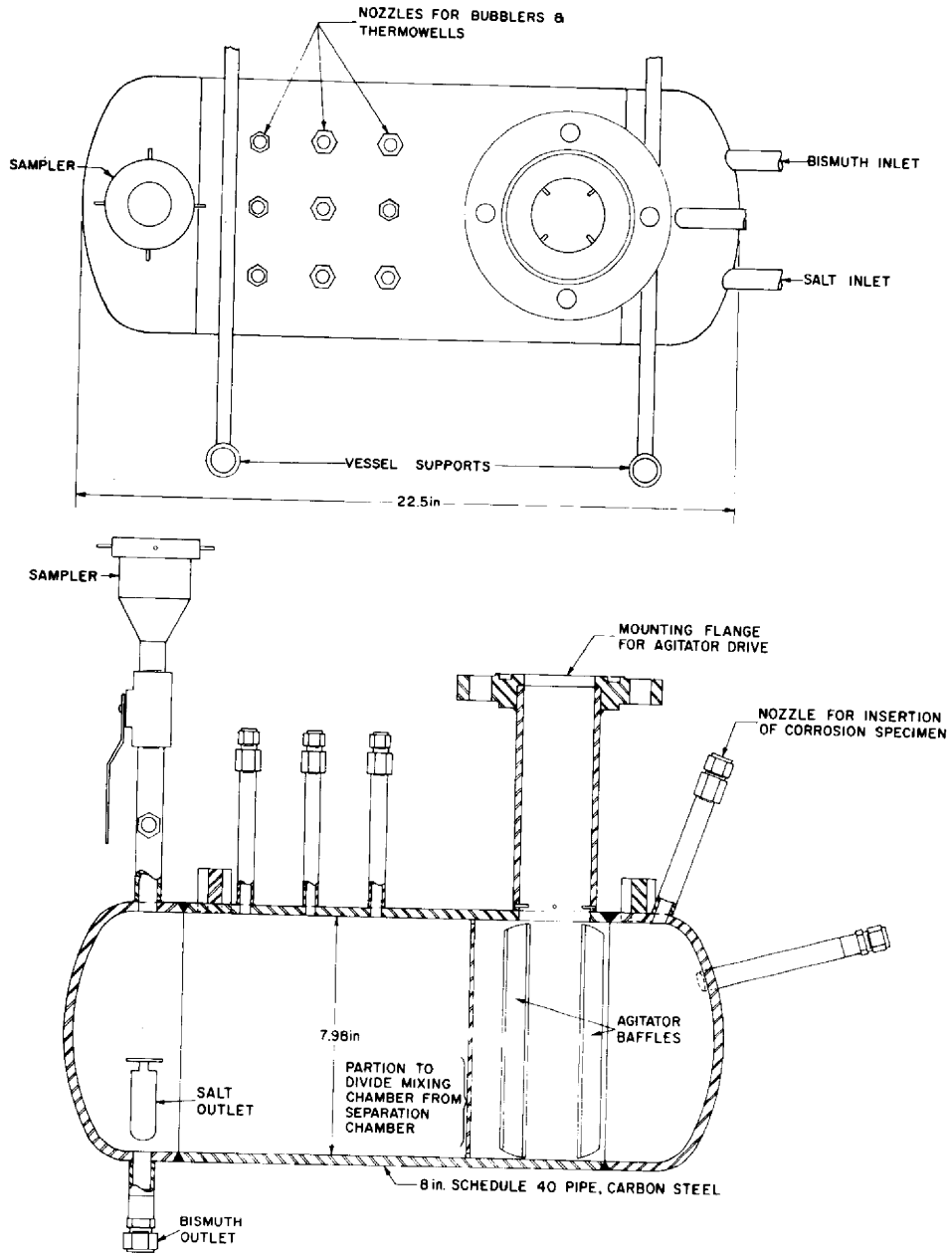The gas-liquid mixtures from the gas-lift pumps discharge into two 4-in.-diam by 7-in.-long carbon-steel disengagement vessels (Fig. 52), which separate the gas and the liquid phases as well as damp surges in the liquid flow rate to the cell vessel. Each vessel (shown schematically in Fig. 56 and in detail in Fig. 57) is divided into two concentric compartments. The outer compartment contains baffles for separating the gas and liquid phases; the inner compartment is designed to produce a pool of quiescent liquid over the orifice through which the liquid discharges. The depth of liquid above the orifice is measured to provide an indication of liquid flow rate. The orifice is located in a plate attached to a spring-loaded cartridge. This plate can be removed if an orifice of a different size is desired. Calibration of orifices in a head pot of this design is discussed in Sect. 9.

8.6 Salt-Metal Treatment Vessel

The salt and the bismuth used in the system must be purified by sparging with HF and hydrogen prior to introduction to the system, as well as periodically during the experimental program. Such treatment removes oxide impurities and reduces corrosion product fluorides to the corresponding metals, which can be removed by filtration. The treatment vessel is a 16-in.-OD by 17-1/2-in.-high vessel constructed of 1/4-in.-thick 304 type stainless steel. It contains a graphite crucible for protection against corrosion. Thermowells, sparge lines, a transfer line, and bubbler tubes made of molybdenum are provided. The transfer line from the treatment vessel contains a filter that consists of a 4-in.-diam by 1/8-in.-thick porous molybdenum disk having a mean pore diameter of about 30 μ.
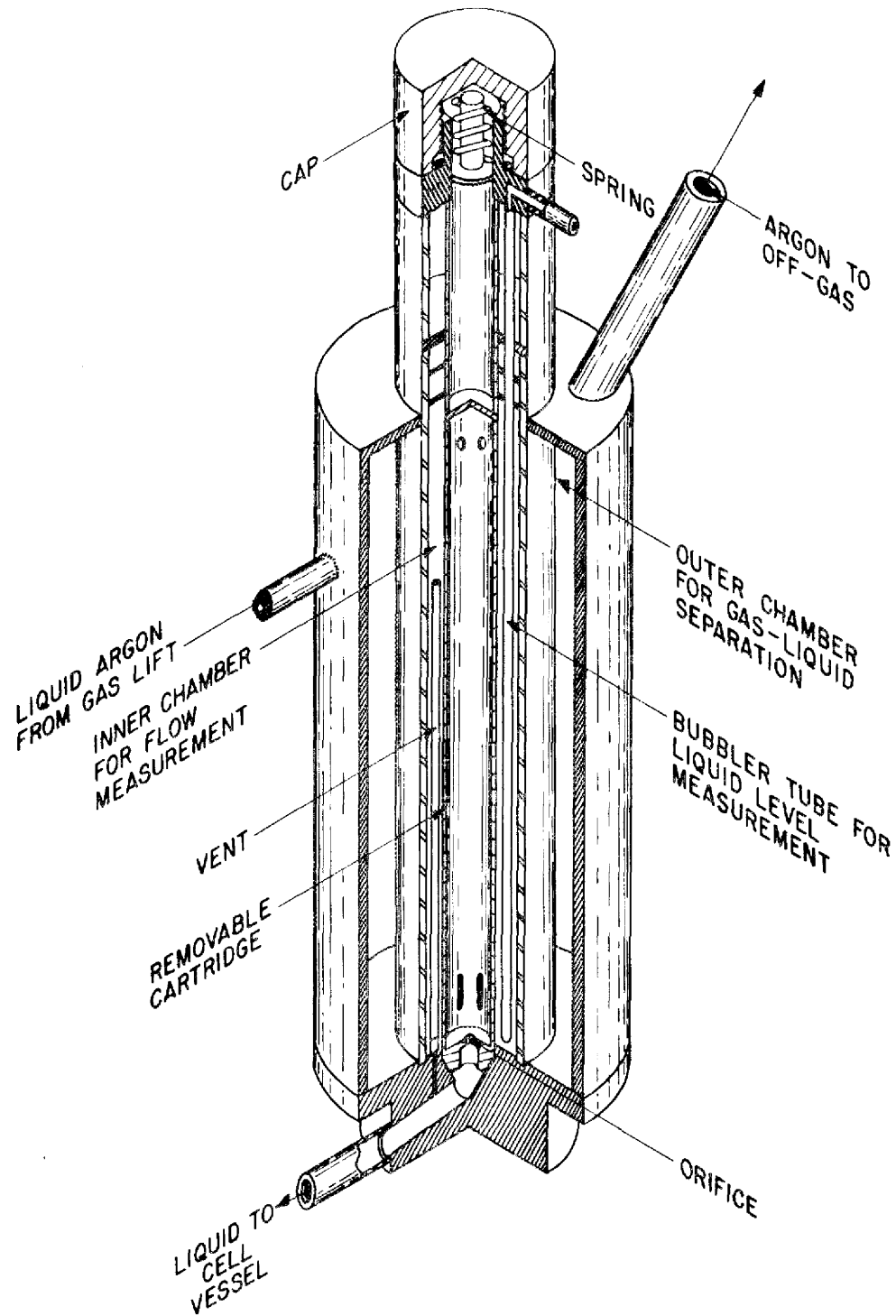
ORNL DWG 70-6241

Fig. 56. Diagram of Vessel for Liquid-Gas Separation and Liquid
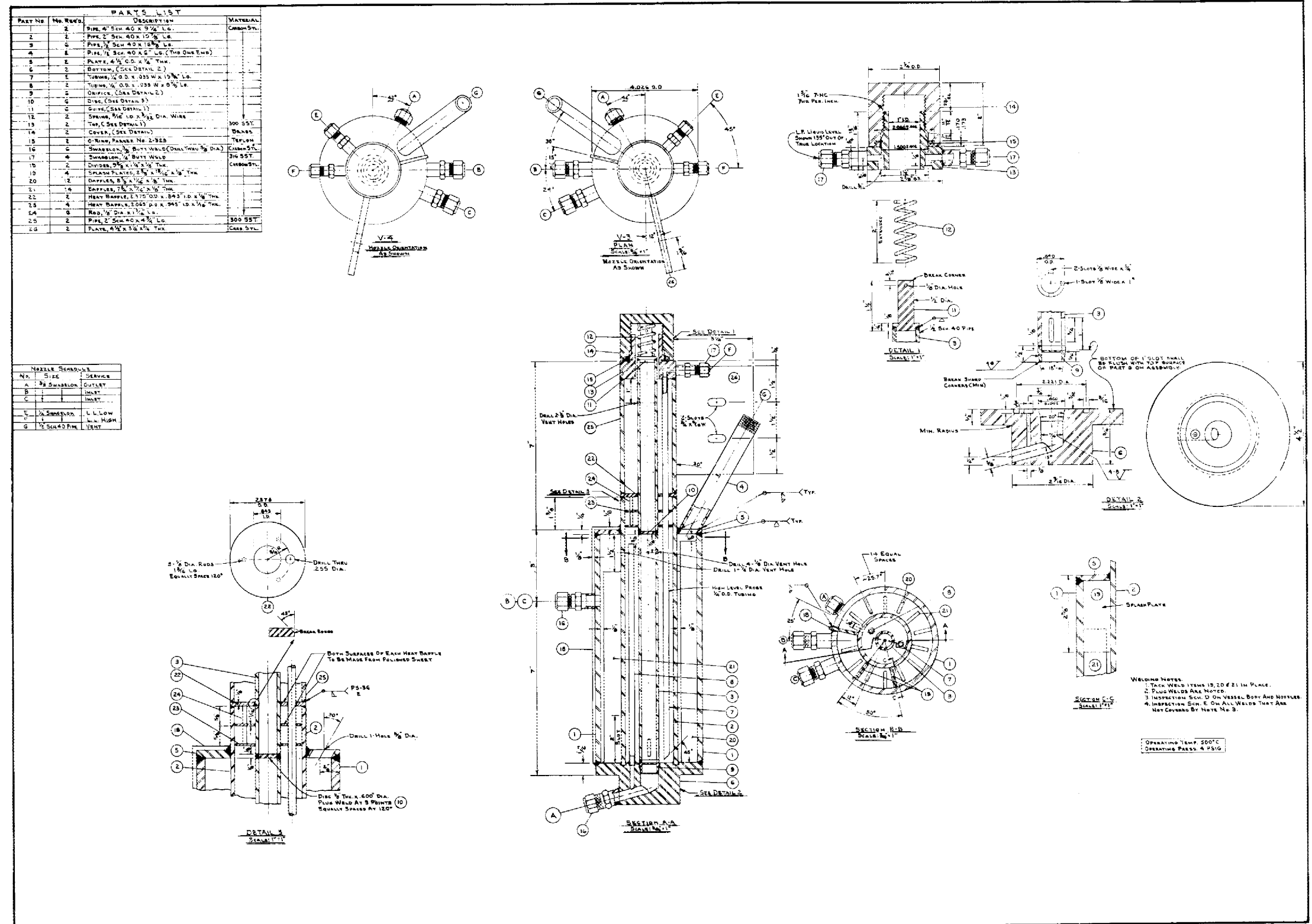Flow Measurement.

Fig. 57. Detailed Design of Orifice--Head Pot Flowmeter.

8.7 Electrolytic Cell

A portion of the first electrolytic cell to be tested is shown in Fig. 58. The vessel, which will contain both the bismuth cathode pool and the electrolyte pool, is fabricated of sections of 5-in. and 8-in. sched 40 carbon-steel pipe. The inlet reservoirs for the bismuth and the salt streams, made of 1-in. sched 40 pipe, are connected to the main cell vessel by 1-in.-long sections of 3/4-in. tubing. The salt and the metal levels are set by the height of a vented 1/2-in.-diam overflow line for each stream.

Preliminary tests with a Lucite model of the vessel (Fig. 59) were made with mercury and water. An air-lift pump was used to circulate mercury through the cell vessel at flow rates up to 0.35 gpm (slightly below the nominal bismuth flow rate). Gas disengagement and mercury flow measurement were effected by a Lucite model of the orifice--head pots described earlier. In general, the Lucite model performed satisfactorily with water flow rates up to 0.25 gpm. These tests resulted in the following observations, and the indicated changes were incorporated in the design of the vessel shown in Fig. 58.

1. The small amount of splashing in the metal inlet reservoir could be contained easily with a loose-fitting splash shield at the top of the inlet reservoir. In the actual vessel, splashing at the overflow lines will be prevented by terminating the end of the overflow line below the level of liquid in the overflow stream sampling reservoir.

2. Frictional losses in the 1/2-in. inlet lines and 3/8-in. overflow lines of the mock-up caused the levels in the inlet reservoirs to be excessively high. These lines were

PHOTO 98322

Fig. 58. Cell Vessel for Flowing Salt and Bismuth Streams Through the Bismuth Cathode Pool and the Electrolyte Pool.
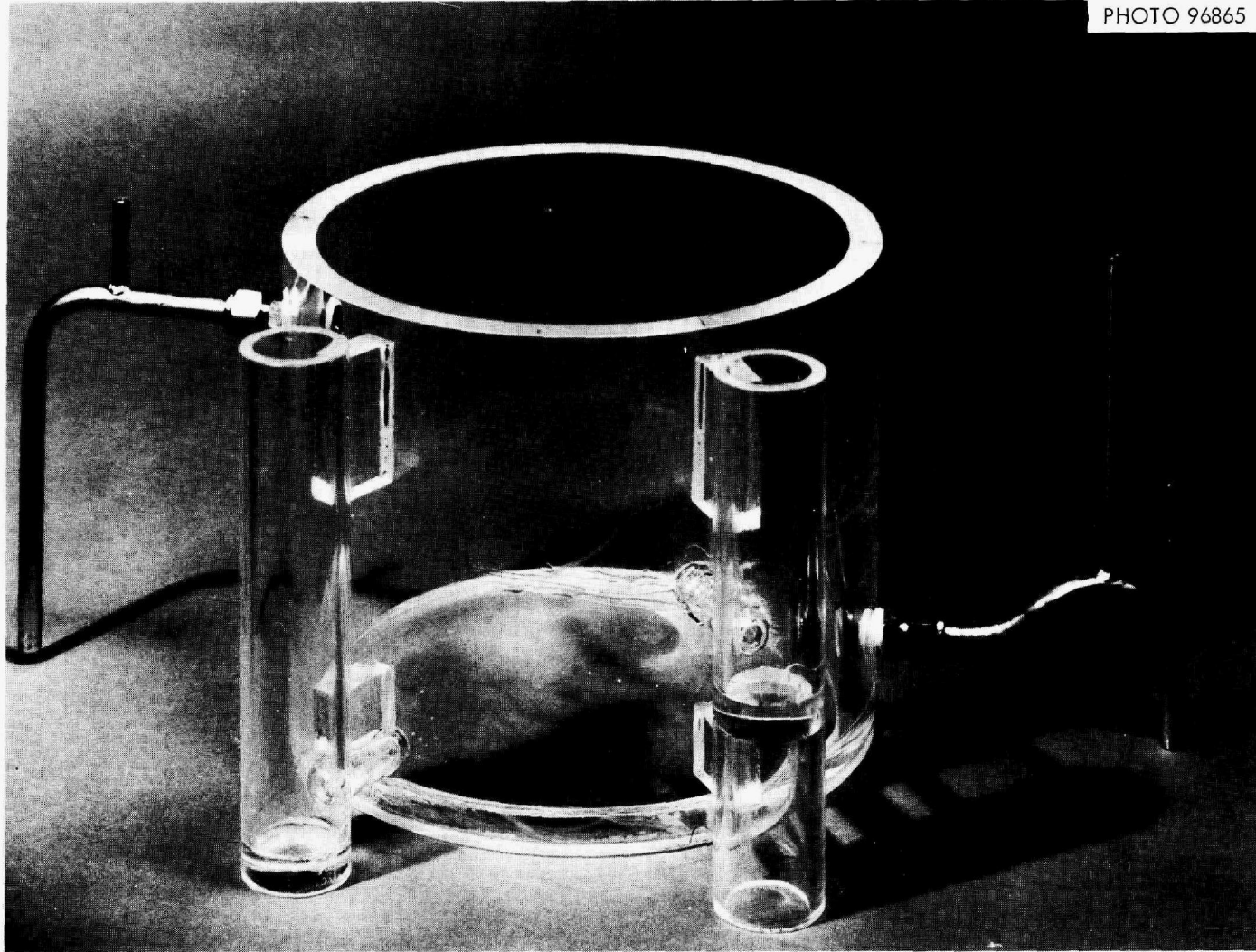
PHOTO 96865

Fig. 59. Lucite Mock-Up of Cell Vessel for Testing the Capability of the Cell Vessel for Handling the Flowing Streams.

8.8 Power Supply

The dc power supply has an output of 0 to 24 V, a maximum current of 750 A, and a 4.2% rms ac component. The unit, which can be controlled remotely, has provisions for automatic voltage control as well as automatic current control. (Or, if desired, it can be controlled manually.) The automatic voltage control will maintain constant voltage within $\pm$ 2% in the 0- to 24-V range; the automatic current control will maintain constant current within $\pm$ 2% in the range 75 to 750 A.

8.9 Status of Equipment

Except for the power supply, all of the equipment for the Flow Electrolytic Cell Facility has been installed. The power supply has been received. All of the electrical work associated with thermocouples and heater power supplies has been completed.

9. CALIBRATION OF AN ORIFICE--HEAD POT FLOWMETER WITH MOLTEN SALT AND BISMUTH

C. W. Kee   B. A. Hannaford

The Flow Electrolytic Cell Facility (FECF) discussed in Sect. 8 contains orifice--head pot flowmeters for measuring the rates at which salt and bismuth flow through the test cell. Calibration and study of these units, which are of a nonstandard design (Sect. 8.5), are being carried out prior to operation of the FECF to ensure that uncertainties in flow rates will be acceptably small.

The initial tests were carried out with transient flows of both water and mercury through a Lucite model. Subsequently, tests were carried out with both transient and steady flows of salt and bismuth in a metal orifice--head pot flowmeter. Details of the tests and the data that were obtained are discussed in the remainder of this section.

9.1 Mathematical Analysis

Flow through a standard sharp-edged orifice can be predicted from the relation

$$Q\rho = C_d \, A \, \sqrt{2\rho\Delta P}, \tag{24}$$

where Q = flow rate of the liquid,

ρ = density of the liquid,

A = cross-sectional area of the orifice,

ΔP = pressure drop across the orifice,

C_d = orifice coefficient.

The objectives of the present studies are twofold: (1) to verify the applicability of this relation to the orifice—head pot flowmeters, and (2) to determine the orifice coefficient. The orifice coefficient can be calculated directly from Eq. (24) by using data obtained during steady flow, or from a more convenient relation that was derived for use with transient flow.

In the transient flow tests, the head pot was first filled with molten salt or bismuth to the desired level. Then the fluid was allowed to drain from it, and the liquid level was determined several times during the drainage period. Since the head pot is of constant cross section, the discharge rate is related to changes in the liquid level in the head pot during the drainage period as follows:

$$Q = \frac{d\ell}{dt} A_h, \tag{25}$$

where Q = liquid discharge rate,

ℓ = liquid level above orifice,

t = time,

A_h = cross-sectional area of head pot.

The pressure drop across the orifice is related to the liquid level as follows:

$$P = \ell \rho g,$$

where g = gravitational constant.

Thus, Eq. (25) can be written as

$$Q = - \frac{A_h}{\rho g} \frac{d\Delta P}{dt} .$$ (26)

Combining Eqs. (24) and (26) yields

$$\frac{d\Delta P}{\sqrt{\Delta P}} = - \frac{C_d A g}{A_h} \sqrt{2\rho} \; dt.$$ (27)

The solution to Eq. (27), with the initial condition that

$$\Delta P = (\Delta P)_{initial} \text{ at } t = 0,$$

is

$$\sqrt{\Delta P} = - \frac{C_d A g}{2 A_h} \sqrt{2\rho} \; t + \sqrt{(\Delta P)_{initial}}.$$ (28)

Thus, a plot of $\sqrt{\Delta P}$ vs t should yield a straight line having a slope of $(- C_d A g \sqrt{2\rho}/2 A_h)$.

9.2 Data Obtained from Transient Flow in a Lucite Orifice—Head Pot Flowmeter

During the initial experiments with water in the Lucite head pot, it was observed that the orifice drain chamber became filled with water when the level in the head pot was greater than about 0.5 in. A submerged orifice is undesirable for this orifice—head pot design since the pressure downstream of the orifice will not be known unless the downstream chamber is filled with gas. This problem was solved by enlarging the orifice drain chamber and conducting all subsequent experiments with an unsubmerged orifice.

The times required for the head-pot level to reach certain predetermined points were measured in ten runs with water and three runs with mercury. The measured values were averaged for each head-pot level; the resulting data for water and mercury are shown in Figs. 60 and 61, respectively.

Over most of the range of flow rates studied, constant orifice coefficients were observed with both water and mercury. As expected, a decrease in orifice coefficient occurred at low flow rates. However, one would not normally operate in this region, since significant errors in pressure drop could result from uncertainties in the differential pressure transmitter zero and in the distance between the orifice and the bubbler tube used for measuring the upstream pressure.

9.3 Data Obtained from Transient Flow in a Metal Orifice—Head Pot Flowmeter

Four experiments were run in which the drainage of molten salt or bismuth from a mild-steel head pot was observed. The data obtained with bismuth (Figs. 62 and 63) indicate a constant orifice coefficient having a value of 0.646, which is approximately equal to the orifice coefficient obtained with mercury (0.663). Deviation of the points from the line in the early part of the experiment (see Fig. 63) results from the fact that bismuth was still flowing into the head pot during this period.
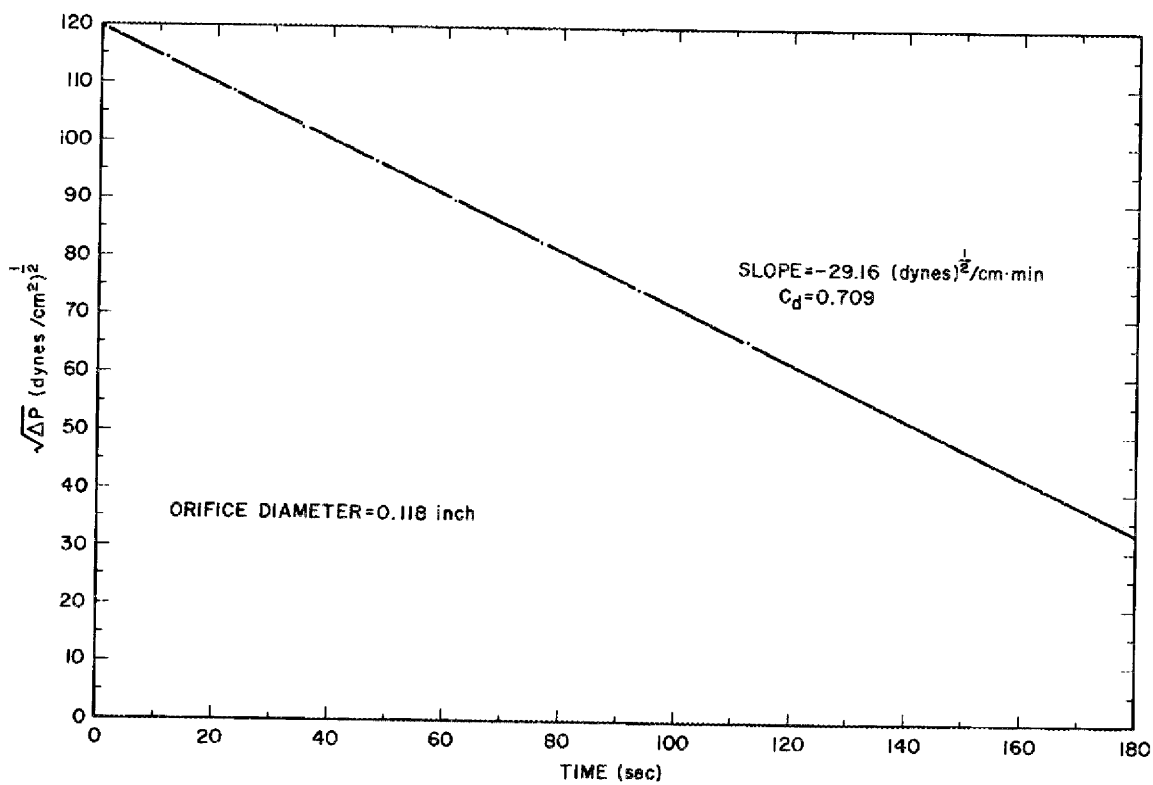
Fig. 60. Calibration Data Obtained During Drainage of Water from the Lucite Head Pot.
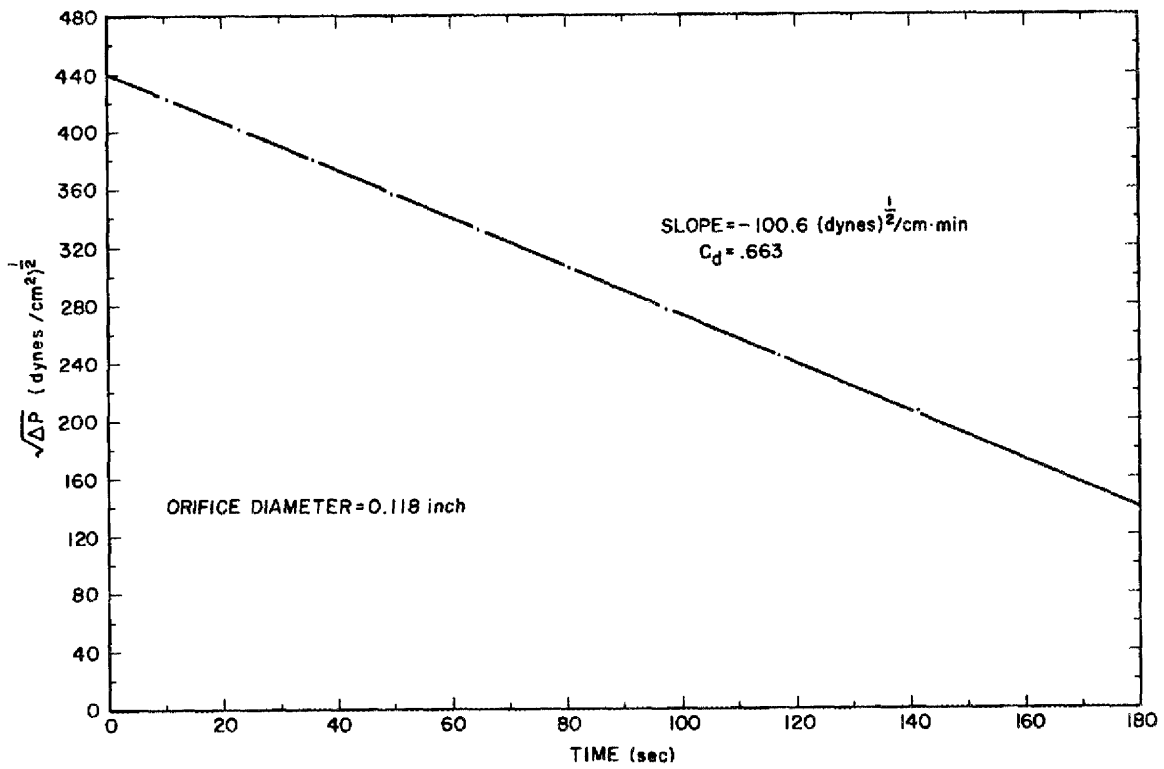
Fig. 61. Calibration Data Obtained During Drainage of Mercury from the Lucite Head Pot.
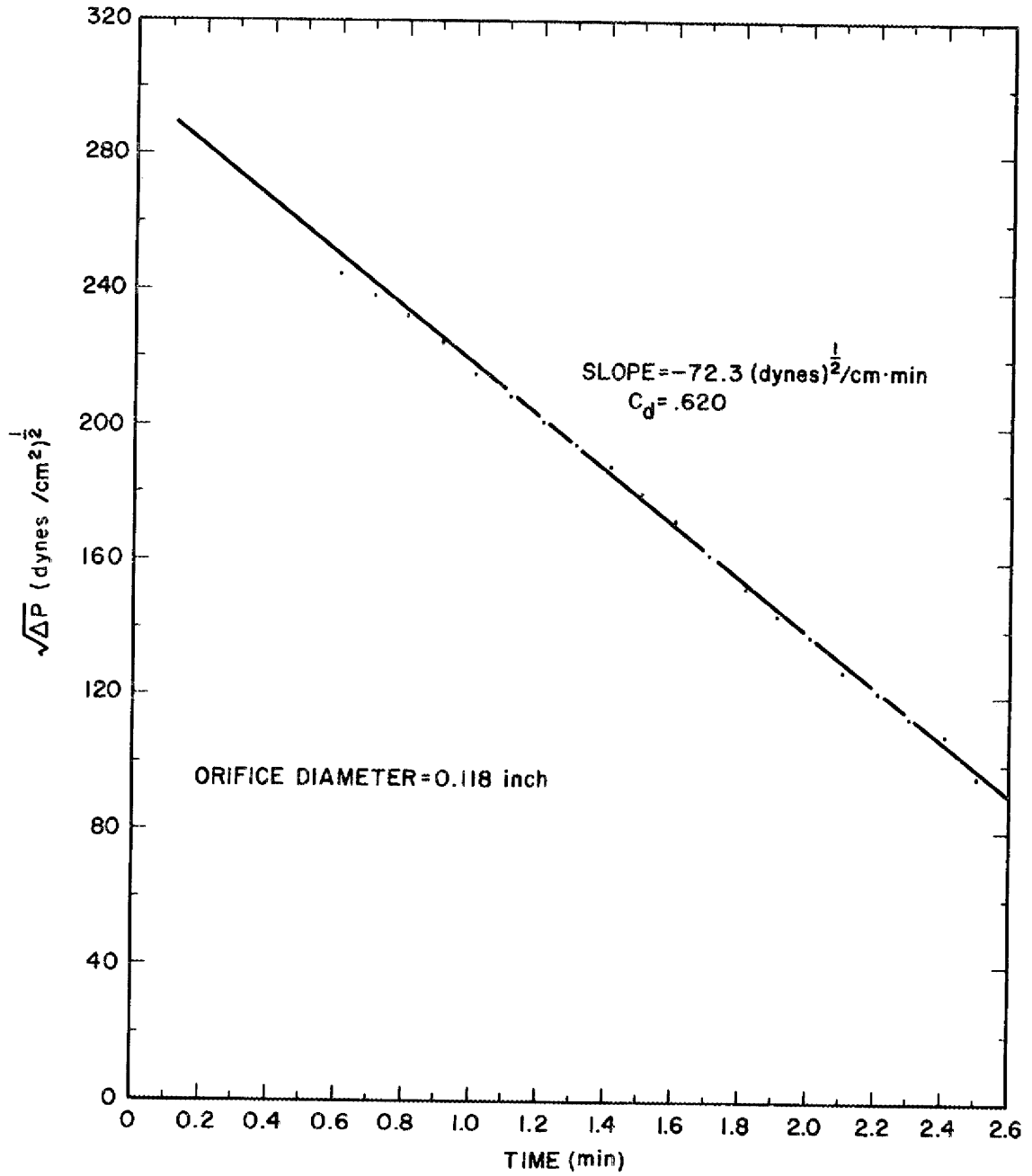
Fig. 62. Calibration Data Obtained During Drainage of Bismuth from a Mild-Steel Head Pot at 600°C. Run OP-1.
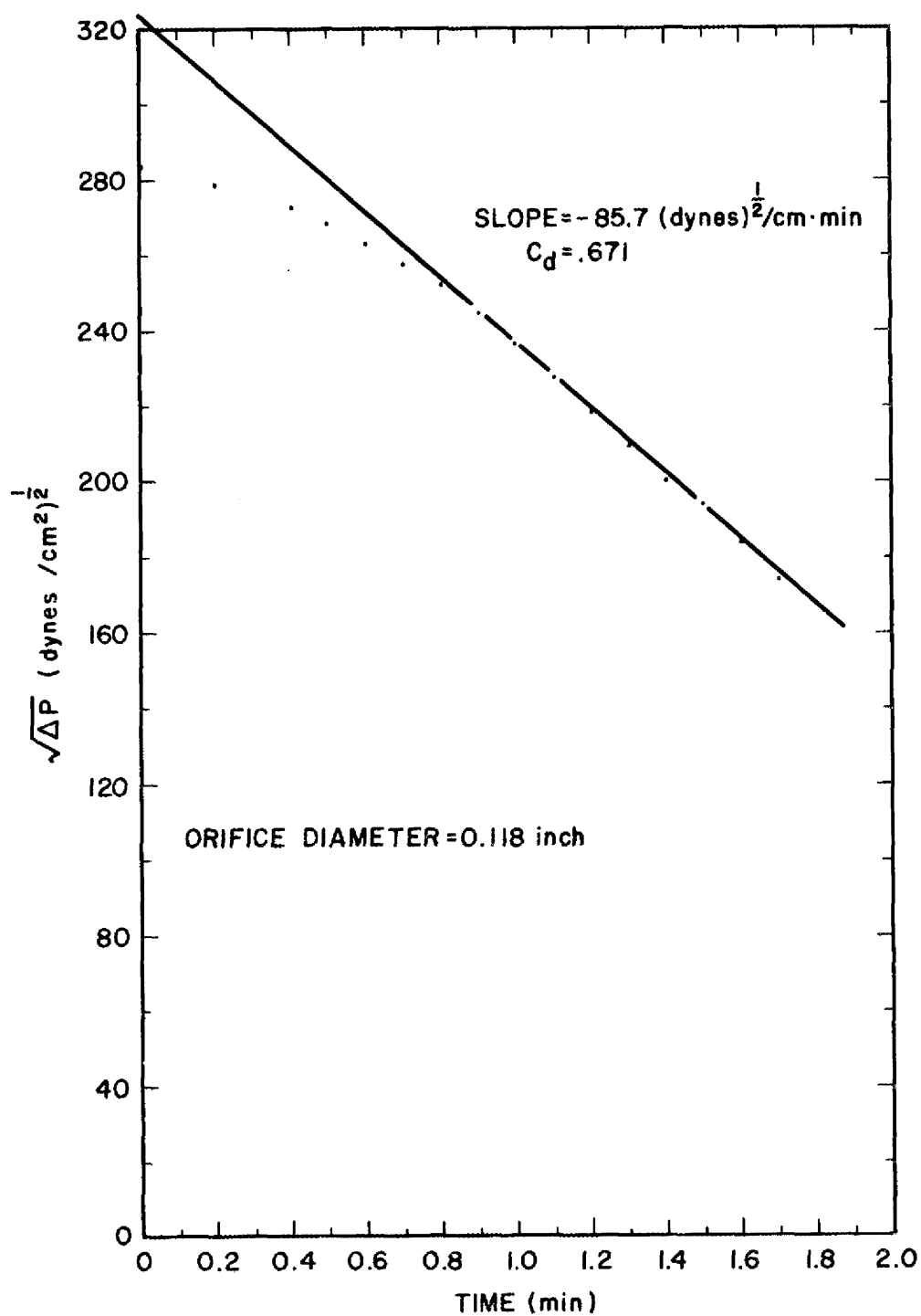
ORNL DWG 71-56

Fig. 63. Calibration Data Obtained During Drainage of Bismuth from a Mild-Steel Head Pot at 600°C. Run OP-2.

The data obtained with salt (Figs. 64 and 65) also show a constant orifice coefficient. The value of this coefficient (0.402) is lower than that obtained with water (0.709) and reflects the higher viscosity of the molten salt.

9.4 Data Obtained from Steady Flow of Bismuth in a Metal Orifice---Head Pot Flowmeter

Three calibration experiments were made in which a steady flow of bismuth was maintained through the mild-steel head pot. Orifice coefficients calculated from data obtained during four periods of constant pressure drop across the 0.118-in.-diam orifice are given in Table 5. Although the orifice coefficient values agree favorably with the average value obtained with transient flow (0.646), additional data are needed to reduce the level of uncertainty in the value of the orifice coefficient. The orifice was removed periodically for inspection during these experiments. No evidence of corrosion, plugging, or deposition was noted.

Table 5. Data Obtained from Calibration of a 0.118-in.-diam Orifice with Steady Flows of Bismuth at 600°C

Duration of Steady Flow (min)	Orifice Reynolds Number	Orifice Coefficient
16.5	20,200	0.66
12.0	29,800	0.623
2.25	47,300	0.82
8.25	49,800	0.68

10. BISMUTH-SALT INTERFACE DETECTOR

J. Roth   L. E. McNeese

A salt-metal interface detection device is needed for the detection and control of the interface location in salt-metal extraction columns. Such a device may also permit the detection of uncoalesced bismuth in

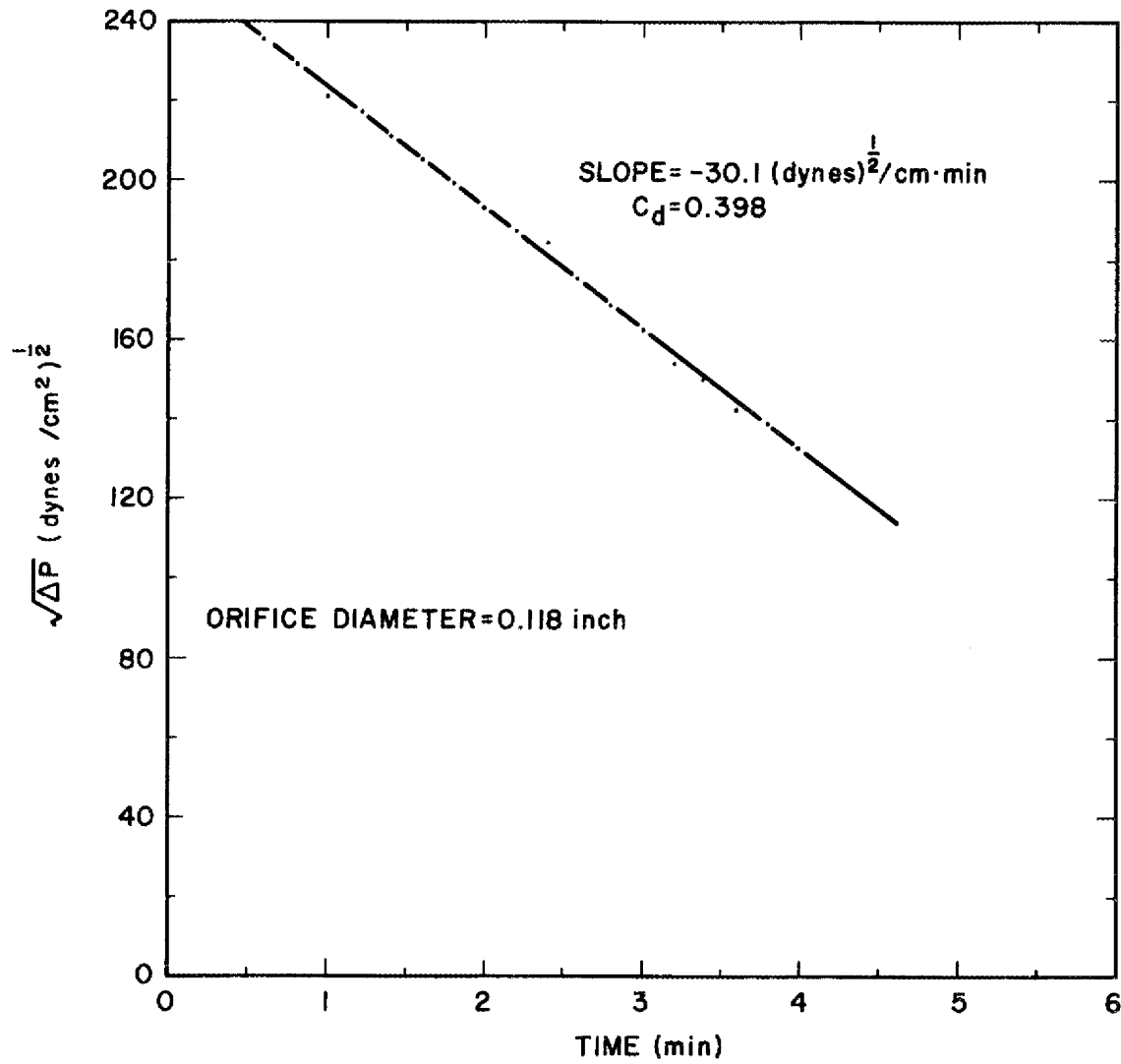Fig. 64. Calibration Data Obtained During Drainage of Molten Salt from a Mild-Steel Head Pot at 600°C. Run OP-4 (Part 1).
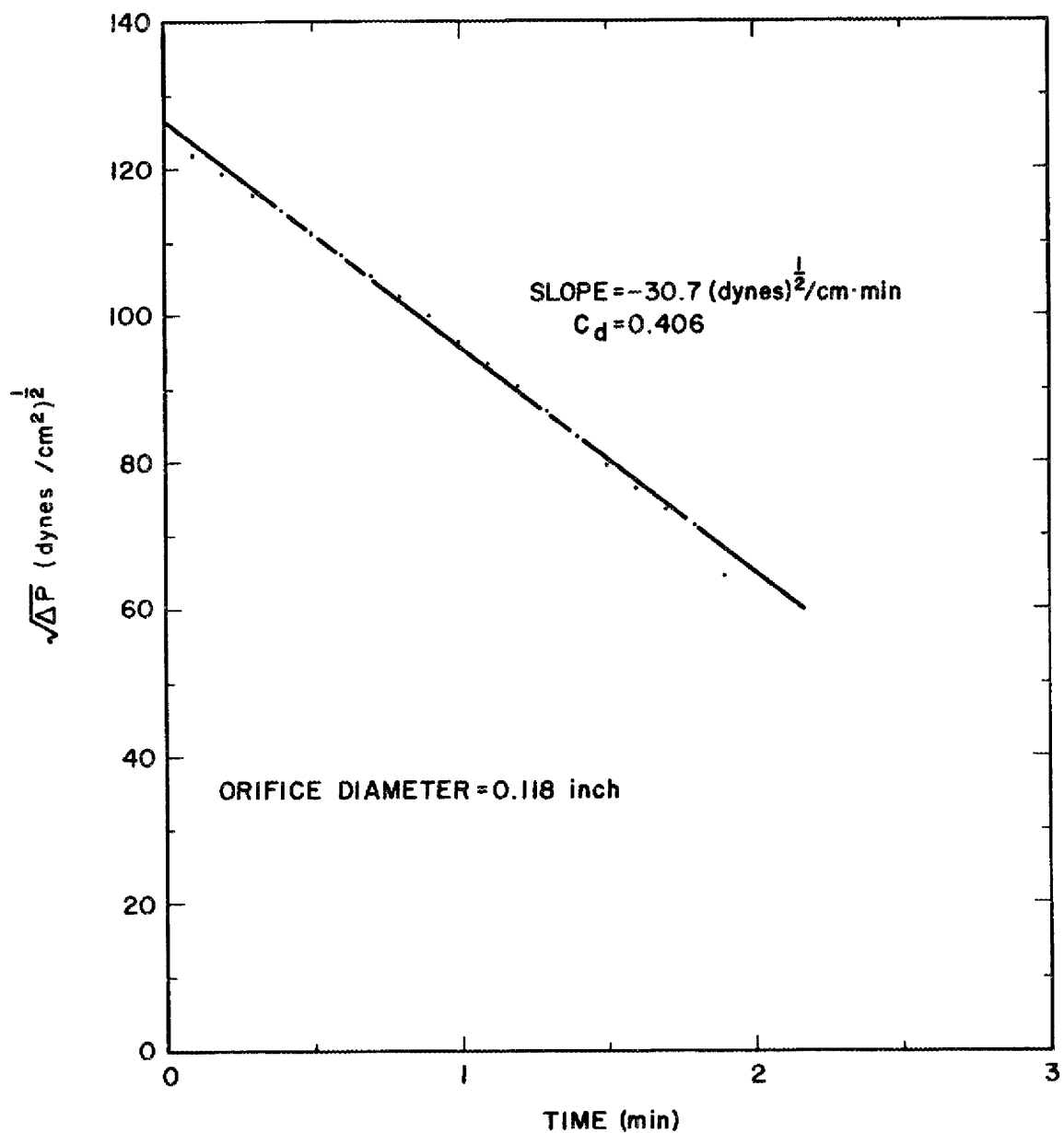
Fig. 65. Calibration Data Obtained During Drainage of Molten Salt from a Mild-Steel Head Pot at 600°C. Run OP-4 (Part 2).

the vicinity of the interface. A modified version of a liquid-level induction probe developed at Argonne National Laboratory[15] has been built, and a study of this probe is presently under way.

10.1 Inductance Coil

The inductance coil, shown in Fig. 66, consists of a 12-in.-long bifilar winding of 30-gage platinum wire. The platinum wire is wound in grooves, which have been machined into the surface of a tubular lavite form having an outside diameter of 15/16 in. and an inside diameter of 9/16 in. These grooves are 0.015 in. wide, 0.015 in. deep with a round bottom, and are separated by 0.035 in. of lavite. The coil contains ten turns per inch. Protective collars, 1 in. wide by 1-7/16 in. in diameter, are located at each end of the coil. The coil leads are twisted pairs to ensure minimal connecting lead inductance. The entire assembly has been coated with a ceramic glaze* to reduce the possibility of external shorting of the coils.

10.2 Electronics System

The input to the primary coil is supplied by a Wavetek Function Generator Model 110** and is typically 20 kc at 2 V. The output of the secondary coil is amplified to about 6 V, rectified, and filtered. The residual current is suppressed to eliminate the zero-level signal, and the differential voltage (e.g., 10 mV dc) is amplified and fed to a strip-chart recorder. When the electronics for this system have been tested under conditions similar to those which will be encountered in actual practice, the wiring diagram will be finalized and reported.

---

*0-900 glaze marketed by the Physical Sciences Corporation, a subsidiary of the Friden Singer Co., Arcadia, Calif.
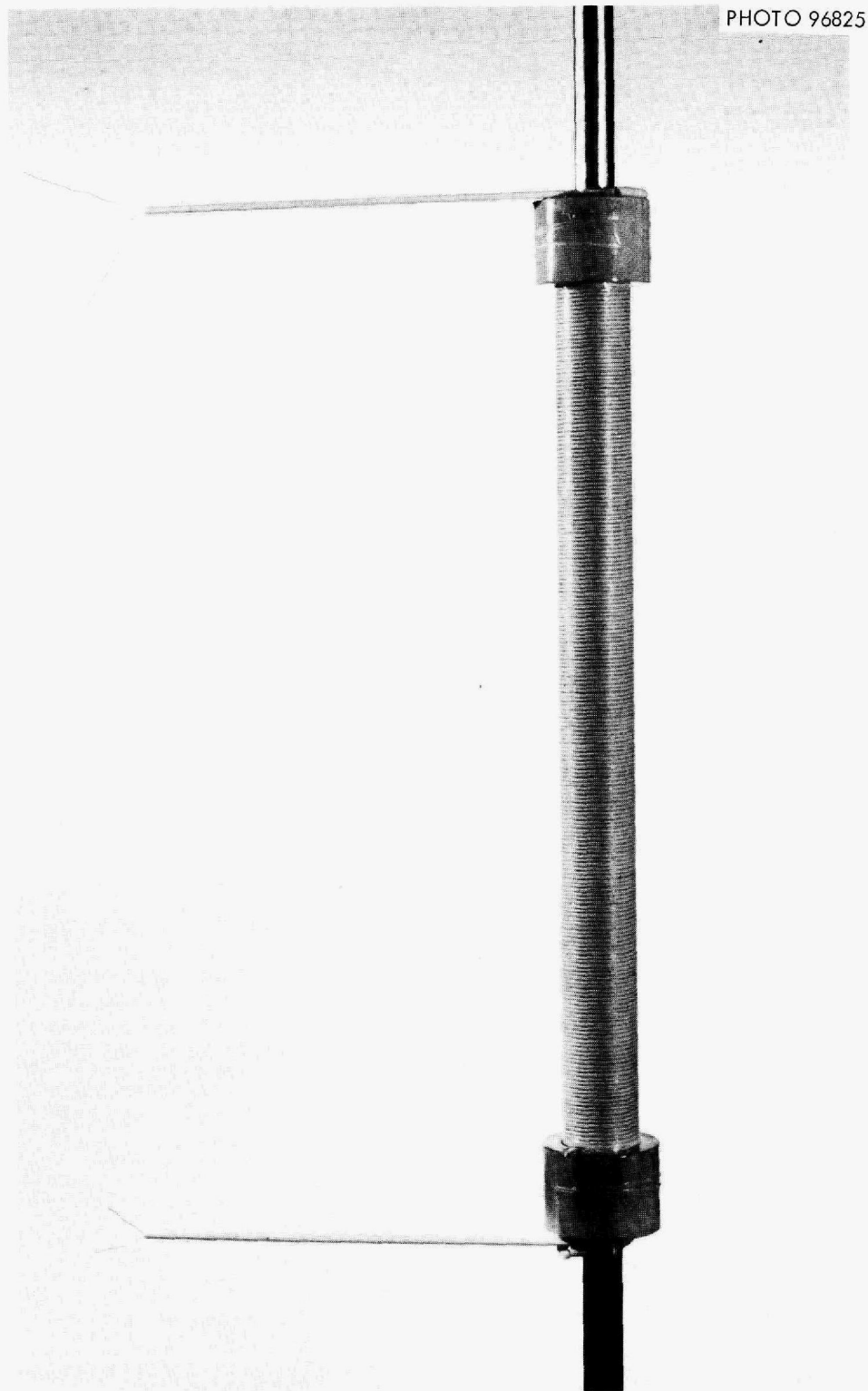
**Obtained from Wavetek Corporation, San Diego, Calif.

Fig. 66. Bismuth-Salt Interface Detector Coil.

10.3 Auxiliary Equipment

A liquid bismuth reservoir has been designed and will be fabricated from carbon steel. Capabilities for in situ purification of the bismuth and for control of temperature, pressure, and cover gas have been provided. The interface detector will be mounted for testing on a seamless type 316 stainless steel tube having a 0.065-in. wall and an outside diameter of 0.500 in. The portion of the inside length of the tube that will be in contact with liquid bismuth is being coated with a 0.005-in. layer of tungsten. Similarly, the portion of the outside diameter of the tube that will be located inside the liquid bismuth reservoir will be coated with a 0.005-in. layer of tungsten to preclude the possibility of a reaction taking place between the bismuth and the stainless steel.

11. STRIPPING OF ThF_4 FROM MOLTEN SALT BY REDUCTIVE EXTRACTION

L. E. McNeese   C. P. Tung

Efficient operation of the reductive extraction system for rare-earth removal requires[16] that only a negligible quantity of ThF_4 remain in the salt which passes through the electrolytic cell and returns to the bottom of the extraction column. It has been proposed that this low ThF_4 concentration be maintained by stripping the ThF_4 from salt that is fed to the cell by countercurrent contact with a lithium–bismuth stream produced at the cell cathode. We have made calculations showing the extent to which ThF_4 can be removed from the salt with a column containing one to four theoretical stages. It was assumed that the salt entering the stripping column had the composition 72-16-12 mole % $LiF-BeF_2-ThF_4$ and that the metal entering the column consisted of a lithium–bismuth mixture having a lithium concentration of 0.008 mole fraction. The metal-to-salt molar flow rate ratio, based on the feed streams, was 74.6.

The fraction of the ThF_4 remaining in the salt stream that left the column is shown in Fig. 67 as a function of the number of theoretical stages used. With one theoretical stage, the fraction of ThF_4 remaining
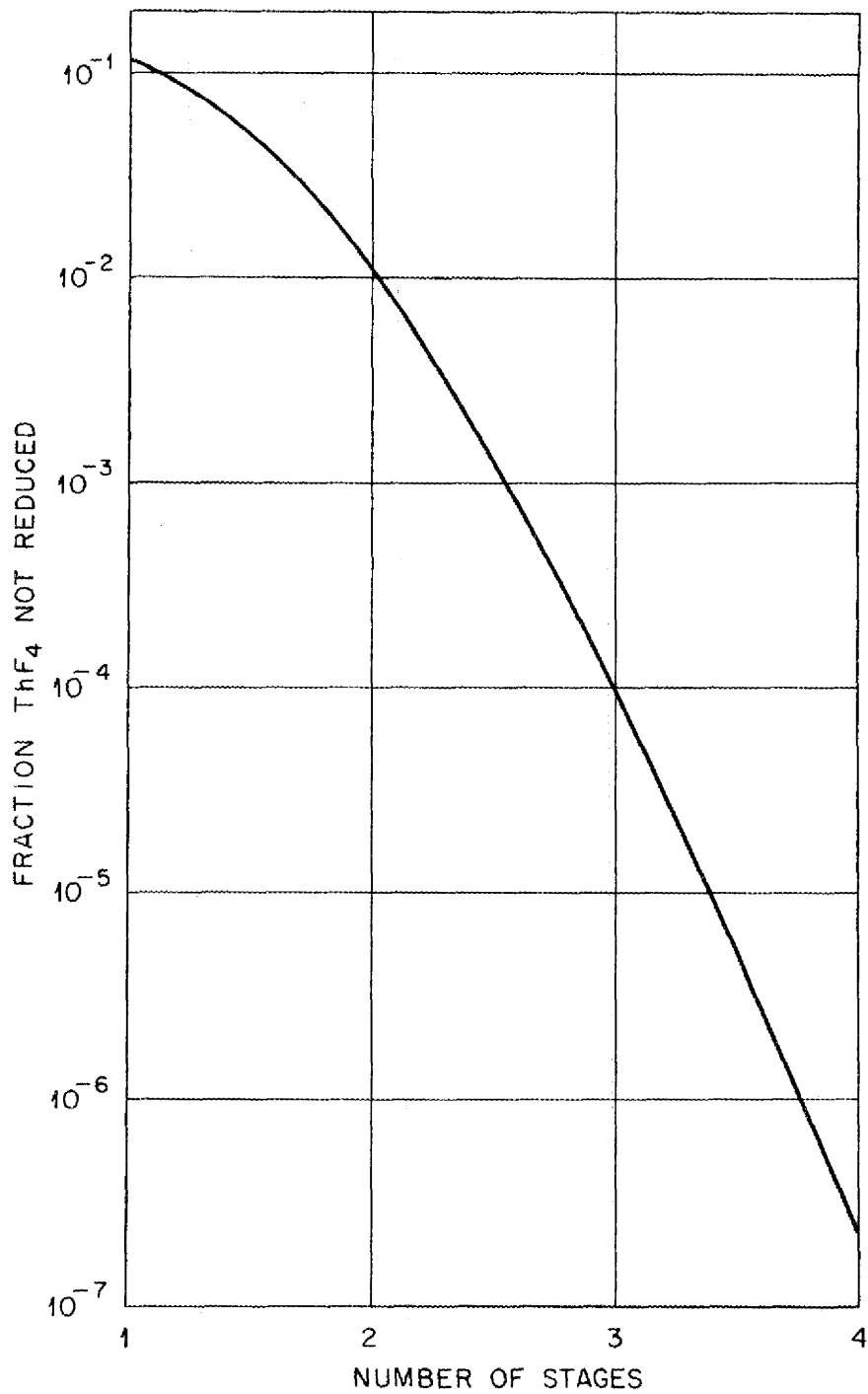
Fig. 67. Fraction of ThF_4 Remaining in Salt After Countercurrent Contact with a Li-Bi Stream for a Column Having a Variable Number of Stages.

in the salt stream is approximately 0.12; the fractions for two, three, and four stages are 0.013, 0.96 x 10^{-4}, and 2.16 x 10^{-7}, respectively. Since the required fractional ThF_4 removal is about 0.99, two to three theoretical stages will be sufficient to maintain the desired fractional removal of ThF_4.

12. REFERENCES

1. H. D. Cochran et al., Engineering Development Studies for Molten Salt Breeder Reactor Processing No. 3, ORNL-TM-3138 (May 1971), p. 30.

2. C. A. Sleicher, A.I.Ch.E. J. 5, 145 (1959).

3. T. Miyauchi and T. Vermeulen, Ind. Eng. Chem., Fundamentals 2, 113 (1963).

4. S. Hartland and J. C. Mecklenburgh, Chem. Eng. Sci. 21, 2109 (1966).

5. V. Rod, Collection Czech. Chem. Commun. 34, 387 (1969).

6. S. Stemerding and F. J. Zuiderweg, The Chemical Engineer, p. CE156 (May 1963).

7. P. V. Danckwerts, Chem. Eng. Sci. 2, 1 (1953).

8. T. Vermeulen, J. S. Moon, A. Hennico, and T. Miyauchi, Chem. Eng. Progr. 62 (No. 9), 95 (1966).

9. MSR Program Semiann. Progr. Rept. Feb. 28, 1969, ORNL-4396, p. 272.

10. T. R. Johnson, R. D. Pierce, F. G. Teats, and E. F. Johnston, A.I.Ch.E. J. 17, 14-18 (1971).

11. W. B. Argo and D. R. Cova, Ind. Eng. Chem., Process Design Develop. 4, 356 (1965).

12. W. Siemes and W. Weiss, Chem. Ing. Techn. 29, 727 (1957).

13. L. E. McNeese, Engineering Development Studies for Molten-Salt Breeder Reactor Processing No. 3, ORNL-TM-3138 (May 1971), p. 54.

14. H. W. Kohn and F. F. Blankenship, MSR Program Semiann. Progr. Rept. Aug. 31, 1968, ORNL-4344 (February 1969), p. 150.

15. M. S. Lin and L. E. McNeese, Unit Operations Section Quarterly Progress Report July-September 1968, ORNL-4366 (April 1970), p. 47.

16. T. R. Johnson, F. G. Teats, and R. D. Pierce, An Induction Probe for Measuring Liquid Levels in Liquid Metals, ANL-7154 (February 1966).

INTERNAL DISTRIBUTION

1.	C. F. Baes	42.	E. L. Nicholson
2.	H. F. Bauman	43.	J. H. Pashley (K-25)
3.	S. E. Beall	44.	A. M. Perry
4.	M. J. Bell	45-46.	M. W. Rosenthal
5.	R. E. Blanco	47.	J. Roth
6.	F. F. Blankenship	48.	A. D. Ryon
7.	G. E. Boyd	49.	W. F. Schaffer, Jr.
8.	R. B. Briggs	50.	Dunlap Scott
9.	R. E. Brooksbank	51.	J. H. Shaffer
10.	K. B. Brown	52.	M. J. Skinner
11.	W. L. Carter	53.	F. J. Smith
12.	H. D. Cochran, Jr.	54.	Martha Stewart
13.	F. L. Culler	55.	R. E. Thoma
14.	J. R. Distefano	56.	D. B. Trauger
15.	W. P. Eatherly	57.	Chia-Pao Tung
16.	D. E. Ferguson	58.	W. E. Unger
17.	L. M. Ferris	59.	C. D. Watson
18.	J. H. Frye	60.	J. S. Watson
19.	W. R. Grimes	61.	H. O. Weeren
20.	A. G. Grindell	62.	A. M. Weinberg
21.	P. A. Haas	63.	J. R. Weir
22.	B. A. Hannaford	64.	M. E. Whatley
23.	P. N. Haubenreich	65.	J. C. White
24.	J. R. Hightower, Jr.	66.	R. G. Wymer
25.	C. W. Kee	67.	E. L. Youngblood
26.	R. B. Lindauer	68-69.	Central Research Library
27.	J. C. Mailen	70-71.	Document Reference Section
28.	H. E. McCoy	72-74.	Laboratory Records
29-39.	L. E. McNeese	75.	Laboratory Records, RC
40.	D. M. Moulton	76.	Y-12 Document Reference Section
41.	J. P. Nichols	77.	ORNL Patent Office

EXTERNAL DISTRIBUTION

78. D. F. Cope, Atomic Energy Commission, RDT Site Office (ORNL)
79. A. R. DeGrazia, USAEC, DRDT, Washington, D.C. 20545
80. D. Elias, RDT, USAEC, Washington, D.C. 20545
81. Norton Haberman, RDT, USAEC, Washington, D.C. 20545
82. Kermit Laughon, Atomic Energy Commission, RDT Site Office (ORNL)
83-84. T. W. McIntosh, Atomic Energy Commission, Washington, D.C. 20545
85. M. Shaw, Atomic Energy Commission, Washington, D.C. 20545
86. Laboratory and University Division, ORO
87-88. Division of Technical Information Extension, ORO
89-90. E.G. Case,DRS, USAEC, Washington, D.C. 20545
91-93. P.A. Morris, DRL,USAEC, WASHINGTON, D.C. 20545